UNIVERSITÁ DEGLI STUDI DI TRIESTE
XXVII CICLO DEL DOTTORATO DI RICERCA IN
FISICA

TIME-RESOLVED AND IMAGING TECHNIQUES FOR PHOTOIONIZATION STUDIES OF ATOMS, MOLECULES AND CLUSTERS

Settore scientifico-disciplinare: FIS/03

Candidate:
Michele Di Fraia

Supervisor:
Dr. Marcello Coreno

co-Supervisor:
Prof. Fulvio Parmigiani

Coordinator:
Prof. Paolo Camerini

ANNO ACCADEMICO 2013/2014

Ringraziamenti

"...1500 anni fa tutti sapevano che la terra era il centro dell'universo,
500 anni fa tutti sapevano che la terra era piatta,
e 15 minuti fa tu sapevi che la gente era sola su questo pianeta;
immagina cosa saprai domani..."
(Agente K, M.I.B.)

Questo lavoro di tesi è stato realizzato presso il laboratorio di Luce di Sincrotrone Elettra a Trieste. È il frutto di un lavoro di gruppo, pertanto le persone che voglio ringraziare sono davvero molte e spero di non dimenticare qualcuno; dovesse succedere mi scuso in anticipo. Questa lunga lista comincia col ringraziare, Marcello Coreno, mio supervisore presso Elettra e responsabile della linea GasPhase, il quale è riuscito a coinvolgermi nel progetto di ricerca col solo trasmettermi parte della sua sconfinata passione per lo studio Sperimentale della fisica della materia (la "S" è volutamente maiuscola ma solo io e lui sappiamo perché ...). A lui devo le mie capacità professionali acquisite, le magiche notti di beamtime ed una piú profonda conoscenza della combinazione Malvasia&Tartine by Darko. Auguro a tutti i futuri dottorandi di poter trovare supervisori con le stesse capacità intellettuali ed umane che ho trovato io in Marcello.
Sono molto grato all'Università di Trieste ed al co-supervisore di tesi prof. Fulvio Parmigiani, per avermi accettato come dottorando.
Un ringraziamento speciale va a Carlo Callegari, responsabile della beamline LDM presso Fermi, per la sua infinita disponibilità e per non essersi mai risparmiato ad elargirmi preziosi consigli. Sì prima o poi io e te dovremmo tornare in Cina.
Un ringraziamento sincero va a tutto il gruppo della beamline GasPhase (senz'altro la più rumorosa beamline di tutta Elettra) per avermi accolto e per avermi messo a disposizione interi armadi pieni di flange e camere sperimentali con cui divertirmi. La caotica giostra delle camere sperimentali al cambio di ogni utente resterà impressa nella mia memoria come una elegante danza futuristica. Mi soffermo in particolare a ringraziare Robert Richter perchè, anche lui, non si è mai risparmiato a concedermi spiegazioni e dettagli tecnici sui vari spettrometri parcheggiati sulla beamline. Ringrazio Kevin C. Prince, responsabile del gruppo di ricerca GasPhase, per il paziente lavoro di rilettura e correzione ortografica delle tesi.

Monica de Simone per i consigli, le revisioni, la fornitura di libri, per gli innumerevoli pranzi e cene a casa sua a festeggiare sempre qualcosa.
Ringrazio il DJ (dottorando junior) Cesare Grazioli, sempre presente, sempre al mio fianco, dentro e fuori Elettra. Per me Cesare è stato la mano che ti viene in aiuto quando ti sei reso conto che hai accostato flangia e gasket ma hai dimenticato viti e bulloni; oppure che ti soccorre in mezzo di strada con i cavi della batteria. Lo ringrazio in particolar modo perchè nessuno come lui riesce a fare tali e grandiose figure di m.... (...gaffes... visto che gli piacciono i francesismi, si legga piú avanti) un maestro in questo. Allo stesso tempo, però, è capace di ostentare alta classe, ad esempio nel chiamare "vernissage" un aperitivo inaugurale al circolino arci.
Sempre per il team GaPh desidero ringraziare Antti Kivimäki e Michele Alagia.
Per tutto quello che so e che avrei sempre voluto sapere sul sistema VMI ringrazio Patrick O'Keeffe, il quale con molta pazienza è riuscito inoltre a farmi appassionare di processi quali ICD grazie alle sue pazienti spiegazioni. Con Matlab son più bravo io però, ammettilo.
Ringrazio Giuseppe Cautero per avermi ha accolto nei laboratori del gruppo detector di Elettra; Rudi Sergo per tutta la conoscenza appresa riguardo i detectors utilizzati in questo lavoro di tesi e per avermi messo a disposizione il mitico "Bunker"; Luigi (Harry) Stebel per averlo importunato più e più volte quando l'elettronica di lettura faceva i capricci. Capricci che immediatamente cessavano di esistere non appena l'aura magica di Harry si presentava nelle vicinanze della suddetta elettronica. Per i progressi fatti sul detector al diamante ringrazio Ralf H. Menk, Dario Giuressi e Matias Antonelli.
Sempre nell'ambito detector al diamante ringrazio il prof. Emanuele Pace ed Antonio De Sio del XUV_Lab dell'Università di Firenze, è voi in fondo che devo la mia presenza a Trieste, già dai tempi della tesi specialistica. Per voi resterò sempre qualcosa col suffisso in -ando (chissà magari post-dottorando).
Altra calorosa accoglienza mi è stata riservata dallo staff della beamline LDM di Fermi. In particolare ringrazio Paola Finetti per avermi aperto un mondo sulle diagnostiche, per le innumerevoli volte che abbiamo smontato il Beam Dump, per le discussioni sui risultati di cross-correlazione, ma soprattutto per avermi fatto scoprire un grande grandissimo amore chiamato Carbon Tape.
Ringrazio Oksana Plekan per l'aiuto nei tests del prototipo di manipolatore delle diagnostiche di LDM e per gli immancabili cioccolatini russi Romashki.
Nell'ambito del progetto della endstation di LDM un ringraziamento va a tutta la collaborazione, in particolare a: Frank Stienkemeier, Thomas Möller, Marcel Mudrich, Raphael Katzy, Aaron LaForge, Viktor Lyamayev, Yevheniy Ovcharenko, Nils B. Brauer, Marcel Drabbels, Tommaso Mazza, Michael Meyer, Paolo Piseri, Michele Devetta, Stefano Stranges.
Un ringraziamento particolare a Giovanni De Ninno per le nostre discussioni sulle misure di auto-correlazione.
Per il lavoro teorico svolto presso lo Jožef Stefan Institute di Ljubljana desidero esprimere un sincero ringraziamento a Matiaz Žitnik e Andrej Mihelič, a quest'ultimo in particolare va tutta la mia stima per la pazienza mostrata nei confronti di uno sperimentale come me.
Infine desidero ringraziare il personale delle sale controllo di Elettra, Fermi (poi unificate), per aver dato "Luce Utenti" e tutto il gruppo PADReS per aver fatto in modo che

la luce FEL entrasse nelle nostre camere (sperimentali) più (o meno) dritta possibile.
Per il lavoro di aggiornamento e fornitura dei disegni tecnici delle camere sperimentali ringrazio Luca Benedetti e Simone Gerusina. Per i lavori realizzati presso l'officina meccanica di Elettra con straordinaria maestria e pazienza ringrazio sentitamente Gianluca Bortoletto.
Inoltre, desidero ringraziare i miei genitori, il cui affetto e costante sostegno sono stati per me un prezioso motore per andare avanti e dare il 1000%. Sono convinto che ancora di preciso non abbiano ben compreso cosa ci faccia a Trieste fra laseroni e diamanti, tranquilli non siete i soli.
Ringrazio mio fratello (a.k.a. fardels), sapere che c'è sempre e mi attende impaziente è forse quanto di più rassicurante possa esistere per uno che ha qualche difficoltà a capire dove, spazialmente, si trovi la propria casa.
Ringrazio mio zio Giorgio il vero sostenitore finanziario di questo progetto di ricerca, grazie Zio ti ho rovinato.
Ringrazio la Sarina per avermi sempre accolto a braccia aperte al mio ritorno e la mitica Valeria per la fornitura costante di viveri realizzati con la sua infinita ars culinaria.
Ringrazio l'Ele per l'affetto che mi ha sempre manifestato e che ricambio incondizionatamente; Gianni e Sonia per la fiducia mostrata nell'avermi lasciato in custodia uno dei loro beni più preziosi. (Ammetto, ma non ditelo a lei, che in realtà è avvenuto l'esatto contrario, si sa ci vuole pazienza con i fisici).
Ringrazio tutto il gruppo di amici del Cortile, per tutto il buon tempo speso con la dovuta leggerezza al di fuori dell'ambiente scientifico.
Ringrazio il binario 2 della stazione di Firenze Rifredi fra saluti, partenze e ritorni (vorrei che Trenitalia ringraziasse me però).
Dimentico forse qualcuno? no mi sa di no ... chiudiamo qua. .... Beh sì ancora una persona manca all'appello. È con profonda gratitudine che ringrazio la mia piccola grande Vale, per tutto il sostegno morale e fisico, per i sacrifici condivisi e per i sogni di un futuro che attendo impaziente.

List of papers and personal contribution

The results presented in this Thesis are based on the following papers:

1. **Extreme ultraviolet ionization of pure He nanodroplets: Mass-correlated photoelectron imaging, Penning ionization, and electron energy-loss spectra**. D. Buchta, S. R. Krishnan, N. B. Brauer, M. Drabbels, P. O'Keeffe, M. Devetta, M. Di Fraia, C. Callegari, R. Richter, M. Coreno, K. C. Prince, F. Stienkemeier, J. Ullrich, R. Moshammer, M. Mudrich. *The Journal of Chemical Physics ,2013, 139, 084301.*

2. **Experimental investigation of the interatomic Coulombic decay in NeAr dimers**. P. O'Keeffe, A. Ciavardini, E. Ripani, P. Bolognesi, M. Coreno, L. Avaldi, M. Devetta, M. Di Fraia, C. Callegari, K. C. Prince, R. Richter. *Physical Review A,2014, 90, 4, 042508.*

3. **A modular end-station for atomic, molecular, and cluster science at the low density matter beamline of FERMI@Elettra**. V. Lyamayev,Y. Ovcharenko, R. Katzy, M. Devetta, L. Bruder,A. LaForge, M. Mudrich, U. Person, F. Stienkemeier, M. Krikunova,T. Möller,P. Piseri, L. Avaldi,M. Coreno, P. O'Keeffe, P. Bolognesi, M. Alagia, A. Kivimäki, M. Di Fraia, N.B. Brauer, M. Drabbels,T. Mazza, S. Stranges, P. Finetti, C. Grazioli, O. Plekan, R. Richter, K.C. Prince, C. Callegari. *Journal of Physics B: Atomic, Molecular and Optical Physics, 2013, 46, 16, 164007.*

4. **Novel Collective Autoionization Process Observed in Electron Spectra of He Clusters**. Y. Ovcharenko, V. Lyamayev, R. Katzy, M. Devetta, A. LaForge, P. O'Keeffe, O. Plekan, P. Finetti, M. Di Fraia, M. Mudrich, M. Krikunova, P. Piseri, M. Coreno, N.B. Brauer, T. Mazza, S. Stranges, C. Grazioli, R. Richter, K.C. Prince, M. Drabbels, C. Callegari, F. Stienkemeier, T. Möller. *Physical Review Letters, 2014, 112, 7, 073401.*

5. **Collective Autoionization in Multiply-Excited Systems: A novel ionization process observed in Helium Nanodroplets**. A. C. LaForge, M. Drabbels, N. B. Brauer, M. Coreno, M. Devetta, M. Di Fraia, P. Finetti, C. Grazioli, R. Katzy,V.

Lyamayev, T. Mazza, M. Mudrich, P. O'Keeffe, Y. Ovcharenko, P. Piseri, O. Plekan, K. C. Prince, R. Richter, S. Stranges, C. Callegari, T. Möller, F. Stienkemeier. *Scientific Reports, 2014, 4, 3621.*

The results diplayed in this Thesis about characterization of the endstation and/or detection system has been obtained in preparation of the successful beamtimes that have concluded with the following list of papers:

6. **Determining the polarization state of an extreme ultraviolet free-electron laser beam using atomic circular dichroism**. T. Mazza, M. Ilchen, A. J. Rafipoor, C. Callegari, P. Finetti, O. Plekan, K. C. Prince, R. Richter, M. B. Danailov, A. Demidovich, G. De Ninno, C. Grazioli, R. Ivanov, N. Mahne, L. Raimondi, C. Svetina, L. Avaldi, P. Bolognesi, M. Coreno, P. O'Keeffe, M. Di Fraia, M. Devetta, Y. Ovcharenko, T. Möller, V. Lyamayev, F. Stienkemeier, S. Düsterer, K. Ueda, J. T. Costello, A. K. Kazansky, N. M. Kabachnik, M. Meyer. *Nature Communications, 2013, 5, 3648.*

The following papers have been submitted or still in writing phase:

7. **The Low Density Matter (LDM) beamline of FERMI**. C. Svetina, C. Grazioli, M. Alagia, L. Avaldi, G. Cautero, M. de Simone, M. Devetta, M. Di Fraia, M. Drabbels, C. Fava, V. Feyer, P. Finetti, S. Gerusina, R. Katzy, A. Kivimaki, V. Lyamayev, N. Mahne, T. Mazza, A. Moises, T. Möller, P. O'Keeffe, Y. Ovcharenko, P. Piseri, O. Plekan, K.C. Prince, L. Raimondi, R. Sergo, F. Stienkemeier, S. Stranges, M. Zangrando, M. Coreno and C. Callegari. *Submitted to Journal of Synchrotron Radiation.*

8. **PhotoIonization and Velocity Map Imaging spectroscopy of Atoms, Molecules and Clusters with Synchrotron and Free Electron Laser Radiation at Elettra**. M. Di Fraia, R. Sergo, L. Stebel, D. Giuressi, G. Cautero, M. Tudor, C. Callegari, P. O'Keeffe, Y. Ovcharenko, V. Lyamayev, V. Feyer, A. Moise, M. Devetta, P. Piseri, C. Grazioli, M. Coreno.*Submitted for a Special Issue of Nuclear Instruments and Methods in Physics Research Section B: Proceedings.*

9. **Fast Beam Monitor Diamond Based Devices For VUV And X Synchrotron Radiation Facilities**. A. De Sio, M. Di Fraia, M. Antonelli, R. Nesti, D. Panella, R.H. Menk, G. Cautero, M. Coreno, C. Callegari, E. Pace. *In writing phase.*

The following is a list of papers to which I have contributed but that are not included in this Thesis.

10. **The Role of the Partner Atom and Resonant Excitation Energy in Interatomic Coulombic Decay in Rare Gas Dimers**. P. O'Keeffe, E. Ripani, P. Bolognesi, M. Coreno, M. Devetta, C. Callegari, M. Di Fraia, K.C. Prince, R. Richter, M. Alagia, A. Kivimäki, L. Avaldi. *The Journal of Physical Chemistry Letters, 2013, 4, 11, 1797-1801.*

11. **Charge Transfer and Penning Ionization of Dopants in or on Helium Nanodroplets Exposed to EUV Radiation**. D. Buchta, S. R. Krishnan, N. B. Brauer,

M. Drabbels, P. O'Keeffe, M. Devetta, M. Di Fraia, C. Callegari, R. Richter, M. Coreno, K. C. Prince, F. Stienkemeier, R. Moshammer, M. Mudrich. *The Journal of Physical Chemistry A, 2013, 117, 21, 4394-4403.*

12. **X-ray micro beam analysis of the photoresponse of an enlarged CVD diamond single crystal**. A. De Sio, M. Di Fraia, M. Antonelli, R.H. Menk, G. Cautero, S. Carrato, L. Tozzetti, J. Achard, A. Tallaire, R.S. Sussmann, E. Pace. *Diamond and Related Materials, 2013, 34, 36-40.*

13. **Fast synchrotron and FEL beam monitors based on single-crystal diamond detectors and InGaAs/InAlAs quantum well devices**. M. Antonelli, M. Di Fraia, S. Carrato, G. Cautero, R.H. Menk, W.H. Jark, T. Ganbold, G. Biasiol, C. Callegari, M. Coreno, A. De Sio, E. Pace. *Nuclear Instruments and Methods in Physics Research A, 2013, 26 164-167.*

14. **X-Ray Beam Position Monitor Based on a Single Crystal Diamond Performing Bunch by Bunch Detection**. M. Di Fraia, M. Antonelli, A. Tallaire, J. Achard, S. Carrato, R.H. Menk, G. Cautero, D. Giuressi, W.H. Jark, F. D'Acapito, A. De Sio, E. Pace. *Journal of Physics: Conference Series, 2013, 425, 212001.*

15. **High Resolution Multiphoton Spectroscopy by a Tunable Free-Electron-Laser Light**. M. Žitnik, A. Mihelič, K. Bučar, M. Kavčič, J.-E. Rubensson, M. Svanquist, J. Söderström, R. Feifel, C. Såthe, Y. Ovcharenko, V. Lyamayev, T. Mazza, M. Meyer, M. Simon, L. Journel, J. Lüning, O. Plekan, M. Coreno, M. Devetta, M. Di Fraia, P. Finetti, R. Richter, C. Grazioli, K. C. Prince, and C. Callegari. *Physical Review Letters, 2014, 113, 19, 193201.*

16. **Tunability experiments at the FERMI free-electron laser**. Allaria E., Battistoni A., Bencivenga F., Borghes R., Callegari C., Capotondi F., Castronovo D., Cinquegrana P., Cocco D., Coreno M., Craievich P., Cucini R., D'Amico F., Danailov M.B., Demidovich A., De Ninno G., Di Cicco A., Di Fonzo S., Di Fraia M.,Di Mitri S., Diviacco B., Fawley W. M., Ferrari E., Filipponi A.,Froehlich L., Gessini A., Giangrisostomi E., Giannessi L., Giuressi D., Grazioli C.,Gunnella R.,Ivanov R.,Mahieu B.,Mahne N., Masciovecchio C., Nikolov I.P., Passos G.,Pedersoli E., Penco G.,Principi E., Raimondi L., Sergo R., Sigalotti P., Spezzani C., Svetina C., Trovó M., Zangrando M. *New Journal of Physics, 2012, 14, 113009.*

Comments on my own participation

This Thesis is the result of a teamwork involving a huge number of people, which is common when dealing with large scale light source facilities as Elettra. My personal contribution to the papers varied, as reported in greater detail below, focused for the most on the instrumentations used.

For papers 1, 10 and 11 I was responsible for the detectors. In particular I was in charge of performing a test run of the position sensitive detector in offline pre-beamtime tests; mounting of the experimental chamber and alignment in the final beamline location; vacuum leak testing; mounting of the floating voltage supply chain; helping in setting up the readout electronic system. During the experimental runs I was in charge of running the detectors, data acquisition, offline data analysis and providing Matlab scripts. After the beamtimes, pre-processing of data in PEPICO and PEPIPICO configuration. Disassembly of the setup and storage in a vacuum enviroment of the detectors.

For papers 2 and 8 I did SIMION simulations for both the Velocity Map Imaging position sensitive detector and Time-Of-Flight spectrometer according to the experimental scientific specifications. Then I mounted a new position sensitive detector for the VMI system and a shorter dirft tube for the TOF spectrometer. Again an offline pre-beamtime test run of the position sensitive detector has been performed. Then mounting of the whole experimental chamber and alignment in the final beamline location. Vacuum leak testing, mounting of a floating voltage supply chain, helping in setting up the readout electronic system. During the experimental run I was in charge of running the detectors, data acquisition, offline data analysis by using Matlab scripts. After the beamtime, pre-processing of data in PEPICO and PEPIPICO configuration. Disassembly of the setup and storage in a vacuum enviroment of the detectors.

For paper 6 before the beamtime I took active part in the mounting of the newly built recombination mirror chamber for pump and probe experiments. Then I prepared the endstation for the experimental run with vacuum leak tests and bakeout of the beam dump and recombination mirror section. During the time assigned for the beamtime I was in charge of data acquisition, online data analysis and preliminary offline data analysis. The cross-correlation measurement on helium targets for the estimation of the FERMI pulse duration (reported in the chapter 5), is relative to the endstation characterization performed in preparation of the measurements subject of this paper.

For papers 9, 12, 13 and 14 I designed the support frame for the detector chamber, as well as an additional diagnostic stage (photodiode and pinhole on UHV manipulator). Then I assembled the whole experimental setup, readout electronic and voltage supply; performed vacuum test and alignment of the experimental chamber. In addition I took an active part in the following beamtime activities: data acquisition, detector startup, data analysis and discussion.

For papers 3, 4, 5, 7, 15 and 16, before the experimental runs I took active part in the design and assembly of the UHV beam diagnostics installed for alignment and refocussing of the FEL beam in the LDM end station, as well as for spatial superposition

of the optical beam for pump probe experiments. Then I prepared the endstation for the beamtimes with vacuum leak tests and bakeout of the beam dump section. During the shift assigned for the beamtimes I was in charge of data analysis acquisition, logbook, online data analysis and preliminary offline data analysis.

However these publications reflect about only the 40% of the work done during the doctoral project. This work also includes several unsuccessful beamtimes, offline work for detector problem solving and a huge quantity of SIMION simulations. In addition the theoretical investigation related to the autocorrelation measurements on helium targets for the FERMI pulse duration (see appendix D) has been object of my period spent abroad, at the Josez Stephan Institue in Ljubljana, in the group lead by Dr. Matiaz Žitnik.

Contents

Ringraziamenti **I**

List of papers and personal contribution **V**

Introduction **1**

1 Basics of photoelectron spectroscopy **5**
1.1 The electronic structure of atoms and rare gas clusters 5
1.1.1 Many electron atoms 6
1.1.2 Rare Gas Clusters 7
1.2 The Atom-Photon Interaction: the dipole approximation 9
1.2.1 Electronic transitions 10
1.3 Electron spectrometers 12
1.3.1 Hemispherical Analyzer 13
1.3.2 Time-of-flight spectrometers and magnetic bottle spectrometers . 14
1.3.3 Velocity map imaging spectrometers 15

2 Modern light sources **17**
2.1 Synchrotron Radiation 17
2.1.1 Elettra 20
2.2 Free Electron Lasers 20
2.2.1 FERMI 23

3 Experimental methods **25**
3.1 The Velocity Map Imaging technique 25
3.2 The Time-Of-Flight mass spectrometer 27
3.3 Diamond-based photon beam monitors 30

4 Experimental setup **33**
4.1 The VMI experimental chamber at the GasPhase beamline 34
4.1.1 The Source Chamber 36
4.1.2 The Interaction Chamber 37

4.1.3 Power Supply, Readout Electronics and Data Acquisition 41
4.2 The Low Density Matter endstation at FERMI 43
4.2.1 The Interaction Chamber 46
4.3 Diamond detectors for beam diagnostics 47

5 Results **51**
5.1 Experiments at Elettra 51
5.1.1 Atomic spectra (Ne, Xe) 51
5.1.2 Rare gas clusters: XUV ionization of He nanodroplets 55
5.1.3 Rare gas clusters: Interatomic Coulombic Decay in NeAr Dimers 57
5.2 Experiments at FERMI 60
5.2.1 Atomic spectra (Ne,Xe) 60
5.2.2 Novel collective autoionization process in He clusters 62
5.2.3 Temporal overlap in two colours pump and probe experiments . . 65
5.2.4 Cross-correlation method for the FERMI pulse duration 66
5.2.5 Auto-correlation method for the FERMI pulse duration 69
5.3 Fast beam monitors based on diamond detectors 73

Conclusions **77**

A Image inversion **I**
A.1 The Method II

B SIMION® simulation software **V**
B.1 Potential optimization example V
B.2 Energy calibration simulation VII

C Helium multiphoton double ionization **XI**
C.1 Theoretical Background XI
C.1.1 Process 1: Direct Two Photon process (D2P) XIII
C.1.2 Process 2: Sequential Three Photon process (S3P) XIII
C.1.3 Photon flux XV
C.2 Simulation Results and Discussion XVII

List of Symbols and Acronyms **XXI**

Bibliography **XXV**

Introduction

X-RAY and Ultraviolet photoelectron spectroscopy has nowdays become the most used technique for studying the electronic properties of atoms, molecules, solids and surfaces. In recent years, research devoted to the study of the electronic structure of atoms, molecules and clusters by means of VUV and soft X-ray radiation, has greatly benefited from the advance in new experimental methods. In particular new generation high-brightness light sources such as Synchrotrons and Free Electron Lasers have greatly increased the number of experiments and also the range of accessible phenomena.

This doctoral project has been carried out at Elettra, Trieste, the Italian national synchrotron radiation (SR) laboratory. It has been integrated into the activities of the local Atomic and Molecular Physics group, which aims at studying the electronic structure of isolated systems of increasing complexity such as atoms, molecules and clusters in the gas phase.

Clusters are aggregates of atoms containing from few to a few thousand atoms. By studying the properties of clusters, one obtains information on the early stage of the growth of matter, and on the evolution of the properties towards the bulk.

At Elettra, the opportunity of combined access to the GasPhase beamline of the storage ring and to the Low Density Matter beamline of the FERMI Free Electron Laser (FEL) allows covering a wide spectrum of single and multiphoton processes by means of advanced experimental techniques, for a thorough description of both energetics and dynamics of isolated systems.

The collaboration between the Atomic and Molecular Physics group, and the Elettra Instrumentation and Detector Laboratory, has resulted in a prototype set-up, built around a Velocity Map Imaging (VMI) spectrometer, with the flexibility to perform SR as well as FEL experiments, just by changing the last stage of detection:

SR setup

In SR experiments, at the GasPhase synchrotron beamline, a crossed-delay-line detector is used, coupled to a 4-channel time-to-digital converter that reconstructs the position of the electrons. It operates in tandem with a Time-of-Flight (TOF) mass spectrometer, used to acquire photoion spectra.

Such a system allows PhotoElectron-PhotoIon-Coincidence (PEPICO) spectroscopy of atoms, molecules and clusters, by correlating the kinetic energy and emission angle of photoelectrons with ions of a specific mass;

FEL setup

FEL experiments notably differ from SR experiments in the much higher rate of events produced and detected (per photon pulse), which usually forces one to forfeit coincidence detection. At the Low Density Matter (LDM) beamline of the FEL FERMI, an imaging plate consisting of a Micro Channel Plate (MCP) a phosphor screen and a CCD camera is used. The system is capable of shot-by-shot collection of practically all events, albeit without time resolution. Additionally femtosecond pump-and-probe experiments can be performed to access the electron dynamics.

Within this framework, the core of my experimental thesis is based on imaging and electron-ion coincidence techniques to investigate the energetics, the angular distribution and also dynamics of electrons and ions emitted upon VUV irradiation of atomic, molecular, and cluster targets, in parallel to a characterization of the light source used. The basic components for performing an X-ray or UV photoemission experiment are: a specimen to be studied, a radiation source, an electron spectrometer and detection system. The development done in new radiation source requires a parallel development in experimental methods, detection techniques, readout system and beam diagnostic system. A general overview of these components is given in the first chapters of this thesis work.
In particular the first chapter of this thesis is dedicated to a brief theoretical introduction on the electronic structure of atoms and rare gas clusters and also to photon-matter interaction, focusing in particular on the photoionization process. In the last section of this chapter a brief overview of the most used electron spectrometers is given.
In chapter 2 a brief description of SR and FEL radiation has been reported together with the main characteristics of the two light sources.
Chapter 3 has been devoted to the description of principles of the VMI spectrometers and TOF technique. Since this is an experimental thesis, chapters 4 and 5 represent the core of this work. In chapter 4 a full description of the experimental setup has been reported, where the SR setup has been also used for a preliminary test for the FEL setup only by changing the last stage of the detection system. Then a description of the final FEL setup is reported as well.
In chapter 5, a thorough characterization of both experimental setups has been performed and presented, along with some recent results obtained with the purpose of exploiting the capabilities of the detection systems. In particular, a section of this chapter is dedicated to helium clusters mass-correlated photoelectron images obtained with the SR, by means of PEPICO spectroscopy. In this work detailed insight into the dynamics of photoexcitation and ionization of pure He clusters has been gained; in particular we have observed inelastic collisions of the outgoing photoelectrons with the surrounding He atoms in the clusters.
With the same SR setup, but by means of the triple coincidence PhotoElectron-PhotoIon-PhotoIon technique (PEPIPICO), the Interatomic Coulombic Decay (ICD) in rare gas clusters has been studied and reported in a section of chapter 5. ICD is a decay channel occurring in weakly bound systems, where electronic energy is transferred (via virtual

photon exchange) from an inner valence excited atom to a neighboring atom, which releases it by emitting a low energy electron. Predicted theoretically at the end of the last century by Cederbaum, ICD has been more recently confirmed experimentally and, since then, it has become the subject of numerous studies. ICD in fact appears to play a major role in a large numbers of systems; e.g. genetic radiation damage can stem from ICD electrons produced in the aqueous environment of biological tissue, in fact low energetic ICD electrons produced in an aqueous environment have been demonstrated to be responsible for much of biological radiation damage. Experimental results on the energy distribution of the electrons emitted in the ICD process in rare gas dimers are reported.
In addition, chapter 5 includes also pump-and-probe experiments carried out with the FEL setup on helium atomic targets. Here the setup has been exploited for the temporal characterization of the FEL light of FERMI. In fact, photoionization of simple atomic targets is usually one of the most used tools to characterize not only the detector response, but also the properties of the incident light.
In modern light sources, the high brightness beamlines using undulator radiation are the most sensitive to electron beam oscillations. The insertion of photon Beam Position Monitors (pBPM) is useful in order to provide those systems with important information, such as photon beam position, absolute intensity and temporal structure; furthermore, several beamline experiments require these data to be known in order to give quantitative results.
Electron beam position stability has been intensively addressed in recent years by the use of Fast Orbit Feedback (FOFB) based on electron Beam Position Monitors (eBPM); conversely, beamlines have not been provided so far with a fast local control system based on the information collected by the pBPMs. Those measurements are rarely used to compensate for long term thermal drifts (of the order of minutes) or to adjust experimental data; recently, integration of pBPM information into the FOFB has been proposed. Hence, for both diagnostics and calibration issues, several SR applications require an in situ detector exhibiting high radiation hardness, fast response, homogeneity and possibily high transparency for X-ray absorption experiments.
Thanks to its unique physical and electronic properties diamond (see chapter 3) is the most promising material for the production of semitransparent in-situ photon Beam Monitors (pBM). A small section at the end of chapter 5 has been dedicated to illustrate preliminary results on Diamond Photon Beam Monitors.

CHAPTER 1

Basics of photoelectron spectroscopy

Atoms and molecules are the fundamental building blocks of matter. They are the smallest units responsible for the characteristic properties of gases, liquids and solids. For this reason a deeper understanding of the atomic electronic structure and dynamics is of extreme importance for the comprehension of the properties of matter. Even if the author's work is primarily experimental a brief theorethical introduction is needed for the sake of completeness. In the first section of this chapter a quick overview on the electronic structure of the targets under study will be given; the second section is dedicated to the interaction of atoms with radiation, focusing on the photoionization process. The last section is a brief overview of the most common electron spectrometers, with a motivation for the technique chosen in this thesis work.

1.1 The electronic structure of atoms and rare gas clusters

In a typical photoelectron emission experiment, the basic excitation process involves the absorption of a photon with energy $h\nu$ according to the following representation:

$$\Psi^i_{tot}(N), E^i_{tot}(N) \xrightarrow{h\nu} \Psi^f_{tot}(N,K), E^f_{tot}(N,K) \tag{1.1}$$

where $\Psi^i_{tot}(N)$ is the initial-state N-electron wave function corresponding to a total energy $E^i_{tot}(N)$, and where $\Psi^f_{tot}(N,K)$ is the K-th final-state N-electron wave function (including the photoelectron) corresponding to a total energy $E^f_{tot}(N,K)$. In this context the determination of accurate N-electron wave functions is a key problem [1]. I will limit the discussion describing the simplest method: the non relativistic *Hartree-Fock* or *self-consistent field* method. This model is also valid for others systems such as electrons in a molecule or a solid [2].

1.1.1 Many electron atoms

Limiting this section to the discussion of the *ground state* of an atom, neglecting spin-orbit interaction and considering only the Coulomb attraction between the nucleus and the electrons and the Coulombic repulsion between electrons, the non-relativistic Hamiltonian for a many electron atom is:

$$\mathcal{H} = \sum_{i=1}^{N} \Big(-\frac{\hbar^2}{2m}\nabla_{r_i}^2 - \frac{Ze^2}{4\pi\epsilon r_i}\Big) + \sum_{i<j=1}^{N} \frac{e^2}{4\pi\epsilon r_{ij}} \tag{1.2}$$

where m is the electron mass, Z the atomic number, r_i is the position of the i^{th} electron, ϵ the electric constant and e the electron charge. The first two terms of the equation are the kinetic energy and the potential energy for each electron in the Coulomb field of a nucleus of charge Z. The term with r_{ij}=|$\mathbf{r}_i$-$\mathbf{r}_j$| is the electrostatic repulsion between the electrons $\mathbf{r}_i$ and $\mathbf{r}_j$ [3]. This electrostatic term is too large to be treated as a perturbation, to go further a physical assumption is required: a large part of the repulsion between electrons can be treated as a central potential $S(r)$. This *central-field approximation* (CF) for the total potential energy depends only on the radial coordinate:

$$V_{CF}(r) = \frac{Ze^2/4\pi\epsilon}{r} + S(r) \tag{1.3}$$

and with such an approximation the Hamiltonian becomes:

$$\mathcal{H}_{CF} = \sum_{i=1}^{N} \Big\{ -\frac{\hbar^2}{2m}\nabla_i^2 + V_{CF}(r_i) \Big\} \tag{1.4}$$

and then the Schrödinger equation $\mathcal{H}\psi = E_{atom}\psi$ can be separated in N one-electron equations of the form:

$$\Big\{ -\frac{\hbar^2}{2m}\nabla_i^2 + V_{CF}(r_i) \Big\}\psi_i = E_i\psi_i \tag{1.5}$$

the total wavefunction is $\psi = \psi_1\psi_2\psi_3\cdots\psi_N$ and the total energy $E_{atom} = E_1 + E_2 + E_3 ... + E_N$. Note that this wavefunction is symmetric, however we know that the overall wavefunction has to be antisymmetric with respect to the interchange of electrons, since they are spin 1/2 particles. So the proper antisymmetric wavefunction is achieved in the Hartree-Fock method with the use of the *Slater Determinant* considering also the electron spin σ_i:

$$\psi = \frac{1}{\sqrt{N!}} \begin{vmatrix} \psi_1(r_1,\sigma_1) & \psi_1(r_2,\sigma_2) & ... & \psi_1(r_{N-1},\sigma_{N-1}) & \psi_1(r_N,\sigma_N) \\ \psi_2(r_1,\sigma_2) & \psi_2(r_2,\sigma_2) & ... & \psi_2(r_{N-1},\sigma_{N-1}) & \psi_2(r_N,\sigma_N) \\ . & . & . & . & . \\ . & . & . & . & . \\ \psi_N(r_1,\sigma_1) & \psi_N(r_2,\sigma_2) & ... & \psi_N(r_{N-1},\sigma_{N-1}) & \psi_N(r_N,\sigma_N) \end{vmatrix}.$$

To solve equation 1.5 we can adopt a separation into an angular part and a radial part. But for the radial part we need to know the exact form of V_{CF} in order to compute the wavefunctions numerically [3]. The Hartree-Fock self-consistent method is an iterative

method starting from an initial trial potential for calculating the wavefunctions. These wavefunctions are then used to calculate a new average potential, and so on until the changes in the potential and wavefunction converge to a *self-consistent solution.* The solutions identifying a state of a bound electron in the atom can be fully described using four quantum numbers: the principal quantum number n, the angular momentum quantum number l, the magnetic quantum number m_l and the spin quantum number s. The possible values of the quantum numbers and their spectroscopical notation are summarized in the table 1.1.

Table 1.1: *Atomic Quantum Numbers*

Quantum Number	Symbol	Values	Notation
Principal	n	1,2,3,...	K,L,M,...
Angular momentum	l	0,1,...,n-1	s,p,d,...
Magnetic	m_l	-l,-l+1,...,l-1,+l	-
Spin	s	$\pm$ 1/2	-

The electron configuration of an atom provides the set of occupied orbitals and the number of electrons in each orbital. Following the Pauli exclusion principle, which states that it is not possible to have two electrons with the same quantum state (i.e. the same set of quantum numbers), it can be shown that for an electronic shell, corresponding to a principal quantum number n, we can have a maximum of $2n^2$ electrons. Analogously, for a given subshell described by l we can have a maximum of $2(2l+1)$ electrons. The general notation for the electron configuration of a N-electron atom is $(n_1 l_1)^{k_1}(n_2 l_2)^{k_2}...(n_N l_N)^{k_N}$ where n and l identify the occupied orbitals (named using the symbols indicated in table above) and where k_i indicates the number of electrons in the orbitals. Orbitals are filled in order of increasing $n+l$ and for a given value of $n+l$ in order of increasing n. In order to completely describe the quantum state of the atoms, the angular and spin momenta (described by l and s) are coupled to give the total angular momentum of the atom.

1.1.2 Rare Gas Clusters

Clusters are aggregates of atoms consisting of few to a few thousand atoms. Due to their small size, their properties are in general different from those of the corresponding material in the bulk phase [4]. By studying the properties of clusters, one expects to obtain information on the early stage of the growth of condensed matter, and on the evolution of the properties towards the bulk [4]. One of the main questions is: how many atoms are required for a cluster to show the properties of the bulk material? Such questions have motivated the development of the experimental techniques for producing small clusters, as well as a series of experimental and theoretical studies of their structure and properties [4].
Several types of clusters have been classified according to the different type of forces that bind atoms in the aggregate. In table 1.2 a list of the binding forces for different types of clusters is given [5]. Metallic and covalent clusters are included as well. Since it is not the purpose of this thesis to describe the physics of clusters, only a brief overview of van der Waals clusters will be given. Van der Waals interactions describe the interaction between rare gas elements. The rare gas atoms or inert gas atoms, lie

Table 1.2: *Classification of clusters by the binding forces forming the aggregate.*

Cluster type	Binding Energy	Examples
Van der Waals clusters	0.01 - 0.05 eV	$(\text{rare gas})_n$, $(N_2)_n$, ...
H-bonded clusters (dipole-dipole interaction)	0.1-0.3 eV	$(H_2O)_n$, $(NH_3)_n$, ...
Ionic clusters (Coulomb force)	0.5-1.0 eV	$(NaCl)_n$, $(H_2O)_nNa^+$, ...
Metallic and Valence clusters (covalent bond)	1.0-4.0 eV	$(\text{alkali metal})_n$, Si_n, C_n, ...

on the extreme right-hand side of the periodic table of elements and they are characterized by closed-shell electronic configurations. Helium has the electronic configuration $1s^2$ while the heavier elements have the outer (valence) shell configuration $(ns)^2(np)^6$, where for neon $n = 2$, argon $n = 3$, krypton $n = 4$, xenon $n = 5$ and radon $n = 6$ [6]. It is this closed shell nature, and thus a high atomic ionization energy, which renders those elements so chemically inert (or noble) thus resulting in a weak interatomic interactions between rare gas atoms, as one can see in table 1.2. Rare gas dimers exhibit no net covalent bonding, but a weak interaction dominated by London-Drude dispersion forces: these long range attractive forces called van der Waals forces are of the form [7]:

$$V_{disp} = -\frac{C_6}{r^6} \;;\; C_6 = \frac{3\alpha^2 I}{4(4\pi\epsilon_0)^2} \tag{1.6}$$

where α and I are the atomic polarizability and ionization energy, respectively [7]. There is a limit to the compressibility of matter because, at short internuclear separations, repulsion forces are present between the atomic nuclei, as well as between electrons (both core and valence) on neighbouring atoms. The total short range repulsive interaction is generally modelled by an exponential term (e^{-Ar}) dependence on the interatomic distance. But usually this term is substituted with a $1/r^{12}$ term which is faster to compute than an exponential. The combination of the attractive term with the repulsive one leads to the famous Lennard-Jones (LJ) model pair potential energy function:

$$V^{LJ}(r) = \epsilon\left\{\left(\frac{r_0}{r}\right)^{12} - 2\left(\frac{r_0}{r}\right)^{6}\right\} \tag{1.7}$$

where ϵ is the well depth (the binding energy of the dimer) and r_0 is the equilibrium internuclear separation. Values of the LJ well depth ϵ and internuclear separations r_0 are given in table 1.3 [8]:

Table 1.3: *Lennard-Jones parameters for Rare Gas Dimers*

Element	ϵ(meV)	r_0(Å)	References
He	0.93	2.9673	Aziz et al. [9]
Ne	3.6	3.087	Aziz et al. [10]
Ar	12.34	3.759	Aziz and Chen [11]
Kr	17.22	4.012	Aziz [12]
Xe	24.33	4.3634	Barker et al. [13]

Neutral rare gas clusters can be produced by expanding a gas from a high pressure volume through a nozzle into vacuum. This method has been used in this thesis work.

The temperature of the gas is critical for the cluster formation process. The expansion of gases in the cluster source is adiabatic, which implies that there is no heat transfer Q into or out of the system [14].
This is of course an idealization, applicabile if the process takes place so rapidly that there is no time for significant heat transfer. Such expansions may change the temperature T of the gas as can be shown considering the generalized law of thermodynamics:

$$dU = TdS - pdV + \sum_i \mu_i dN_i \tag{1.8}$$

Here the sum is over all N_i particles and μ_i denotes the chemical potential per particle, U the internal energy, S the entropy, V the volume. In the present case the number of particles N in the process is constant. Then the central law of thermodynamics reads as:

$$dU = TdS - pdV \tag{1.9}$$

After some manipulation [14], it can be shown that the temperature change associated with adiabatic expansion into vacuum where dU = 0 may now be written as:

$$(dT)_U = \frac{1}{C_V}\Big[p - T\Big(\frac{\partial p}{\partial T}\Big)_{V,N_i}\Big]dV_U \tag{1.10}$$

Where $C_V = (\frac{\partial U}{\partial T})_V$ is the heat capacity for a gas at constant volume; $p = -(\frac{\partial U}{\partial V})_{S,N_i}$. For an ideal gas it is easy to verify that eq. 1.10 yields dT=0, hence, there will be no temperature change in an ideal gas expanding adiabatically into vacuum [14]. If we consider a real gas, the van der Waals law for non-ideal gases may be used instead of the ideal gas one:

$$\Big(p + \frac{a}{V_m^2}\Big)(V_m - b) = RT \tag{1.11}$$

Here a and b are constants and depend on the type of gas. a describes the intermolecular/interatomic attraction and b compensates for the size of the molecule/atom. V_m is the molar volume. After some manipulation, for a finite size change we get [14]:

$$T_2 - T_1 = \frac{a}{C_V}\Big(\frac{1}{V_{m,2}} - \frac{1}{V_{m,1}}\Big) \tag{1.12}$$

When expanding the gas into vacuum, $V_{m,2}$ will approach infinity. Therefore we find:

$$T_2 = T_1 - \frac{a}{C_V V_{m,1}} \tag{1.13}$$

thus the temperature change in an adiabatic expansion which is dependent on a,C_V, and $V_{m,1}$ of the expanding gas [14]. Since all these properties are positive in the normal case, the gas will be cooled in the adiabatic expansion. The cooling associated with the gas expansion is the key point in the cluster source used in experiments since it can induce cluster formation.

1.2 The Atom-Photon Interaction: the dipole approximation

The interaction of an atom with a classical monochromatic electromagnetic field can be described by the following Hamiltonian operator [15]:

$$\mathcal{H}(\mathbf{r},t) = \frac{1}{2m}[\mathbf{P} + e\mathbf{A}(\mathbf{r},t)]^2 - e\Phi(\mathbf{r},t) + V(|\mathbf{r}|), \tag{1.14}$$

where $\mathbf{A}(\mathbf{r},t)$ and $\Phi(\mathbf{r},t)$ are the spatial and time-dependent, vector and scalar potential of the external field, $-e$ is the electron charge (e taken to be positive), $V(|\mathbf{r}|)$ is the usual Coulomb interaction binding the electron to the nucleus. $\mathbf{A}(\mathbf{r},t)$ and $\Phi(\mathbf{r},t)$ are gauge invariant. With the choice of a particular gauge, namely the Coulomb gauge [15], the radiation field is completely described by the vector potential, having the form $\mathbf{A}=\mathbf{A}_0 e^{(\mathbf{kr}-\omega t)}$ + complex conjugate, with wave vector $|\mathbf{k}| = 2\pi/\lambda$. So the Hamiltonian reads as:

$$\mathcal{H}(\mathbf{r},t) = [\frac{\mathbf{P}}{2m} + e\mathbf{A}(\mathbf{r},t)]^2 + V(|\mathbf{r}|), \tag{1.15}$$

For $|\mathbf{r}|$ values of typical atomic dimensions and for the typical wavelength λ used in the following experiments (tens of nanometers), $\mathbf{k}\cdot\mathbf{r} << 1$, so that over the extent of an atom, the vector potential is spatially nearly constant $\mathbf{A}(\mathbf{r},t) \simeq \mathbf{A}(t)$. This is the so-called *dipole approximation*. With an appropriate choice of the gauge functions, the Hamiltonian of the atom-radiation system is described by the following equation:

$$\mathcal{H}(\mathbf{r},t) = \frac{1}{2m}[\mathbf{P} + V(|\mathbf{r}|)] + e\mathbf{r}\cdot\mathbf{E}(t), \tag{1.16}$$

where $\mathbf{E}(t)$ is the electric field. The Hamiltonian can be thus separated into two contributions [16]:

$$\mathcal{H} = \mathcal{H}^A + \mathcal{V}^{AF}(t), \tag{1.17}$$

$\mathcal{H}^A$ is the atomic term and $\mathcal{V}^{AF}(t)$ is the interaction term given by:

$$\mathcal{V}^{AF} = -\mathbf{d}\cdot\mathbf{E}(t) \tag{1.18}$$

where $\mathbf{d} = -e\mathbf{r}$ is the dipole moment.

1.2.1 Electronic transitions

During an absorption process, a photon disappears and its energy is transferred to the particle. A certain minimum value of the photon energy, known as ionization threshold, is required to remove an electron from an atom or a molecule. When photons with energy below the ionization threshold are absorbed a bound electron is moved to an empty orbital and the atom or molecule is left in a neutral excited state, see fig. 1.1 a):

$$h\nu + A \rightarrow A^\star \tag{1.19}$$

This process is called *resonant photoexcitation*. If the photon is more energetic, above the ionization threshold, the absorption between a discrete state and a continuum state is called *photoionization*. Photoionization involves the ejection of electrons from atoms or molecules caused by their interaction with monochromatic photons.

$$h\nu + A \rightarrow A^+ + e^- \tag{1.20}$$

The ejected electrons e^- are called *photoelectrons*, see fig. 1.1 b). The photon radiation does not produce any photoelectrons until the ionization threshold (E_i) is reached. (see figure 1.1) [17].

In this process an atom, initially in a discrete internal state *A*, for example the ground state, absorbs a photon. This disappearance of a photon, accompanied by the appearance of a photoelectron, is simply the well-known photoelectric effect.

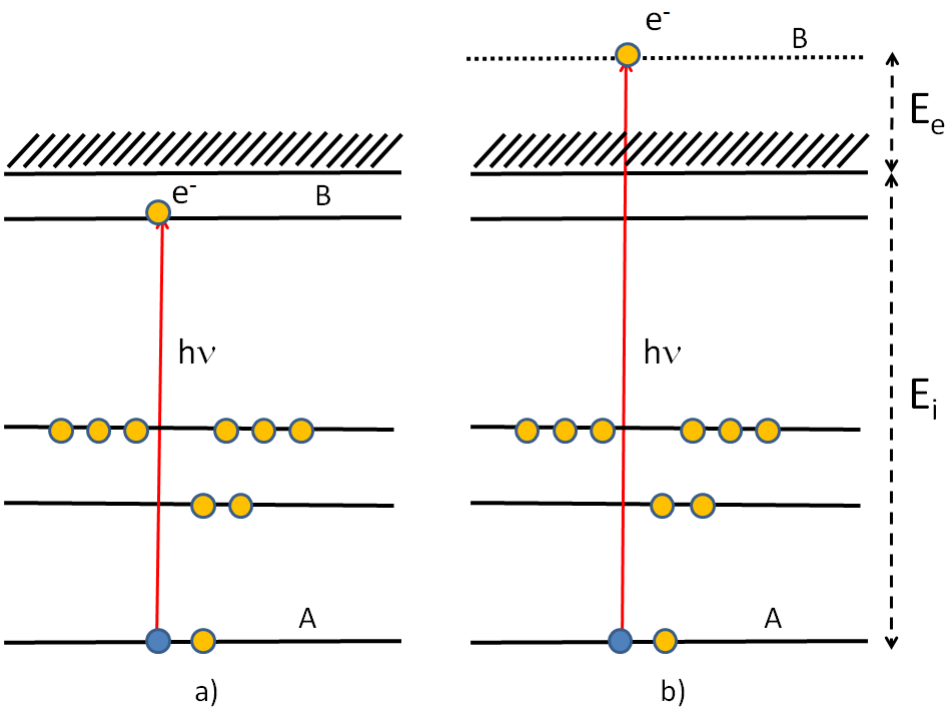

Figure 1.1: *In a) Photoexcitation by absorption of a photon energy $h\nu < E_i$ and in b) Photoionization of an atom by absorption of a photon with energy $h\nu > E_i$.*

The conservation of global energy during the absorption process results in the fact that the energy of state B above the ionization threshold E_e, that is also the final kinetic energy of the photoelectron, once it is separated from the ion, is related to the energy $h\nu$ of the incident photon and to the ionization energy E_i by the equation (recoil energy neglected [1]):

$$E_e = h\nu - E_i = \frac{1}{2} m_e v^2 \tag{1.21}$$

which, represents the Einstein's photoelectric effect. Because the final state belongs necessarily to a continuum (as a result of the continuous character of E_e), Fermi's golden rule allows us to calculate a photoionization rate and, consequently, after normalization to the flux associated with the incident photon, a photoionization cross-section.

Assuming the validity of the dipole approximation, the cross-section σ_{if} for a photoionizing transition due to an unpolarized beam of photons of energy $h\nu$ from an initial state $|i\rangle$ to a final state $|f\rangle$ [18] is given by:

$$\sigma_{if} = \frac{4\pi^2 \alpha a_0^2}{3} (h\nu) |M_{if}|^2 \tag{1.22}$$

where α is the fine structure constant, a_0 is the Bohr radius, $h\nu$ is the photon energy (in Rydberg units [2]) and the absolute square of the matrix element is:

[1] This is a simplification because the ion (with mass M) recoils upon the ejection of the photoelectron (with mass m_e) and the energy is split between the two particles by conserving the momentum. If recoil energy is taken into account, equation 1.21 reads as $E_e = (\frac{M}{m_e+M})[h\nu - E_i]$. The lighter the ion with respect to the electron mass the greater the recoil energy.

[2] 1 Ry = 13.6 eV

$$|M_{if}|^2 = \sum_{i,f} |\langle f| \sum_j \vec{r_j} |i\rangle|^2 \tag{1.23}$$

where $\vec{r_j}$ is the position of the jth electron.
The photoelectron angular distribution resulting from photoionization of state $|i\rangle$ by linearly polarized photons [18] leaving the ion in state $|j\rangle$ is given by:

$$\frac{d\sigma}{d\Omega} = \frac{\sigma}{4\pi}\left[\sum_{k=0}^{n}(\beta_{2k} P_{2k}(\cos\theta))\right] \tag{1.24}$$

where $d\sigma/d\Omega$ is the differential photoionization cross-section into the infinitesimal solid angle element $d\Omega$, n is the numer of photons involved in the process, σ the total (angle-integrated) cross section, θ is the angle between the photon polarization vector and the photoelectron momentum direction, $P_{2k}(x)$ are the Legendre polynomials, and β_{2k} are the asymmetry parameters.
Not all transitions are possible: only those that fulfill conservation of energy, angular momentum, and parity including also the emitted photoelectron in the final state (for the photoionization process). Table 1.4 illustrates the selection rules for electric dipole transitions [19].

Table 1.4: *Selection Rules for electric dipole transitions*[a]

Selection Rule	Remarks
$\Delta l = \pm 1$ for one-electron systems $\Delta L = \pm 1$ for multielectron systems with L-S coupling	Strictly valid
$\Delta M = 0, \pm 1$	$\Delta M = 0$: linear polarized light $\Delta M = \pm 1 : \sigma^+$ or σ^- circular polarized light
$\Delta S = 0$	Valid for light atoms. Exceptions for heavy atoms with large spin-orbit coupling.
$\Delta J = 0, \pm 1$	$J = 0 \rightarrow J = 0$ is forbidden.

[a] L-S: spin-orbit coupling. L: total orbital angular momentum. S: total electron Spin.
M: total z component of orbital angular momentum

1.3 Electron spectrometers

There are three fundamentals properties characterizing each emitted photoelectron: the kinetic energy, the direction of emission relative to the target and the incident radiation, and in general but not always measured, the spin orientation [1]. In details one is usually interested in:

1. *The photoelectron's kinetic energy distribution.* This measurement produces an electron spectrum or an energy distribution curve (PES). In most dispersive spec-

trometers this quantity is measured at fixed angles of electron emission (or over a small range of emission angles) [1].

2. *The photolectron's angular distribution.* Such an angular-resolved mesurements (AD) can be made relative to the radiation's electric field vector or to fixed axes with respect to the target. Generally this measurements require kinetic energy distributions determinations at different angles of emission [1].

3. *The photoelectron's spin distribution.* These measurements require a magnetically polarized target, usually by means of an external field, so that photoelectrons may be emitted with one of the two possible spin orientation. Then the relative numbers of spin-up and spin-down photoelectrons are measured [1]. Since this kind of measurements are not object of this thesis work, they will not be further discussed here.

The general considerations that govern the choice of an electron spectrometer are: (1) energy resolution in the PES, (2) efficiency, (3) unrestricted physical access to the sample possibly without breaking the vacuum, (4) ultra-high-vacuum capability (5) ease of construction. Various electron spectrometer are used in electron spectroscopy, and it is not the purpose of this section to give a detailed discussion of all of them, however a brief overview of the most used ones will be given beside a motivation for the choice made in view of the observables already defined.

1.3.1 Hemispherical Analyzer

The Hemispherical Analyzer (HA) is an electrostatic device used to disperse electrons as a function of their kinetic energy. This spectrometer consists of: an electrostatic lens system and two concentric hemispheres held at different potentials (see figure in 1.2).
The lens system is necessary to: image the sample on the hemispheres entrance plane; define the analyzed sample area and accepted solid angle on a sample; focus the particles into the analyzer entrance slit (w in figure 1.2) by accelerating or decelerating the particles to the pass energy (see later).
Particles enter the HA through narrow slits. The energy-dispersed electrons are detected at the exit of the HA, which is for construction at the same plane of the entrance plane, at the opposit point 180° around the HA.
Only the electrons with the right kinetic energy can pass the analyzer at a certain potential. If the electrons are traveling very fast they will hit the outer hemisphere and if their kinetic energy is very low they will hit the inner hemisphere. Thus only electrons within a very narrow energy region $E_e = E_0 \pm \Delta E/2$ will be able to pass through the whole analyzer to the detector. For this reason E_0 is also traditionally called Pass Energy (PE).

With respect to fig. 1.2 fundamental parameters are : V_1 internal hemispherical electrode, V_2 external hemispherical electrode. When collecting a negative charge V_2 is more negative than V_1. The potentials applied to the inner and outer hemispheres are defined by the pass energy E_0 chosen and the main parameters of the analyser: internal radius R_1, external radius R_2, mean radius $R_0 = (R_1 + R_2)/2$, entrance slit width w, incident angle α ($\alpha_{max} = \frac{w}{2R_0}$). The potentials of the inner and outer hemispheres are

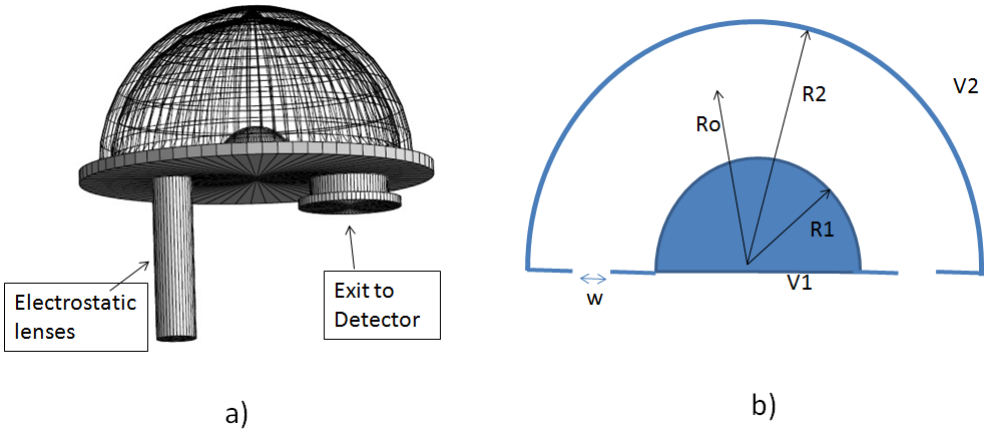

Figure 1.2: *In a) Drawing of a typical hemispherical analyzer and in b) Scheme of the fundamental parameters of the analyzer.*

given by:

$$V_1 = E_0[2R_0/R_1 - 1]\ ;\ V_2 = E_0[2R_0/R_2 - 1] \tag{1.25}$$

The pass energy resolution is defined as: $\Delta E = E_0[w/2R_0 + \alpha^2_{max}/4]$. The HA is able to provide PES with a very high resolution (typically 10 meV). The main disadvantages are that the angular acceptance is limited (typically about 8 degrees) and if an analysis of the AD of the emitted electrons is required the whole spectrometer has to be moved and the PES collected at each different angle.

1.3.2 Time-of-flight spectrometers and magnetic bottle spectrometers

The Time-Of-Flight (TOF) electron energy spectrometer consists of a field-free tube where the photoemitted electron fly in a region of ideally zero electric and magnetic field. A detector on one end of the tube collects the electrons. The kinetic energy of the electron is given by $E_{kin} = \frac{1}{2}m_e(\frac{L}{t})^2$, where t is the electron flight time, L the path lenght into the drift region and m_e the electron mass. By measuring the time of flight (for example with an oscilloscope) the energy of the electrons can be determined. The main advantage with this spectrometer is definitely the ease of contruction. The main disadvantage is that, as for the HA, to retrieve the angular emission information one has to move the whole spectrometer. In novel design of TOF electron spectrometers the use of position sensitive detectors allows the analysis of the particle's energy and momentum.

One particular evolution of TOF spectrometer is the magnetic bottle electron spectrometer (MBES), where a solenoid connected to a DC power supply is coiled around the drift tube and a strong cone-shaped permanent magnet is placed near the interaction region. The magnetic field produced by the solenoid is radially uniform inside. In a magnetic bottle electron spectrometer, one uses this effect to guide the charged particles, according to the Lorentz force $\vec{F} = q\vec{v} \times \vec{B}$, where q is the charge of the particle, $\vec{v}$ is the speed of the particle and $\vec{B}$ is the magnetic field. In an MBES a magnetic field is created around the TOF tube and the ionization region in the shape of a bottle - hence the name - and the electrons are adiabatically accelerated toward the detector. The basic idea in an MBES is the combined use of high and low magnetic fields to

direct all electrons created in a photoionization process to a distant detector and record the arriving time in comparison to a time reference. Since the travel distance and the electron mass are known, the time of flight can be converted to the kinetic energy of the detected electrons.The MBES is able to collect all electrons with a very high detection efficiency, high resolution and a much stronger signal compared to the plain TOF. The main disadvange of MBES is that the angular distribution of the emitted electrons cannot be recovered from the data.

1.3.3 Velocity map imaging spectrometers

The Velocity Map Imaging spectrometer (VMI) consists of a tube with the ionization region at one end and a detection system at the other. The ionization region lies between two electrodes with a high voltage difference between them. In this case the voltage difference is so high that the initial kinetic energy of the electrons can be neglected in the time-of-flight towards the detector. Instead it is the position where the electrons hit the detector, a multichannel plate and a CCD-camera, which brings information on the electron (a more detailed description of this spectrometer is given in chapter 3).
The question arises as to why a VMI spectrometer should be used instead of the HA, TOF, MBES analyzers previoulsy described. The VMI spectrometer is particularly well suited when dealing with light sources with a considerable focal spot size, such as synchrotron radiation (about 300 μm). Using such a spectrometer it is then possible to detect over a full acceptance angle (4π) and a larger interaction volume, and so increase the statistics and reduce the acquisition time [20]. Moreover with a VMI spectrometer it is possible to obtain not only an image of the velocity distribution of the charged particles emitted, but also the angular distribution without moving the whole spectrometer (which is the case for a HA) or by changing the polarization of the light [20]. For MBES, the angular distribution is not measured at all. On the other hand it is not possible to obtain direct information on the kinetic energy of a single particle. In fact the PES and AD can be calculated after acquisition by using image inversion techniques (for details see appendix A). The main disadvantage of using VMI with respect to HA and MBES are: the resolving power is limited to few percent of KE, the limited range of kinetic energies of the collected electrons and (in some cases, like e.g. the use with FELs) the sensitivity to scattered light and scattered electrons.

CHAPTER 2

Modern light sources

Photoionization studies of atoms, molecules and clusters by means of VUV and soft X-ray radiation have greatly benefited from advances in new experimental methods. In particular modern high-brightness light sources such as Synchrotrons and Free Electron Lasers have greatly increased the variety of experiments and also the range of accessible phenomena [18] whose study would be impossible without these sources. In this chapter the operating principles of these new light sources will be briefly presented, focusing in particular on the description of the Elettra Synchrotron and the FERMI Free Electron Laser where the results of this thesis work have been obtained.

2.1 Synchrotron Radiation

Particle accelerators have undergone extraordinary growth in the last few years. From their first usage in the 20's to now, there has been huge development: for example the particles' kinetic energy rose from a few hundred keV up to TeV (10^{12} eV). By 1960, not only the direct beam (generally composed of electrons or protons) but also the spontaneous radiation emitted by such particles had been used. This spontaneous emission is caused by the passage of the particles through the magnetic structure of the accelerator itself. This emission, called *Synchrotron Radiation* (SR), has very special properties such as: a wide continuous spectrum ranging from far Infrared to X-rays, high brilliance, picosecond pulse length, a highly collimated flux, variable polarization (linear, elliptical or circular). SR is nowadays the most common tool for a wide number of scientific applications in physics, chemistry, biology, life sciences, environmental science, medicine, forensic science, conservation of cultural heritage, etc....
In accelerator rings, the particle trajectory is constrained to a circular orbit, due to a magnetic field $\vec{B}$ acting on the particles having charge q and velocity $\vec{v}$ through the

Lorentz force (2.1) :

$$\frac{d\vec{p}}{dt} = \frac{d}{dt} m\gamma\vec{v} = q\vec{v} \wedge \vec{B} \tag{2.1}$$

where p is the particle momentum, γ the Lorentz's factor.[1] Since the force is perpendicular to the velocity, it bends particle trajectories without exchanging energy with the particles (in a classical mechanical model). Thus the charged particles moving in a uniform magnetic field describe a circular orbit. This is the basic construction principle of circular accelerators, which constrains particles to move in a circular orbit, where an additional electrostatic field then accelerates them.
Since the end of the 1800s the idea that a charged particle, when accelerated, emits energy (within an electromagnetic model) was well understood. In fact Larmor wrote the relationship between the *emitted power* (P) and *acceleration* ($\vec{a}$) of a particle with *electric charge q*. Later the classic Larmor formulation was relativistically generalized as in eq. (2.2) :

$$P = \frac{2}{3}\frac{q^2}{4\pi\varepsilon_0 c^3} c^2\gamma^4[\gamma^2(\vec{\beta}\cdot\frac{d\vec{\beta}}{dt})^2 + (\frac{d\beta}{dt})^2] \tag{2.2}$$

Where $\vec{\beta}$ is the relative speed with respect to the speed of light in vacuum c [2] and with ε_0 the dielectric constant .
It is noteworthy from 2.2 that the emitted power is proportional to the fourth power of $\gamma = E/mc^2$ indicating that for lighter particles (i.e. electrons) the emitted power P is higher. In a circular accelerator the centripetal acceleration is perpendicular to the direction of the velocity, $\frac{d\vec{\beta}}{dt} \perp \vec{\beta}$ and, neglecting the much smaller longitudinal acceleration, the emitted power is thus given by:

$$P = \frac{2}{3}\frac{q^2}{4\pi\varepsilon_0 c}\gamma^4(\frac{d\beta}{dt})^2 \tag{2.3}$$

the quantity $\frac{d\beta}{dt}$ is equal to $\vec{\omega}\wedge\vec{\beta}$, so that, with *R* the radius of curvature, the acceleration can be written as $\frac{d\beta}{dt} = \beta^2 c/R$ and P becomes:

$$P = \frac{2}{3}\frac{q^2}{4\pi\varepsilon_0} c\frac{\beta^4\gamma^4}{R^2} \tag{2.4}$$

If $T = (2\pi R)/(c\beta)$ is the period, then then the particle energy loss δE in one cycle is:

$$\delta E = P\frac{2\pi R}{c\beta} = \frac{q^2}{3\varepsilon_0}\frac{\beta^3\gamma^4}{R} \tag{2.5}$$

which can be finally written in more practical units as follows:

$$\delta E(MeV) = 8.85\cdot 10^{-2}\frac{[E(GeV)]^4}{R(m)} \tag{2.6}$$

In order to keep the particle in the closed trajectory this energy loss must be supplied again, which is accomplished by the Radio Frequency Cavities. The RF cavity determines the temporal structure of the SR light.

[1] Lorentz's factor: $\gamma = \frac{1}{\sqrt{1-(\frac{v}{c})^2}}$.

[2] c = 299 792 458 m/s

The spectrum of the emitted SR (see figure 2.1), typically, shows significant fluxes over a range of about 3 times the critical frequency parameter (ω_c), which is described by the following expression:

$$\omega_c = \frac{3}{2}\frac{c}{R}\gamma^3 \tag{2.7}$$

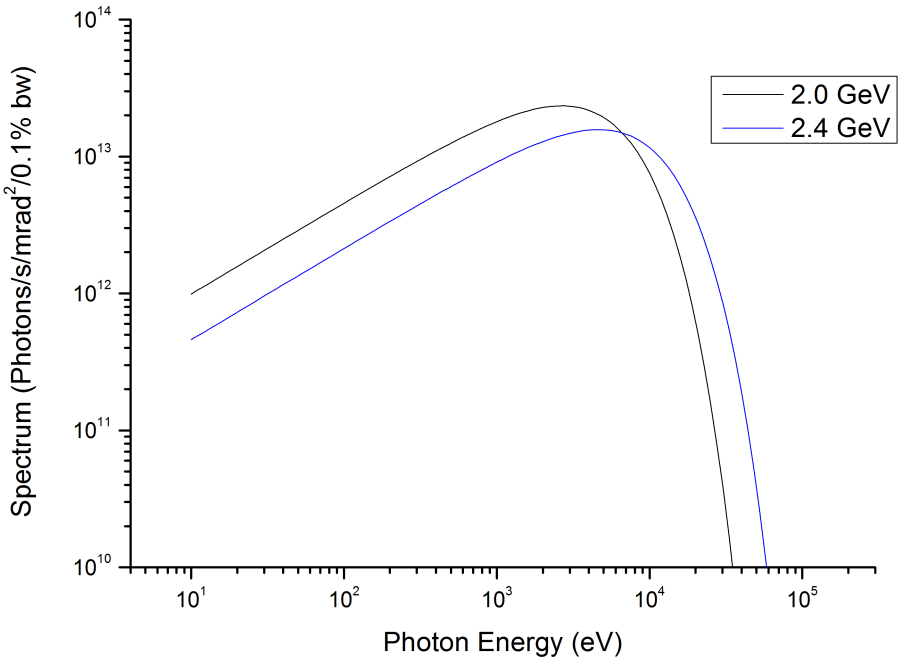

Figure 2.1: *Typical bending magnet spectrum calculated, according to the Elettra main parameters [21], for 2 and 2.4 GeV using the CXRO web interface [22].*

The historical development of synchrotron radiation sources has proceeded through three steps which are known as the three generations of synchrotron radiation sources [23]:

First Generation The Storage Rings of this generation were originally built for high energy research. The synchrotron radiation programs started in a parasitic mode.

Second Generation The sources of this generation were designed specifically to produce synchrotron light. These rings are characterized by a large number of beamlines.

Third Generation The rings of this generation have lower emittance and many straight sections for the so called *insertion devices* (ID) designed to extend the spectral range and increase the brightness with respect to those of the second generation.

The last generation was necessary to overcome a limitation reconsidered during the second world war by Iwanenko and Pomeranchuk: the radiation emitted by particles moving on circular paths and the consequently energy loss may pose a limit on the

maximum energy attainable with a circular accelerator [23]. By using ID such as wigglers or undulators in the straight sections one forces the electrons to radiate [23]. The characteristics of the emitted radiation from wiggler or undulator magnets, the most commonly used ID, are not the same. The bending magnets, or dipoles, bend the electron beam through short arcs. The electrons moving in bending magnets describe a circular orbit and produce a broad-band smooth spectrum. An observer placed on axis will receive a stream of photons for a very short time, and will therefore measure a narrow electric field in the time domain corresponding to a broad-band in the frequency domain [23].
Wigglers are essentially a sequence of bending magnets with alternate polarities. The emitted radiation has spectral characteristics analogous to those of bending magnets, with an enhancement of a factor $2N$, where $2N$ is the number of poles. The measured field will consist of a series of distinct sharp peaks in the time domain and of a broad-band spectrum in the frequency domain [23].
Wigglers and undulators use a very similar magnet technology. Typically undulators have many more periods. The main difference is in the emission angle: in an undulator the emission angle is much smaller than the natural emission one, while for a wiggler the opposite is true. Then in an undulator the electrons propagate executing smooth transverse oscillations, keeping into the emitted radiation cone in any point of the trajectory. As a result of the interference between radiation emitted from different points of the trajectory, the spectrum consists of a series of quasi-monochromatic peaks. So the on axis observer will receive an almost continuous signal in the time domain, while in the frequency domain the spectrum consists into a series of harmonics [23]. Since this kind of ID is also the basic component of a FEL light source it will be described more in details in section 2.2.

2.1.1 Elettra

Elettra is the Italian synchrotron radiation facility in Trieste (see figure 2.2), it is a third generation storage ring (2 and 2.4 GeV) that has been operating since October 1993. It is optimised to provide photons in the energy range from a few to several tens of keV with a spectral brightness up to 10^{19} photons/s/mm^2/mrad^2/0.1%bw and is continuously upgraded in order to be competitive with the most recent light sources.
Recently a new upgrade allows operating in top-up mode, which consists of a constant reinjection of electrons lost during operation. This top-up mode results in an almost constant light intensity, an increased average brightness over time and a much greater spatial stability of the beam.
Currently 26 beamlines, utilize the radiation generated by the Elettra source, covering a wide number of areas such as spectroscopy, diffraction, scattering, lithography, infrared microscopy and spectroscopy, and UV inelastic scattering [21]. The main beam parameters of Elettra are summarized in table 2.1 [21]:

2.2 Free Electron Lasers

Free Electron Laser (FEL) is a novel type of light source in the VUV and X-ray spectral region. The principle is rather simple and builds on undulator radiation.
As in the case of a synchrotron radiation facility, an electron beam is produced by an

Figure 2.2: *The Elettra Synchrotron Radiation and Free Electron Laser Facility in Trieste. Panoramic view [21].*

Table 2.1: *Elettra storage ring parameters [21].*

Beam Parameters	**Values**
Energy range	0.75-2.5 GeV
Injection Energy	All energies up to 2.5 GeV
User Operating Energy	2.0 GeV (75% of user time) 2.4 GeV (25% of user time) 1.0 GeV (SR-FEL)
Critical energy	3.2 keV at 2.0 GeV 5.5 keV at 2.4 GeV
Operating mode	Top-up
Operating current (user request)	300 mA at 2.0 GeV (lifetime 26 h) 140 mA at 2.4 GeV (lifetime 40 h)
Top-up injection rate	1 mA every 6 min at 2.0 GeV 1 mA every 20 min at 2.4 GeV
Filling pattern	Any (single, few, multi etc.); most requested multibunch filled at 95% of the ring circumference (864 ns) and hybrid (multibunch with a single bunch in the dark gap)
Bucket size [a](in multi-bunch)	2 ns
Dark gap when filled at 95%	43 ns

[a]The Bucket size is the bunch to bunch temporal separation

electron gun and passes through an electron accelerator, before entering a long series of undulators.
Undulators are a type of ID (see the previuos section), particular components built to generate radiation with specific characteristics.
Undulators consist of a series of alternating magnet poles deflecting the beam periodically in opposite directions, or in a spiral path, as shown in Fig. 2.3.

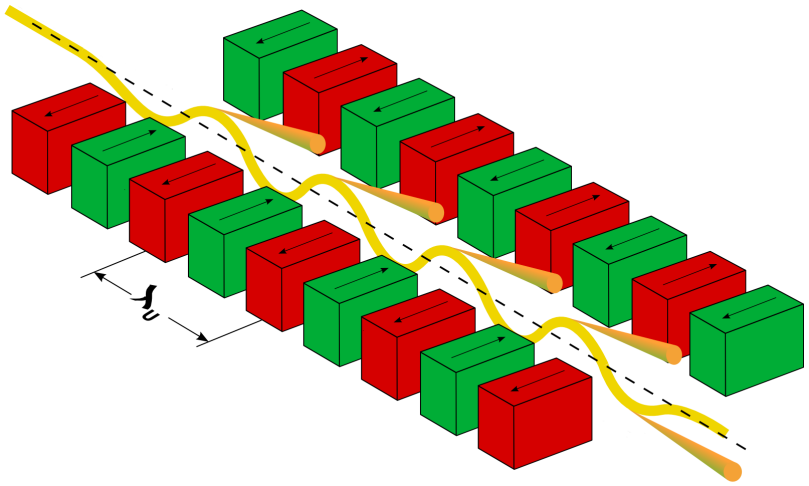

Figure 2.3: *Scheme of an Undulator.*

The k-th harmonic undulator radiation can be described mathematically by the following equation [24]:

$$\lambda_s = \frac{\lambda_u}{2\gamma^2 k}[1 + \frac{K^2}{2} + (\gamma\theta)^2] \tag{2.8}$$

where λ_s is the positive interference wavelength, λ_u the undulator period, k the harmonic number, θ the angle between the emitted light and the central orbit, γ the Lorentz factor and K the undulator strength parameter which can be expressed as:

$$K = \frac{\lambda_u e B_0}{2\pi m_e c\gamma} \tag{2.9}$$

where B_0 is the magnetic field strength, e the elementary charge and m_e the electron mass [24]. The basic concept for understanding the working principle of a FEL is the interaction between the electron beam and the radiation field. In Self Amplified Spontaneous Emission (SASE) FELs, an electron travelling along the undulator emits spontaneous radiation which is relatively weak and incoherent. The electron beam is narrow and collimated so it co-propagates with the light, and the electron beam can interact with the emitted light. If the electron and the light field are matched in phase, and are pointing in the same direction, the electron loses energy which is transferred to the light field. If the phases are different, the electron gains energy. After a short time, the more energetic electrons catch up with the less energetic ones; the electron beam consists now of bunches of electrons spaced with the light wavelength. The waves radiated by the initially random electrons then add in phase with one another. The bunches are in phase with the incident light field, the emission of the bunches adds coherently to the light field and amplifies it. This interaction is called *micro-bunching*. At resonant conditions, the electron beam and the radiation field can exchange energy over several undulator periods, which can lead to a net gain of energy in the radiation field. One of the major features of an FEL is its high brilliance, notably in the X-ray region which is not available at other light sources. Because of its transverse coherence, the FEL is diffraction limited (at saturation). The longitudinal coherence is comparatively poor and affect the repeatability of the pulse structure, i.e. each pulse is different. The

high brilliance makes it challenging to find suitable materials for measuring the emitted light, splitting the light or even measure calibration spectra directly. A new generation of FEL, seeded Free Electron Lasers, consists of two series of undulators separated by a chicane, where the conversion between energy and density modulation can be done. A laser pulse can also be introduced to induce an energy modulation and thus seed the photon emission. This technique is called High-Gain Harmonic-Generation (HGHG), and is designed to convert the fundamental frequency of the laser to a much higher frequency. The first undulator is used as a modulator, the chicane compresses the bunches (which enhances further the density modulation), and in the second undulator the lasing process occurs. This geometry gives an intense fundamental mode which is narrow and has better shot-to-shot repeatability.

2.2.1 FERMI

FERMI is a seeded FEL user-facility which comprises two different coherent radiation sources, FEL-1 and FEL-2 designed to cover respectively the wavelength range from 100 nm to 20 nm and from 20 nm to 4 nm in the first harmonic. FERMI uses a linear accelerator to generate a beam of relativistic electrons that is made to propagate through a long series of undulators. An initial seed signal, provided by a conventional, high peak power, pulsed laser operating at 200-280 nm at the repetition frequency of the electron bunches, is temporally synchronized to overlap the electron beam, produced by the linac accelerator, in a first undulator section called the modulator (MOD). The laser field modulates the transversely wiggling electron bunch energy at its own frequency. This energy modulation is then converted to a modulation of the spatial charge density by passing the electrons through a chromatic dispersive section. The resultant density modulation contains higher harmonics of the seed laser wavelength. A subsequent set of undulators, named the radiators (RAD), is tuned in magnetic strength so that intense, coherent FEL radiation at a wavelength corresponding to one of these harmonics is emitted and then amplified to a high peak power level [25]. The temporal duration of the FEL radiation is approximately that of the seed laser and the polarization properties (linear, elliptical) are determined by the magnetic field pattern of the radiators (planar, helical).

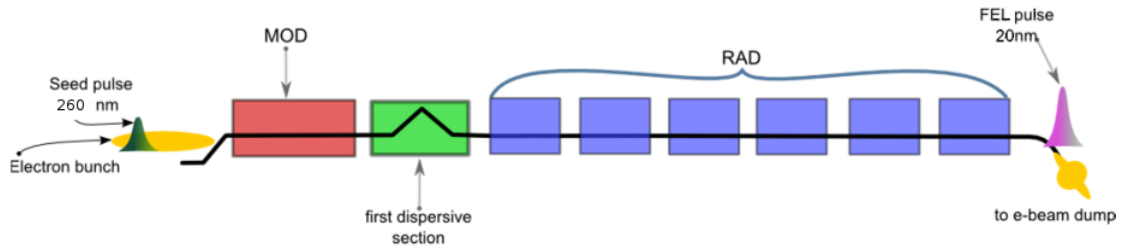

Figure 2.4: *FERMI FEL-1 conceptual scheme. Picture from the website [25].*

Among existing FEL sources FERMI is unique in many respects: very high peak flux (comparable to SASE FELs) and higher 6D brightness; high temporal and transverse coherence of the FEL pulse; control of the time duration, polarization, wavelength and bandwidth of the coherent FEL pulse. Close to transform-limit pulses provide ex-

cellent resolving power without monochromators. Natural synchronization of the FEL pulse to the seed laser is also achieved. An additional benefit is the reduction in undulator length needed to achieve saturation as compared to starting from noise as in SASE FELs. The main FERMI beam parameters are summarized in table 2.2 [21].

Table 2.2: *FERMI free electron laser parameters*

Beam Parameters	**Values**
Electron beam energy range	1-1.5 GeV
Bunch charge	500-800 pC
Bunch peak current	400-600 A
Wavelength (FEL-1) Wavelength (FEL-2)	100-20 nm (12-60 eV) 20-4 nm (60-300 eV)
Relative bandwidth	10^{-4}
Average energy per pulse	10-200 μ J
Photon pulse	30-100 fs
Polarization	H, V, CR, CL
λ (seed)	200-280 nm
Repetition rate	10 Hz

CHAPTER 3

Experimental methods

In this chapter an overview of the instruments (spectrometers and diamond detector) used in this thesis work is given. In particular the first section is dedicated to the Velocity Map Imaging technique and its operating principle. A second section is dedicated to Time-Of-Flight spectrometers for mass-charge ratio discrimination. Also the PhotoElectron-PhotoIon Coincidence (PEPICO) technique, which is particularly useful when investigating clustered system, will be introduced. Finally the last section is dedicated to illustrate the working principle of novel diamond photon beam monitors.

3.1 The Velocity Map Imaging technique

Velocity Map Imaging (VMI) is a technique introduced in 1997 by Eppink and Parker [26] who modified the traditional design of a Time-Of-Flight spectrometer using circular electrodes with a hole in the center (see figure 3.1) instead of using traditional accelerating grids producing a uniform electric field.

Adopting this geometry the electric fields are no longer uniform as can be seen in 3.1 b). The main advantage of such a scheme is that, with proper choice of the applied potentials, a focusing effect is obtained: electrons or charged particles in general emitted with the same transverse momentum (same kinetic energy and same ejection angle) arrive in the same spatial region of a 2D detector (as displayed in figure 3.2), even if emitted from different spatial regions.

The interaction region is between the Repeller (R) and the Extractor (E) electrodes (see 3.1 a)). Focused radiation ionizes the atoms in the gas and electrons are emitted leaving the atom in a ionized state. The direction of the electrons depends on the orbital from which they are emitted and from the energy and polarization of the incident light. The electric fields are chosen so that electrons are pushed toward the detector. The

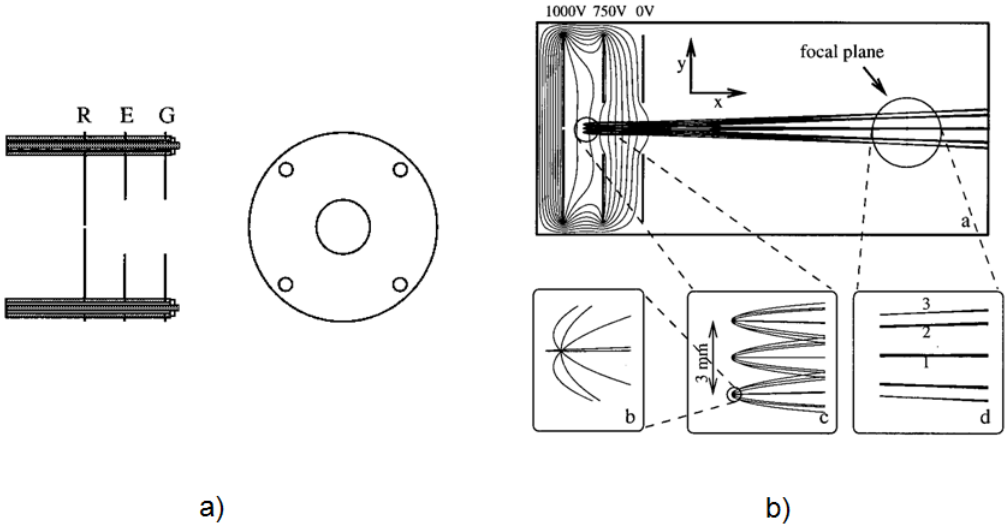

Figure 3.1: *Scheme of the VMI techinque. In a) the electrodes with circular holes and in b) the electric field present in the VMI system and particles' trajectories where 1, 2 and 3 correspond to ejection angles 0/180° (x direction), 45/135° and 90° (y direction), respectively. Figure taken from the original work of Eppink and Parker [26].*

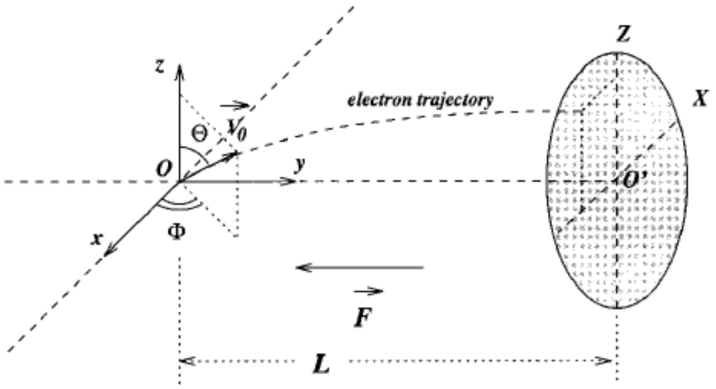

Figure 3.2: *The detector's plane is X,Z, L is the detector-ionization point distance, the Z axis is along the light polarization and the source beam propagation. Figure taken from [27].*

electron cloud keeps expanding radially arriving at the detector plane in a circle of a few cm diameter [20]. The larger the transverse kinetic energy momentum the larger the radial position on the detector. The radius R at which the electron hits the detector is directly proportional to the electron's initial velocity v_0 according to the following relation $R = v_0 t$, where t is the time of flight [20]. In the direction along the y axis the electron's velocity is given by:

$$v_y = \sqrt{\frac{2T_E}{m}} \tag{3.1}$$

where $T_E = qV$ represents the kinetic energy gained by the electron accelerated by the potential V. If the field component in the ZX plane can be neglected and if the total length L of the spectrometer is large compared to the acceleration region, the time

of flight t can be approximated [20] as:

$$t \approx \frac{L}{v_y} = L\sqrt{\frac{m}{2qV}} \tag{3.2}$$

the radius $R = v_0 t$ will be connected to the initial electron's kinetic energy by:

$$R \approx L\sqrt{\frac{T_0}{qV}} \tag{3.3}$$

where $T_0 = \frac{1}{2}mv_0^2$. Since the electric field is not just directed along the Y axis but also slightly radially, the component of the field in the ZX plane only contributes with a magnification by a factor N [20]. So finally:

$$R \approx NL\sqrt{\frac{T_0}{qV}} \tag{3.4}$$

The magnification factor must be determined through a calibration for each voltage setting applied, by taking images at different photon energies (and therefore different kinetic energies). We actually follow this procedure before any experiment (see section 5.1.1). The focusing conditions are found by choosing a proper ratio of the voltages applied to the Extractor and Repeller electrodes. This procedure is usually done by simulating the charged particle trajectories using a simulation software package such as SIMION [28]. Then starting from the value obtained by the simulation an optimisation has to be performed by acquiring images, adjusting the Extractor and Repeller voltages and analysing the images in order to evaluate the best focusing conditions. With such a spectromter it is not possible to obtain direct information on the kinetic energy of a single particle. In fact the kinetic energy spectrum (PES) and Angular Distributions (AD) can be calculated after acquisition by using image inversion techniques (Abel transform), provided the system has an axis of symmetry. These techniques allow one to retrieve the full 3D velocity distribution information starting from a 2D image collected by the spectrometer [20](for more details on the inverse Abel transform see appendix A).

3.2 The Time-Of-Flight mass spectrometer

The Time-Of-Flight ion mass spectrometer (TOF MS) has the simplest design among all mass spectrometers devoted to distinguish gaseous ions according to their mass-charge ratio [18]. The TOF MS was developed in 1946, but until the late 1990s its popularity was limited by the lack of technologies to facilitate recording and processing of the mass spectrum on a micro-second time scale [29]. The main idea is based on the fact that ions with the same energy and different masses travel with different velocities. Basically, ions formed by photoionisation are accelerated by an electrostatic field to a common energy and travel over a field free path to the detector. Measuring the flight time for each ion allows the determination of its mass. The TOF scheme is generally based on the original design of Wiley and McLaren [30] and consists of three sections: the ionization section, the acceleration section and the field-free section (see 3.3). In early TOF mass spectrometers, there were only two regions: the first one used to extract

the ions with an accelerating potential that varies over the interaction volume, and the field-free (drift) region. Since the ions acquire energy from the extraction potential, the kinetic energy varies accordingly. Therefore, the velocities of ions produced at different locations differ, which smears out the arrival times and limits the mass resolution [19]. In order to improve this, a modification of the extraction field was introduced by Wiley and McLaren [30]. As described in their paper the acceleration occurs in two steps: the first one in the interaction region and the second one in the acceleration region. The voltages ϕ_1 and ϕ_2 applied to grids G1 and G2, defining respectively the electric fields E_1 and E_2, are chosen so that particles with the same mass-charge ratio emitted from an extended region in the interaction section arrive at the same time at a detector at the end of the field-free region in the drift tube kept at potential $\phi_3 = 0$.

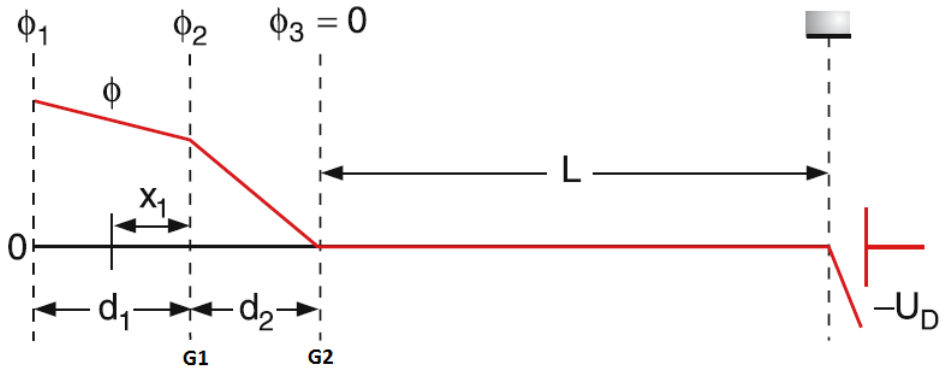

Figure 3.3: *Time-Of-Flight spectrometer scheme in a Wiley - McLaren configuration. Figure taken from [19].*

Considering at time $t = 0$ a positive ion with charge q and mass m produced in a small volume of the interaction region (d_1), at distance x_1 from the grid G1, with initial velocity $v_0 = 0$, the flight time t_1 is determined by the kinetic energy to which the ion is accelerated [19]:

$$x_1 = \frac{1}{2}\frac{qE_1}{m}t_1^2 \Rightarrow t_1 = \sqrt{\frac{2mx_1}{qE_1}} \tag{3.5}$$

So at grid G1 the ion has acquired the velocity $v_1 = \frac{qE_1}{m}t_1$ and at grid G2 the ion has acquired the velocity $v_2 = \sqrt{v_1 + \frac{qE_2}{m}t_2}$, where t_2 is the time interval between G1 and G2.

$$\begin{aligned} d_2 &= \int_{t_1}^{t_1+t_2} v dt = \int_{t_1}^{t_1+t_2} (v_1 + \frac{qE_2}{m}t)dt = \\ &= v_1 t_2 + \frac{1}{2}\frac{qE_2}{m}(2t_1t_2 + t_2^2) = \\ &= \frac{q}{m}[(E_1 + E_2)t_1t_2 + \frac{1}{2}E_2t_2^2] \end{aligned} \tag{3.6}$$

Resolving for t_2 and substituting for t_1 the expression found in 3.5 we obtain:

$$t_2 = \sqrt{\frac{2m}{q}}\frac{1}{\sqrt{E_1}}\frac{1}{E_2}[-(E_1+E_2)\sqrt{x_1} + \sqrt{(E_1+E_2)^2 x_1 + 2E_1E_2d_2}] \tag{3.7}$$

The drift time across the field-free region is $t_3 = L/v_2$, and the total time of flight t is $t = t_1 + t_2 + t_3$. Substituting the expressions for t_1 from eq. 3.5 and for t_2 from eq. 3.7 we immediately see that $t \propto \sqrt{\frac{m}{q}}$. Then for a fixed charge q and acceleration voltage V, the dependence of the mass is quadratic with the arrival time t at the detector. The mass resolution $m/\Delta m$ depends on the shortest time interval Δt that can be resolved as follows [19]:

$$\frac{\Delta m}{m} = 2\frac{\Delta t}{t} \tag{3.8}$$

The conditions for which the total time t is not dependent on the location x of ion production, called spatial focusing condition or Wiley-McLaren condition [30], are obeyed if $\frac{dt}{dx_1} = 0$. This derivative yields the optimum flight path length $L = L_{opt}$ in the field-free region from the grid G2 to the detector, which is:

$$L_{opt} = d_1 k^{3/2}(1 - \frac{d_2}{d_1}\frac{1}{k+\sqrt{k}}) \tag{3.9}$$

where

$$\begin{aligned} k &= 1 + \frac{2d_2}{d_1}\frac{E_2}{E_1} = 1 + 2\frac{V_2}{V_1} \\ V_1 &= \phi_2 - \phi_1 \; ; \; V_2 = \phi_3 - \phi_2 \end{aligned} \tag{3.10}$$

TOF MS are widely used since the construction of the apparatus is very simple, ions of all species can be simultaneously observed and the ion collection efficiency is very high with respect to the other types of mass spectrometers such as magnetic sector, quadrupole mass spectrometers, and others.

By combining mass spectrometry and photoelectron spectroscopy it possible to perform so called photoelectron-photoion coincidence spectroscopy (PEPICO). Whenever a photoelectron is detected, we know that also a photoion has been formed in the same photoionization event. The precise moment can be located in time usually within some 20 or few hundreds of ns earlier [31], depending on the electron detection method. The form of the PEPICO technique used in this study consists in an analysis post acquisition: during the measurement all the events are recorded, within a time window, using an internal trigger as start. Then for each ion collected (with arrival time t_{ion}) the software searches for the last electron recorded (arrival time $t_{electron}$) before the ion event. Once the electron-ion pairs have been individuated, for each of them the difference $t_{ion} - t_{electron}$ is calculated, this time difference is assumed as the time-of-flight of the ion. Then an histogram with the time-of-flight is realized. If the arrival time of electrons and ions is uncorrelated, the time-of-flight histogram would be a decreasing exponential curve with a constant decay time τ given by the reciprocal of the electron count rate. On the contrary if the arrival time of electrons and ions is correlated a well defined peak appears in the histogram plot. This is the general PEPICO technique used

to determine electron-ion pairs occuring from the same event. Since we use a VMI electron spectrometer it is also possible to select the position (and thus the kinetic energy) of the electron in coincidence with a specific ionic mass. The use of a high repetition rate UV light source such as SR is particularly important because it allows the production of electron-ion pairs at random instants so that a realistic distribution of events can be obtained.

3.3 Diamond-based photon beam monitors

SR and FEL light sources require novel concepts of beam diagnostics to keep photon beams under surveillance, calling for simultaneous position and intensity monitoring. To deal with the high power load and short time pulses provided by these sources, novel materials and methods are needed for the next generation Beam Position Monitors (BPM) [32, 33].
The most used technique is based on photocurrent measurements. A photoconductor is an element of semiconducting or insulating material provided with two electrical contacts, capable of detecting the passage of photons through the change of a physical characteristic, the conductivity. Radiation with energy above the band gap interacts with the diamond material creating e/h pairs and resulting in an increase of the conductivity. Providing the bulk with metallic electrods by means of standard thermal evaporation techniques and applying a voltage between the electrodes the charge produced in the material can be collected very fast.

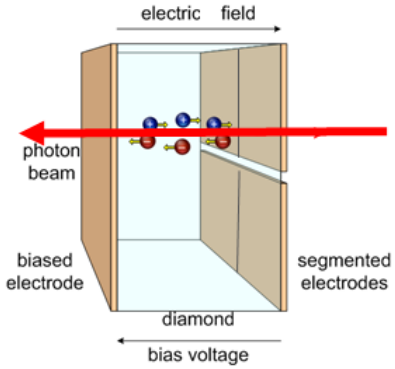

Figure 3.4: *Scheme of the working principle of diamond beam monitors [32, 33].*

The electric current generated in a photoconductor has the following expression:

$$I_{ph} = qn\theta\eta\frac{\mu\tau E}{L} \tag{3.11}$$

where q is the charge, n the number of photons per unit time, η is the quantum efficiency, θ is the quantum yield [1], μ is the carrier mobility, τ the recombination time of the photo-generated charges,E the electric field, L the distance between the electrodes. The quantity $\mu\tau E$ is called the charge collection distance (d), and it is defined as the distance travelled by the particle during its mean lifetime.

[1] Quantum yield: represent the number of electrons generated for each impinging photon ata a given energy considering that the minimum energy for e/h pair production in diamond is w = 13.6 eV.

Then the above equation can be written as:

$$I_{ph} = I_{ph,p}\frac{d}{L} \tag{3.12}$$

calling $I_{ph,p}$ the primary current, the photo-conductive gain (G) results:

$$G = \frac{I_{ph}}{I_{ph,p}} = \frac{\mu\tau E}{L} = \frac{d}{L} = \frac{\tau}{t_r} \tag{3.13}$$

where t_r is the time spent by the charge to travel from an electrode to the opposite one. It is easy to observe that in order to get a high photo-conductive gain it is necessary to have high mean lifetime and carrier drift speed ($V_d = \mu E$). This implies that the bulk material has to be as perfect as possible not only in terms of the lattice geometry, but also from the chemical purity point of view. In fact crystal imperfections (dislocations, lattice vacancies, etc ...) and impurities introduce intra-gap energy levels between the valence and the conduction band decreasing the drift velocity and the mean lifetime of the carriers [34].
By using segmented electrodes it is possible to detect the incident beam position as reported in the scheme of Fig. 3.5.

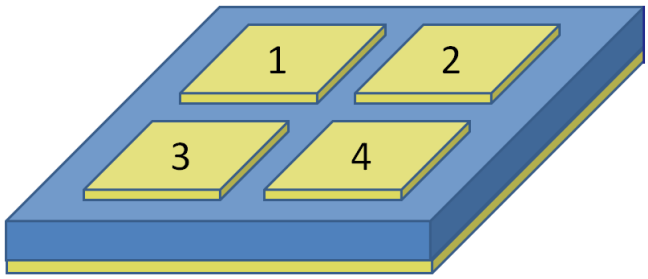

Figure 3.5: *Scheme of the segmented electrodes on diamond bulk surface.*

The position of the incident beam can be reconstruced by using the *difference-over-sum* technique that allows one to calculate the beam centroid position, by acquiring simoultaneously the current (I_i with i=1..4 for a 4-quadrant geometry) from each electrode. In the case of 4-quadrant geometry then the horizontal and vertical position of the beam centroid are calculated as follows:

$$\begin{aligned} Horizontal &= \frac{I_L - I_R}{I_L + I_R} = \frac{(I_1 + I_3) - (I_2 + I_4)}{(I_1 + I_3) + (I_2 + I_4)} \\ Vertical &= \frac{I_U - I_D}{I_U + I_D} = \frac{(I_1 + I_2) - (I_3 + I_4)}{(I_1 + I_2) + (I_3 + I_4)} \end{aligned} \tag{3.14}$$

where I_L is the sum of the current of Left electrodes (I_1 and I_3), I_R is the sum of the current of Right electrodes (I_2 and I_4), I_U is the sum of the current of Upper electrodes (I_1 and I_2), I_D is the sum of the current of Lower electrodes (I_3 and I_4).
The sum of all the currents $I_{tot} = \sum_{i=1}^{4} I_i$ is used to monitor the intensity of impinging light after dark current subtraction.
Because of its unique physical and electronic properties diamond is the most promising

material for the production of semitransparent in situ pBPMs [32,33]. A brief overview of the chemical and physical properties is given in comparison with the most common materials, Silicon and Germanium, used as active materials in this technology as reported in the table below.

	Diamond	**Silicon**	**Germanium**
Atomic weight	12.1	28.09	72.6
Nearest neighbour distance [Å]	1.54	2.35	2.45
Number of atoms[$\times 10^{22}$ cm^{-3}]	17.7	4.96	4.41
Compressibility [$\times 10^{11}$ m^2 N^{-1}]	0.226	1.012	1.29
Density [g cm^{-3}]	3.51	2.34	5.33
Melting point[$^\circ$C]	3350	1410	973
Band gap energy [eV]	5.47	1.12	0.665
Breakdown voltage [V]	1×10^7	3×10^3	1×10^3
Resistivity [Ω cm]	$> 10^{13}$	2.3×10^5	47
Electron Mobility[cm^{2}V^{-1}s^{-1}]	1800	1350	3900
Hole Mobility [cm^{2}V^{-1}s^{-1}]	1200	480	1900
Young modulus [GPa]	1134	131	103
Thermal conductivity [Wcm^{-1}K^{-1}]	20	1.27	0.653

Table 3.1: *Main physico-chemical properties of Diamond, Silicon and Germanium.*

Chemical and structural properties: diamond is a crystallized allotropic form of carbon, composed by carbon atoms connected toghether with hybrid covalent bonds sp^3 in a tetrahedral geometry. The reduced inter-atomic distance (1.54 Å) and high atomic density (0.176 Å^{-3}) give this material a large binding energy. These characteristics are reflected in an extraordinary compactness, hardness and low compressibility. In addition, the particular chemical bond makes this material particularly resistant to damage from radiation and chemically inert.

Optical, thermal and electrical properties: Diamond is characterized by a high energy gap (5.47 eV), which makes it an excellent insulator (if pure), transparent to a wide spectral region from 225 nm to far-infrared. This transparency also determines the poor sensitivity of these detectors at wavelengths greater than 225 nm, this feature is known as *visible blindness.*

From an electrical point of view the wide energy gap between the valence and the conduction bands reduces significatively the number of free charges that, at room temperature, are present in the conduction bands; for this reason electronics based on this material are characterized by low thermal noise. The high mobility of carriers, together with a small dielectric constant, makes it an ideal material to produce very fast response time devices. The high value of the breakdown voltage allows the use of micro-electrical structures even at high voltage gradients.

Finally, diamond has a thermal conductivity of 2000 Wm^{-1}K^{-1} (compared to 390 Wm^{-1}K^{-1} of copper) that allows a quick heat dissipation, making it suitable to operate in vacuum and high thermal stress enviroments.

CHAPTER 4

Experimental setup

This chapter represents the core of my doctoral work. The experimental results displayed have been acquired with two distinct, but conceptually similar, setups. In fact, depending on the different gaseous targets under study the scheme changes only in the source chamber section. This chapter is split into SR experimental setup and FEL experimental setup sections with a description of the main light source parameters of the two beamlines where the results have been obtained, focusing on the different position sensitive detectors used.
Independently of the source beam or target, both SR and FEL experimental setups are based on a Velocity Map Imaging spectrometer and a Time-of-flight spectrometer, whose working principles have been described in the previous chapter. The general experimental scheme is reported in figure 4.1.

The experimental conceptual scheme changes only in the position sensitive detector (PSD) part, depending on the light source used because of the different event rates per photon pulse expected at SR and FEL facilities.
In the following sections will be described, details of the different experimental setups using the following reference scheme. Photoelectrons induced by photoionization go upward, entering the Velocity Map Imaging focusing system (see chapter 3 for details) and are collected by a 2D PSD detector. Meanwhile the photoions, slower than the electrons, go downward entering the Time-Of-Flight Spectrometer (TOF) for the mass-charge ratio discrimination (chapter 3). The availability of this state-of-the-art detection system allowed not only a deeper comprehension of the electronic structure of matter, but also deeper characterization of novel light sources as the FEL FERMI. This close and mutual interaction between new detectors and new light sources has resulted in a continuous development of both systems. In order to provide users with important and quantitative information (i. e., beam position, intensity, beam temporal structure, etc...)

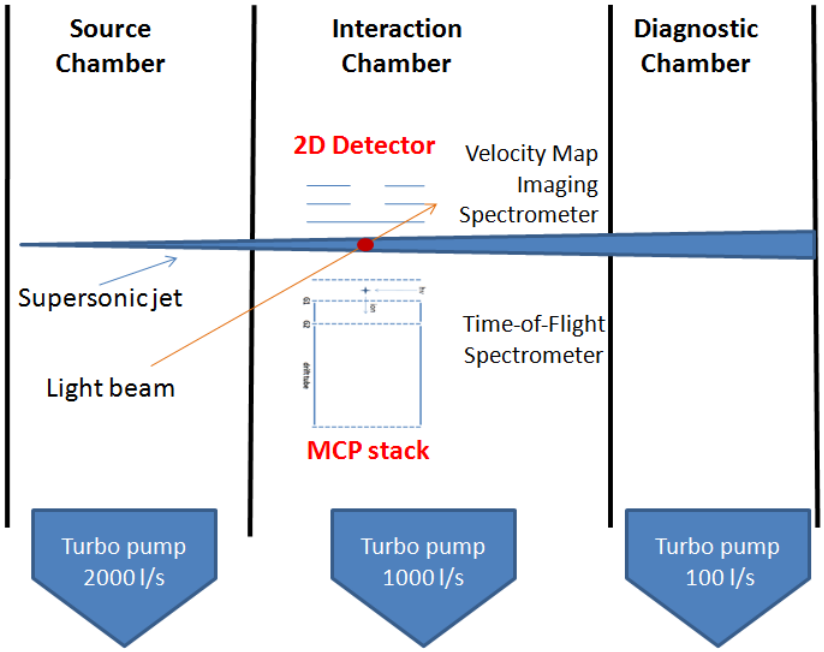

Figure 4.1: *General scheme of the experimental setup.*

for this reason a small section will be also dedicated to new photon beam diagnostics based on diamond devices (section 4.3).

4.1 The VMI experimental chamber at the GasPhase beamline

The GasPhase Photoemission (GaPh) beamline was built at Elettra 18 years ago for photoemission studies of atomic and molecular gaseous targets [35]. The beamline is provided with an undulator of 12.5 cm period, which delivers light in the range from 13.5 eV to well above 900 eV. The monochromator is a Variable Angle Spherical Grating Monochromator, with fixed positions of the slits. The optical design was developed by Sincrotrone Trieste, and includes a toroidal prefocusing and two refocusing mirrors (spherical and plane-elliptical); the layout is shown in Fig. 4.2.

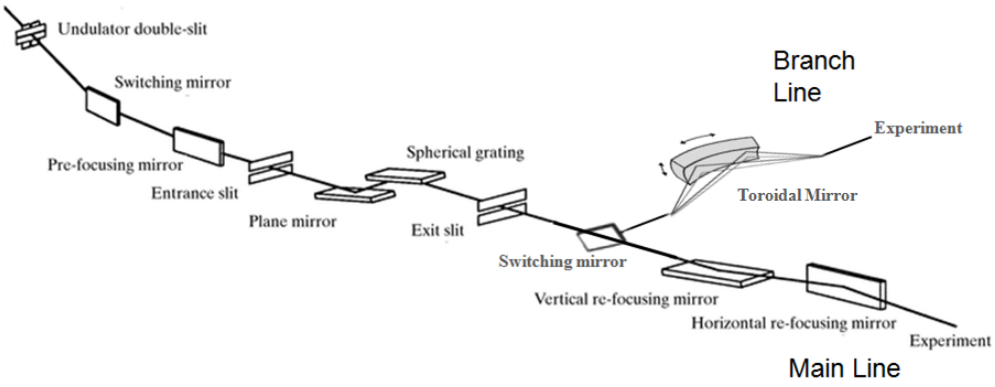

Figure 4.2: *Schematic diagram of the optical layout of the gas-phase beamline.*

The monochromator was commissioned and not only met its specifications ($E/\Delta E \geqslant 10000$) over most of the working range (13-900 eV) but even exceeded them considerably. A resolving power of 60000 was measured at 48 eV. It remains higher than 10000 at 540 eV and a value of 8000 is obtained at 860 eV. This resolving power is the highest among the soft x-ray monochromators at ELETTRA. The use of two refocusing mirrors provides a roughly circular spot at the sample (diameter 350 μm for a 20 μm exit slit and low photon energy, decreasing to less than 150 μm as the photon energy increases above 200 eV). The beamline is connected to the experimental station through a differential pumping section (5 orders of magnitude difference in pressure), to decouple the UHV section of the mirror chambers from the high vacuum in the experimental region. Alternatively after the exit slit it is possible to insert a plane mirror and to deflect the monochromatized radiation to a Branch-Line. A toroidal mirror is placed before the branch-line differential pumping section and it is used to focus SR to a spot of about 350 μm at the interaction point. Both the plane deflection mirror and the toroidal mirror operate at 6° grazing incidence, thus the branch-line has a transmission cut-off at about 200 eV photon energy. The low-energy Branch-Line is equipped with a tunable Ti:Sapphire oscillator (Tsunami, SpectraPhysics) for pump and probe experiments. The main laser specifications are: a tuning range 700-1000 nm (manually tuned), an average power of 0.6-1.2 W at the entrance of the experimental chamber (depending on the wavelength), repetition rate of 83 MHz (1/6th of the storage ring frequency), a pulse length of about 15 ps or 50 fs and variable polarization. When mode-locked, the laser can be synchronized with the storage ring time structure, allowing ps time-resolved measurements also in multi-bunch operation of Elettra.
Recently the optics of the monochromator were heavily contaminated with a carbon deposit, considerably reducing the reflectivity at photon energies close to the carbon K-edge. For this reason an in-situ cleaning of the monochromator optics was carried out by UV irradiation with intense Hg lamp in air, after which the ultra-high-vacuum environment was restored. The production of ozone and highly reactive oxygen species is capable of removing carbon contamination from the optics.
The GaPh beamline offers users a wide number of different experimental chambers[1] as well as the possibility of mounting user's own equipment. In the next section the experimental chamber devoted to photoionization studies of atoms, molecules and clusters will be described in more details. This system has been upgraded, during this thesis work, with respect to a prototype setup described in [36]. The major changes concern the detectors and readout electronics with the aim of extending the maximum detectable kinetc energy up to 45 eV: 1) a wider PSD detector has been mounted; 2) a new readout electronics allows data acquisition in multihit mode; 3) the TOF drift tube has been reduced to 40 mm in order to allow operating in a different swapped detection mode (not presented in this thesis) so that ions are collected with the VMI spectrometer and the electrons by the TOF section. A general setup scheme is shown in Fig. 4.1.

The beam of atomic, molecular and cluster targets (represented by the blue cone in Fig. 4.1) is produced in the first stage: The Source Chamber (see section 4.1.1). Then the source beam interacts with the light beam in the Interaction Chamber (section 4.2.1) where the detection system (VMI and TOF) is placed.

[1] http://www.elettra.trieste.it/lightsources/elettra/elettra-beamlines/gas-phase/bl-description/page-4.html?showall=

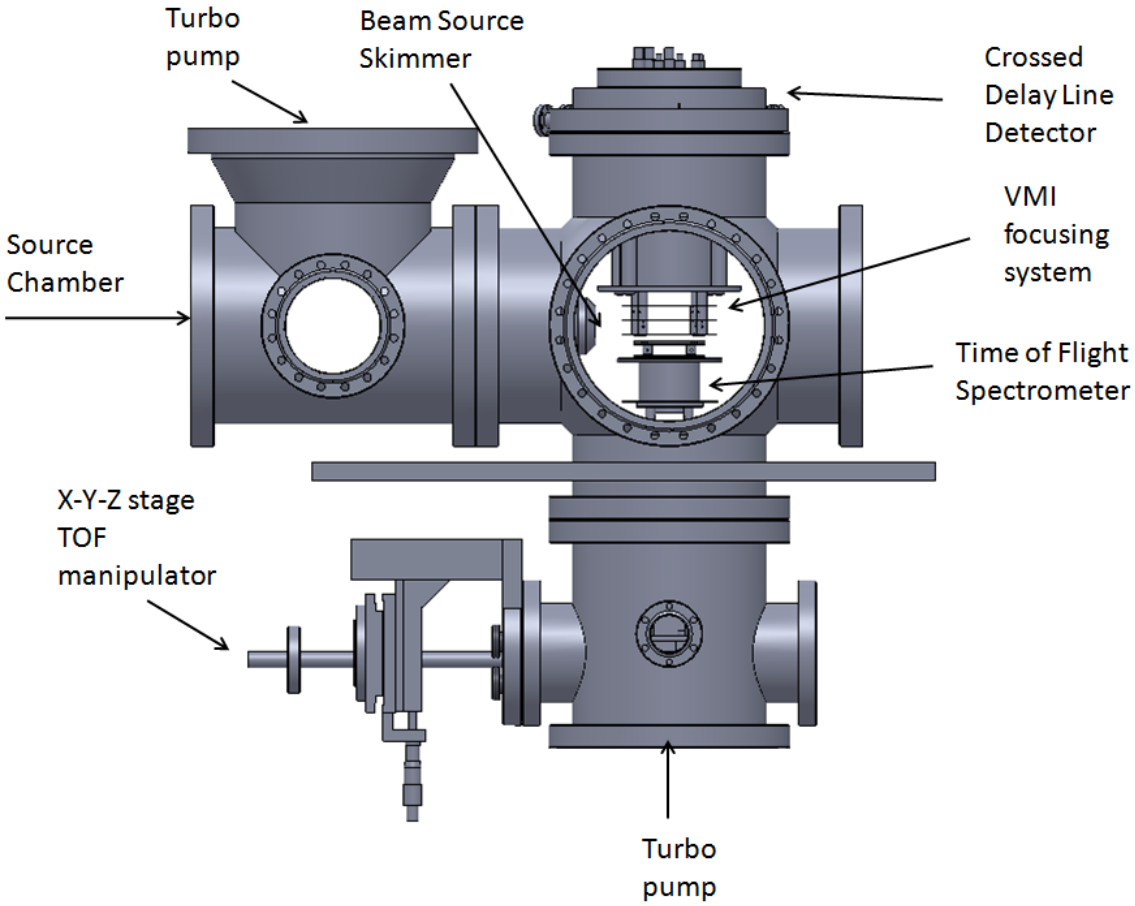

Figure 4.3: *Drawing of the Gasphase VMI experimental setup.*

A more detailed description of this chamber is given in the next sections. Finally a Diagnostic Chamber can host different diagnostics (QMS, LT-detector, etc ...) for a characterization of the gaseous beam source, and a beam dump system in order to avoid spourious effects due to the gas back being scattered towards the interaction and detector regions.

4.1.1 The Source Chamber

The Source Chamber is a CF200-flanged vacuum chamber of 300 mm length, with two CF-100 flanged ports: one is usually used for mounting a Dewar for liquid Nitrogen cooling (down to 78 K) of the gas nozzle that will described later, the other one is used for a full range pressure gauge. On the top of the chamber, a CF-250 port hosts a magnetically levitated, water-cooled turbomolecular pump (Adixen ATP 2300 M, pumping speed 2050 liter/s) [37]. Inside this chamber, just before the interaction chamber, there is a beam skimmer holder (see Fig. 4.3), where skimmers of different diameter can be mounted in order to select the central portion of the supersonic beam.
Two different type of gas sources can be used for the supersonic jet: a continuous source and a pulsed source.

The **continuous supersonic beam source** is essentially obtained by expanding 1-2 bar of gas through a nozzle of 50 μm diameter. The nozzle is mounted on a manipulator that allows alignment of the gas jet with respect to the skimmer. The nozzle-interaction point distance can also be varied by using the manipulator in the range 100-200 mm (typically 120 mm is used). The nozzle can be liquid Nitrogen cooled in order to foster cluster formation. In order to control the temperature and avoid obstruction of the nozzle by ice formation, a kapton heater foil [38] has been mounted all around the nozzle. This beam source system has been used for the results presented later in sections 5.1.1 and 5.1.3.
For the results presented later in section 5.1.2, a mobile source of He droplets [39] (collaboration with University of Freiburg) was used, in which a beam of He nanodroplets is produced by continuously expanding pressurized He (50 bar) of high purity (grade 6.0) out of a cold nozzle (T_0 = 13$\div$33 K) with a diameter of 5 μm into vacuum. Under these expansion conditions, the mean droplet sizes can be inferred to range between 200 and 17000 He atoms per droplet [40].

The **pulsed supersonic beam source** is used when it is important to reach higher densities of gas in the supersonic expansion, but the average gas load must be kept low. It is well suited for cluster production and for operation with pulsed light sources. In fact it is mostly adopted at FERMI (see section 5.2.2). The gas jet of the LDM endstation is built around an Even-Lavie pulsed valve [41]. This particular pulsed valve is connected to a closed-cycle cryostat and optimized for producing helium droplets. It can operate up to 500 Hz with an almost constant intensity and with opening times of about 20 μs. The great advantage of using such a pulsed valve is that the droplet density increases by more than an order of magnitude as compared to a continuous-flow droplet source [41], while maintaining the same gas load. In this particular case the supersonic beam of He clusters has been obtained by expanding He gas at 50 bar stagnation pressure through a conical nozzle (100 μm diameter, with half-opening angle of 45°) and cooled to 17 K.

4.1.2 The Interaction Chamber

The Interaction Chamber is also called the *Detector Chamber*. It is here that the source beam coming from the source chamber interacts with the light beam and the particles produced by the photionization are detected. The general scheme, reported in Fig. 4.4, consists of a Time-Of Flight Mass Spectrometer and a Velocity Map Imaging focusing system coupled to a 2D Position Sensitive Detector (PSD). Since the detector chamber has been the main subject of the PhD project, in the next subsections I will enter into greater detail.

As seen in Fig. 4.4, a) the cooled supersonic jet of gaseous targets produced by using the systems described in the previous section, interacts with the SR light beam. In normal operation mode, the electrons and ions produced by photoionization go respectively upward and downward in the scheme. Fig. 4.4 b) shows an horizontal section of the interaction chamber drawing, on the top side is the Velocity Map Imaging focusing system and the PSD detector on the bottom side the Time-of- Flight spectrometer.

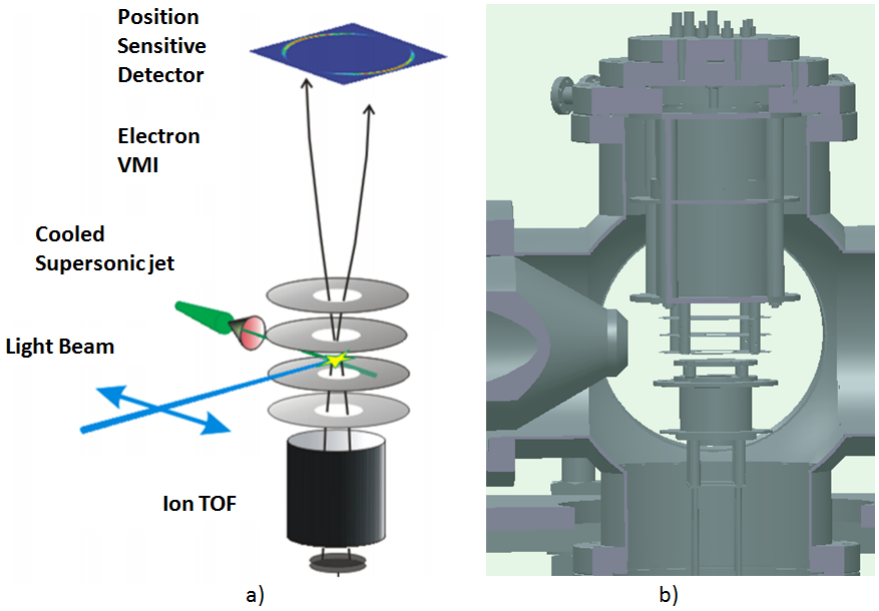

Figure 4.4: *a) General Scheme of the Interaction Chamber. b) Horizontal section and zoom of the interaction chamber drawing.*

The Velocity Map Imaging Spectrometer

The working principle of VMI spectrometers has been described in chapter 3. In the drawing of Fig.4.5 we can see the Extractor and Repeller Electrodes plus an additional electrode (labelled as 3^{rd} Electrode). The Electrodes are metallic plates of 100 mm diameter, 0.2 mm thick. The Repeller has a hole in the center of 40 mm diameter, while the Extractor and the 3^{rd} Electrode have holes of 20 mm.

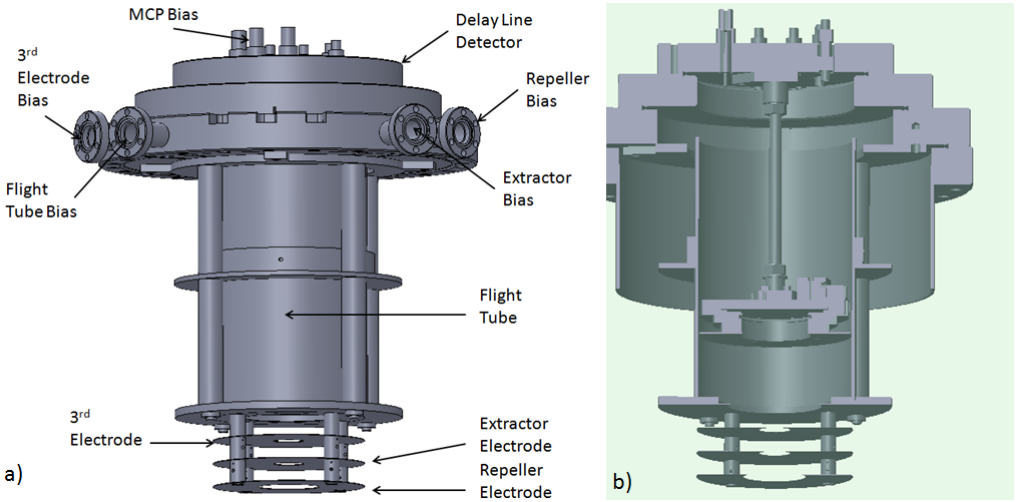

Figure 4.5: *a) Drawing of the VMI Spectrometer. b) Transverse section.*

The gap between these electrodes is 15 mm, and they are kept separated and electrically isolated by small cylinders made of PEEK. The Time-Of-Flight tube is 170 mm long. All the structure is mounted on the CF200 side of a CF200-CF150 adapter which

also hosts four feedthroughs for the High Voltages (HV) of all the electrodes and the flight tube bias. Also a 2 mm thick μ-metal shield is present in order to prevent magnetic fields from affecting the particle trajectories. Also a CF150-CF100 zero length adapter (visible in figure 4.5) is required for the PSD assembly which is mounted on a CF100 flange. The transverse section in Fig. 4.5 b) provides a close view inside the flight tube, where the PSD is mounted.

The 2D Position Sensitive Detector: The Crossed Delay Line

The bidimensional Position Sensitive Detector (PSD) for SR experiments has been constructed at the Instrumentation and Detector Laboratory of Elettra-Sincrotrone Trieste S.C.p.A [42]. A drawing of the PSD mounting is reported in Fig. 4.6: The PSD is

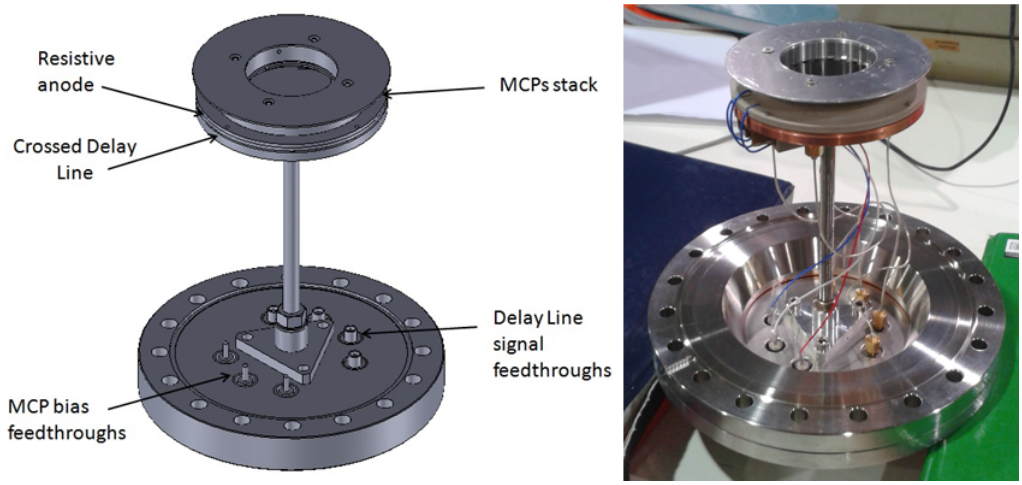

Figure 4.6: *On the Left: Drawing of the Position Sensitive Detector for SR applications. Right: Photo of the Detector.*

mounted on a CF100 flange. At the base of the flange, a triangular support and threaded rod of 135 mm hold the mounting of the MCP, the resistive anode and the crossed delay line assembly. A SIMION simulation indicates that the optimum distance between the MCP stack and the interaction point is 100 mm. This value was found by considering an MCP effective area of 42 mm and the possibility, using a power supply of 3 kV maximum, to image electrons up to 45 eV. The MCP-interaction point distance can be adjusted via the threaded rod.

A scheme of the position sensitive part of the PSD is reported in Fig. 4.7 b) which is composed of: a Crossed Delay Line Detector, a resistive anode and an MCP stack (Hamamatsu F4296-10). The MCP stack consists of a pair of MCPs, resistance matched in Chevron configuration, with 46 mm diameter and active area of 42 mm [43]. The resistive anode is a plate with a resistance of about 1MΩ/sq it is placed in between the MCP stack and the crossed delay line.

The crossed delay line (see Fig. 4.7 d)) is fabricated with Thick Film Technology (TFT) and consists of an upper serpentine line embedded in an insulating substrate, then a ground line parallel to the delay line, the lower serpentine line, and again a ground line parallel to the delay line as seen in Fig. 4.7 c).

The resistive anode placed in between the MCP stack and the crossed delay line al-

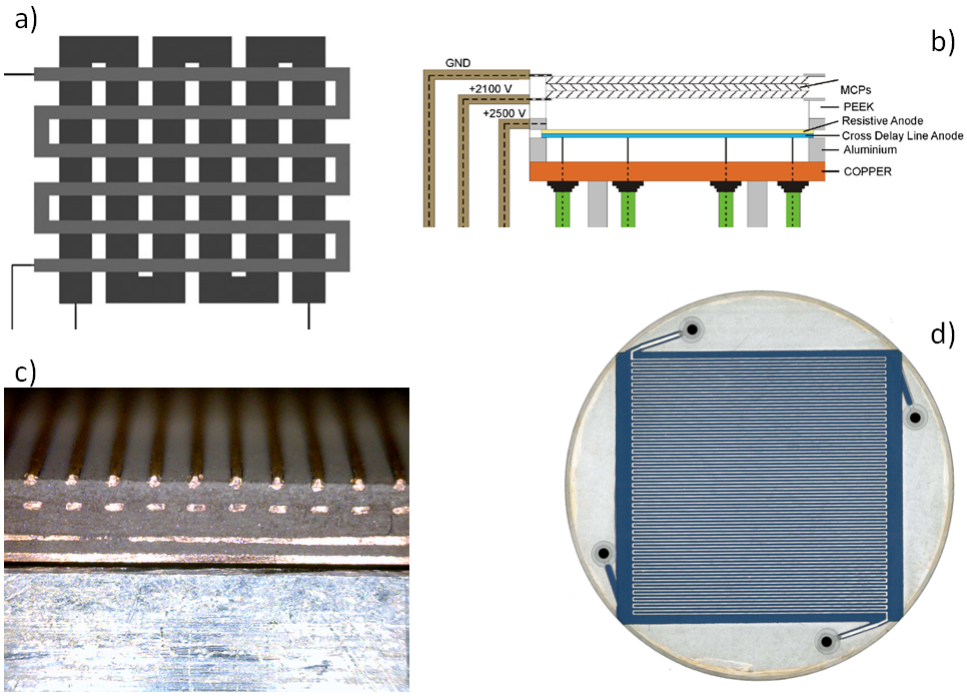

Figure 4.7: *in b) scheme of the position sensitive part of the PSD (figure from the original paper [42]). a) Scheme of the crossed delay line. c) Crossed delay line zoom. d) Crossed delay line 46x46 mm for SR applications.*

lows decoupling of the HV of the MCP stack from the delay line and also capacitive de-coupling of the signal. In this way positive as well as negative ions/electrons are detectable, while keeping the crossed delay anodes at low voltage.
The crossed delay line is a square of 50 mm side characterized by a propagation time of 33 ns for the upper serpentine line and 36 ns for the lower serpentine line. The distance between MCP stack and resistive anode-delay line assembly is about 5 mm, and this distance is optimized so that between 3 and 5 meanders of the delay line are involved in each event, in order to get a better estimation of the centroid of the electron cloud [42].

The Time-Of-Flight Spectrometer

The Time-Of-Flight Spectrometer (TOF), whose working principle has been described in chapter 3, is used for mass-charge ratio discrimination. The TOF drawing is reported in Fig. 4.8: It consists of two meshes, held by two annular supports (see top of Fig.4.8) and kept at the appropriate potentials according to the Wiley-McLaren conditions discussed in chapter 3. A central aluminum drift-tube has been used, whose dimensions can be changed depending on the target under analysis and the resolving power required (for the results shown in the next chapter, a 40 mm drift-tube was used). At the bottom there is a 30 mm diameter Micro Channel Plate (MCP) stack manufactured by tectra GmbH [44], and used also as trigger and for signal amplification. In front of the exit side of the MCP stack (effective area 26 mm) a home-made resistive anode is placed to collect the ion signal. A typical spectrum obtained with such a detector is reported in Fig. 4.9 as an example. The whole TOF mounting is supported by 4 rods mounted on an

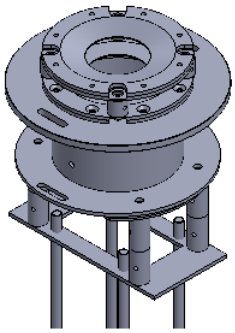

Figure 4.8: *The Time-Of-Flight Spectrometer.*

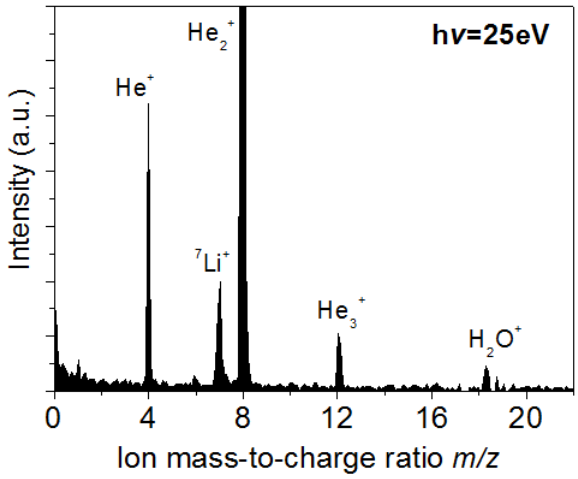

Figure 4.9: *Example of a typical TOF Spectrum [45].*

XYZ movable stage (see Fig. 4.3) allowing the TOF detector to be moved along the supersonic jet source direction. This feature is particularly relevant since heavier clusters ions travel a longer distance along the jet source propagation direction before hitting the MCP stack. This aspect has been simulated by using SIMION before proceeding with the construction of the detector, according to the experimental requirements.

4.1.3 Power Supply, Readout Electronics and Data Acquisition

For the most frequently used configuration in normal Photo-Electron-Photoion-COincidence PEPICO measurements the Voltage Supply settings and Power Supply (PS) chain is reported in Fig. 4.10. In order to avoid large voltage differences that may cause damage to the detector, a floating voltage supply system has been adopted, and this is particularly important when dealing with high voltages.
A new prototype of floating PS system, called FLEX (FLoating EXtended system) made by Elettra Sincrotrone Trieste S.C.p.A, was used. This system can be custom mounted with different precision regulated, low ripple, HV modules, namely EMCO CA series [46] ranging from 200 up to 2000 V.

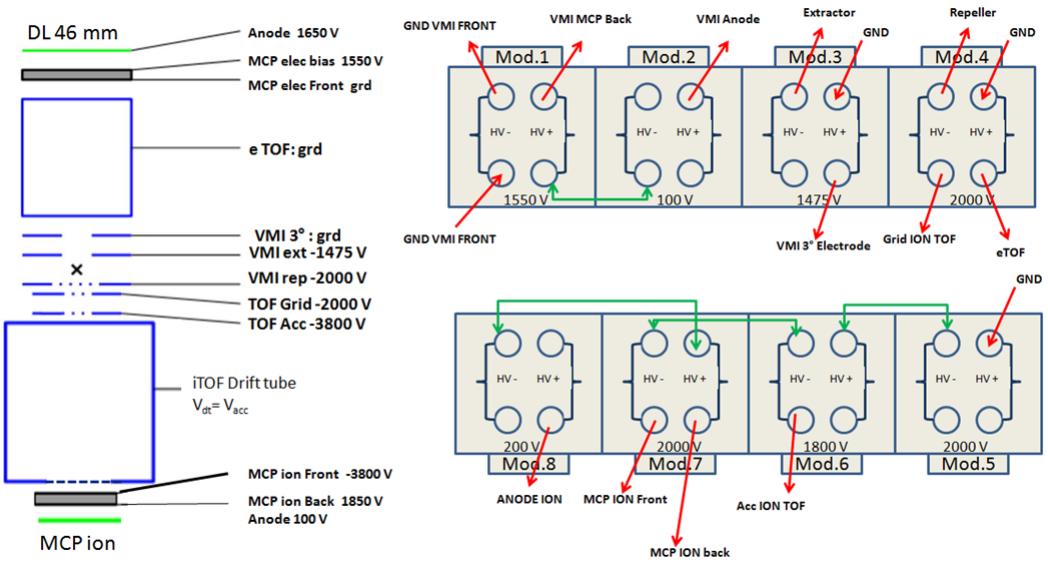

Figure 4.10: *Schematic illustration of the voltage settings and relative floating power supply chain.*

Voltage stability is particularly crucial when high resolution is required, and these modules have a voltage stability of < 25 ppm/^{0}C [46].
A schematic illustration of the readout scheme is reported in Fig.4.11. When an elec-

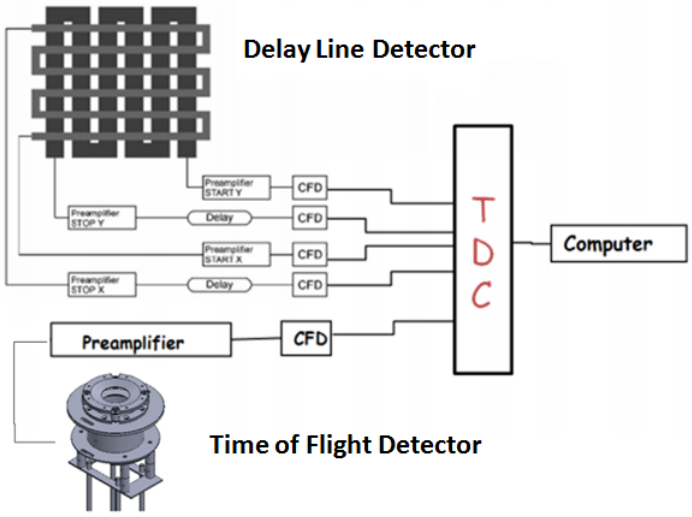

Figure 4.11: *Schematic illustration of the readout scheme.*

tron arrives at the MCP front an electron cascade takes place. The subsequent localized shower of electrons is collected onto the resistive anode, inducing a capacitive signal in a specific X, Y position on the delay lines. The four signals, taken from each end of the delay lines, are amplified immediately at the air-side of the detector and sent to an advanced four-channel time converter (THR02-ST) [47] made by Elettra-Sincrotrone Trieste S.C.p.A. specifically built for 1D or 2D delay line detectors. Inside the THR02-ST, every channel is coupled to a Constant Fraction Discriminator (CFD) that allows the extraction of the incoming pulse centroid with very low jitter, thus producing a

digital signal no longer influenced by the amplitude variations of the pulses, but fully preserving the time information related to incoming particles. Then the digital signal is fed into the time-to-digital converter (TDC) that calculates the arrival time of stop hits with respect to a digital trigger signal, the start signal. Acquisition starts when the start signal is registered and it terminates after a predetermined amount of time, the so called time window. All stop hits that happen to be detected by the acquisition system during the time window of the TDC are saved: this feature, called the multi-hit capability, is mainly constrained by some specific TDC limitations and by detector propagation time. As a start pulse the user can select whether to use an internal or external trigger source [47]. This system allows a real-time visualization of the position of the photo-electron arriving at the detector by means of a specific code developed within under the LABVIEW National Instrument environment [48]). The THR02-ST is equipped with 4 direct output after CFDs. These 4 signals are fed into another external TDC board (ACAM TDC-GPX 8 channels) together with the amplified and discriminated signal from the TOF detector. All events are recorded on a computer where, after acquisition, electron images and ion Time-Of-Flight spectra are reconstructed in coincidence via software.

4.2 The Low Density Matter endstation at FERMI

Low Density Matter (LDM) is one of the three beamlines currently present at the Free Electron Laser (FEL) facility FERMI at Elettra. LDM is designed to investigate atoms, molecules, and their aggregates (clusters) in an unperturbed environment (a supersonic jet in vacuum). The LDM end-station is based on a modular design which includes interchangeable sources for high- and low-temperature jets, helium nanodroplets, rare-gas and water clusters, metal clusters, and radical species [49].
The LDM beamline operates within the full photon energy range of FEL1 and FEL2, from 12 eV to 300 eV. Photons are delivered to the experimental stations by means of the *photon analysis, delivery and reduction system* (PADReS) [50]. The photon transport, including a delay line ($\pm$30ps), is shared with all other beamlines up to the three-way switching mirror, see Fig. 4.12. After that, the FEL beam is refocussed into

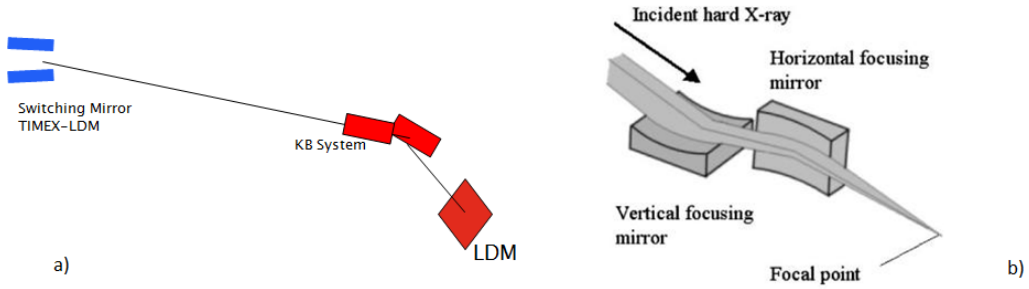

Figure 4.12: *a) Schematic diagram of the optical layout of the LDM beamline; b) detail of the KB mirror system.*

the end-station by a Kirkpatrick-Baez mirror system (see fig. 4.12 b). The latter comprises two bendable (active) mirrors capable of a minimum spot size of about 10 μm, at a focal length of 1200 mm from the center of the second mirror. Photon polarization

at the source can be chosen arbitrarily, subject to the constraint that the axes of the polarization ellipse lie in the horizontal and vertical planes. All transport optics preserve linear polarization, thus arbitrary linear polarization is available at the target. Some degradation of circular (elliptical) polarization is unfortunately occurring, particularly at longer wavelength, which can be evaluated by means of optical calculation [51]. For those experiment requiring a particularly high degree of circular polarization, a proper tuning of the FERMI undulators should be used to compensate this beam-line dichroism. A synchronized Infrared (IR) femtosecond laser (2) pulse can be introduced (almost) collinearly to the FEL thanks to the recombination mirror (3) for pump-probe experiments. As in the case of SR experiments, the main methods currently in use are electron and ion spectroscopies, using a velocity map imaging (VMI) detector, and Time-Of-Flight (TOF) mass spectrometer respectively. The main source (4) for most experiments is a pulsed valve which can be cryogenically cooled and provides intense atomic, molecular and cluster beams [49] (Numers in brackets refers to figure 4.13).

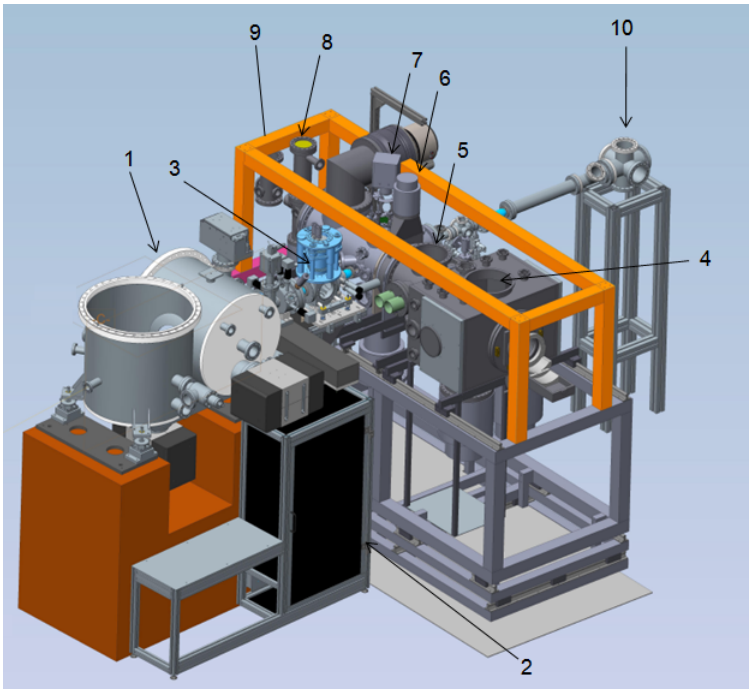

Figure 4.13: *Overview with 3D rendition. (1) Kirkpatrick-Baez mirror chamber. (2) User Seed Laser. (3) Recombination Mirror. (4) Source chamber. (5) Doping chamber. (6) Differential pumping chamber. (7) Detector chamber. (8) Quadrupole mass spectrometer chamber. (9) Surface ionization detector chamber.(10) FEL beam dump.*

The FEL light passes into the main chamber through the target region, and exits to a beam dump at the back. The light is focused at the target region, and as mentioned above, the focus size is adjustable via the adaptive optics (1) of the PADReS system. The chamber is furnished with a retractable fluorescent screen (yttrium aluminium perovskite crystal) for optimizing the focus. The light spot is viewed by a CCD camera, rigidly attached to the screen's manipulator, and this is the primary diagnostic for achieving the best focus of the light. The beam dump (10) consists of a 1.6 m long tube with a retractable, gold-coated, polished copper plate at the end, which reflects the

light down into a second tube. For beam alignment and diagnostic purposes, the plate can be retracted to allow viewing of the beam on a fluorescent screen on the inside of the rear window of the beam dump [49]. For a first feasibility test of the detection system, the interaction chamber described in the section describing the SR setup has been used. So the VMI focusing system was exactly the same, and the major change was in the PSD. Because of the higher rate of events produced by such a brilliant light source with respect to SR, the crossed delay line detector was no longer used as PSD, since a discrimination of the events and their position reconstruction would be impossible. In the case of the FEL application, a different PSD solution has been adopted: an MCP stack, a phosphor screen and a camera (see figure 4.14).

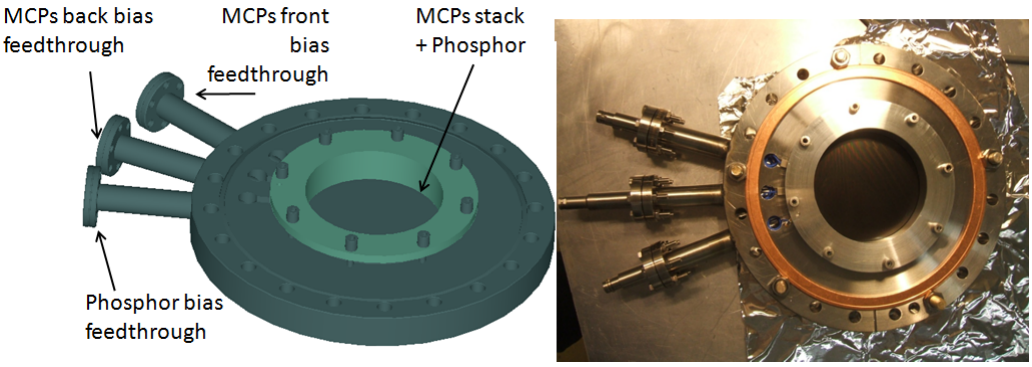

Figure 4.14: *Drawing a) and Picture b) of the Position Sensitive Detector for FEL applications made by the Instrumentation and Detector Labs. of Elettra-Sincrotrone Trieste S.C.p.A.*

During the beamline construction period commissioning measurements of the beamline optics were performed at LDM with the GasPhase VMI end-station equipped with the in-house built imaging plate made in collaboration with the Instrumentation and Detector Labs. of Elettra. The phosphor used is a P47 type, (Y_2SiO_5:Ce) with a maximum light emission at 400 nm and a very short luminescence decay time of 100 ns. The phosphor powder has been mixed to a UHV compatible glue and deposited by using spin coating techniques. Over the phosphor an aluminum layer coating has been also deposited for the HV supply of the phosphor (from 4 kV up to 10 kV). Then an MCP stack of 77 mm diameter has been used.
With this setup we measured multiphoton ionization from rare gases using the VMI setup in both PES and ion collection mode [52]. As an example a TOF spectra of Xe^+, Xe^{2+} and Xe^{3+} is shown in Fig. 4.15. Each spectrum is a sum over 10 shots, normalized by FEL intensity. The multiplet structure of each charge state reflects the natural abundance of the Xe isotopes. This measurement is clear evidence of multiphoton absorption, i.e. good focussing. To produce Xe^{3+} ion at 52.22 nm one need direct absorption of three photons or a two photon sequential double ionization plus two further photons to ionize Xe^{2+} [53].

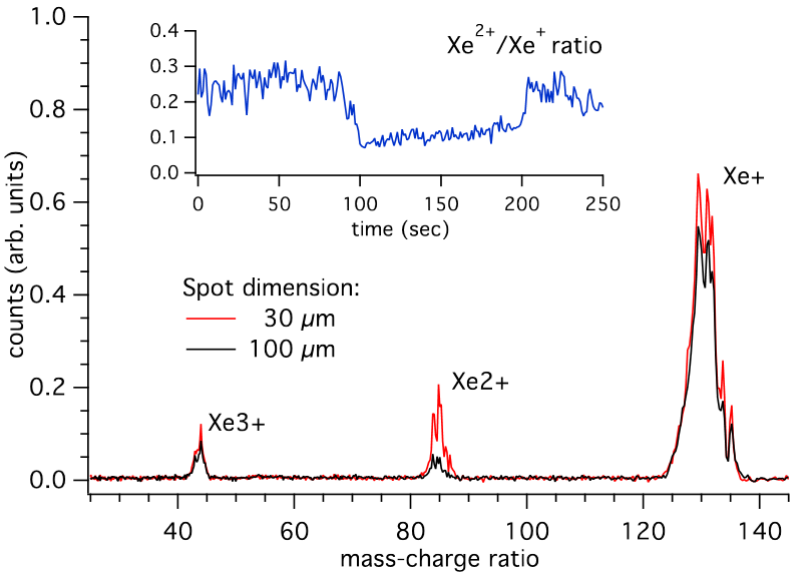

Figure 4.15: *Ion TOF mass spectra of Xe taken at λ = 52.22 nm (23.74 eV) for different focusing conditions (picture taken from the original paper [52]). In the inset (blue line) we show the Xe^{2+}/Xe^{+} intensity ratio recorded while changing the curvature of the KB mirrors.*

4.2.1 The Interaction Chamber

In parallel to the successful commissioning of the beamline dedicated to the testing of the above system, it has been the construction of the final interaction chamber and endstation (with the use of a commercial PSD) for LDM, work of a wide collaboration involving several institutions, coordinated by Prof. F. Stienkemeier (Molecular and Nanophysics Group, University of Freiburg, Germany). For a complete description of the endstation please refer to [49]. In Fig.4.16 a cut view is shown of the present interaction chamber ((7) in Fig. 4.13).

As seen in the drawing, the VMI spectrometer consists of electrodes shaped as truncated cones, a flight tube and a detection system based on a commercial imaging plate PSD from Photonis. The imaging plate consists of an MCP stack of 75 mm diameter, a phosphor screen and a sCMOS Andor Neo camera, with 2560 x 2160 pixels, of size 6.5 microns [54].

Conical electrodes, instead of flat ones, have been adopted, in oder to minimize interference with an additional detector for photon scattering which can be mounted along the FEL propagation axis. In Fig. 4.16 it is also possible to see the mounting of the TOF spectrometer.

The TOF spectrometer is located opposite to the VMI spectrometer and the first accelerating region is defined by the VMI geometry. It may be operated at the same time as the VMI to obtain ion and electron spectra simultaneously, but the resolution of the TOF depends on whether it operates independently or simultaneously with the VMI [49].

The LDM endstation data acquisition system, developed by the FERMI control group, in collaboration with the LDM staff, is integrated into the TANGO [55] control system of the FERMI facility.

The acquisition hardware, includes a CAEN digitizer, model VX1751, 100 μs of acquisition per shot, and the Andor camera for the VMI spectrometer. Several trigger signals

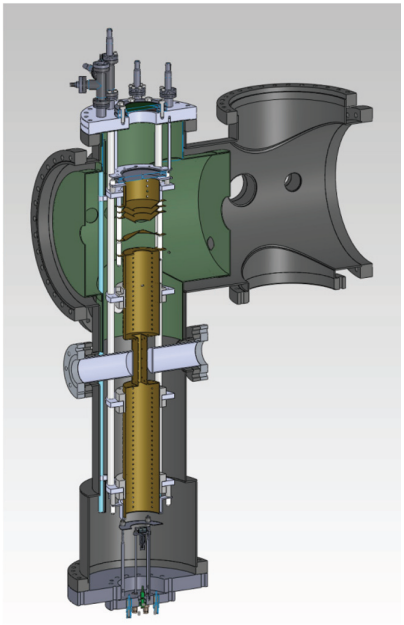

Figure 4.16: *Cut-view of the interaction chamber, showing the VMI and the TOF mass spectrometer. Picture taken form the original paper [49].*

are necessary, for example to open the gas source valve or the shutter of the camera, to provide time zero for the TOF mass spectrometer [49].
In contrast with the detection system for SR application described previously, with such a detection system it is not possible to perform coincidence spectroscopy.

4.3 Diamond detectors for beam diagnostics

Because of its physical and electronic properties (see section 3.3) diamond is the most promising material for the production of semitransparent in situ pBPMs, and it might be the only suited material to be utilized as pBPM for X-ray free electron lasers [32,33]. The working principle of diamond detectors is described in section 3.3. In this section the experimental apparatus developed in collaboration with the Detector and Instrumentation Laboratory of Elettra and the XUV_Lab of the University of Firenze is presented. The general experimental scheme for SR applications is reported in 4.17.

The temporal structure of the Elettra synchrotron radiation light in *hybrid-mode* operation consists of 432 buckets with 2 ns spacing. Not all the buckets are filled, usually about 40 buckets are left empty resulting in a dark gap between a train of pulses of about 80 ns. An additional single high current (4 mA) bunch can be placed in the middle of this dark gap. After leaving the synchrotron ring the radiation passes into the beamline monochromator for wavelength selection and then the light impinges on the diamond detector housed in a vacuum chamber (Fig. 4.18). The read out electronics consists of a low frequency or a high frequency system, the data are stored in a computer which is also used to control the detector.

The device is housed in a compact (about 20 cm) evacuated chamber provided with two X-Y translator stages allowing movement with sub-micrometric precision.

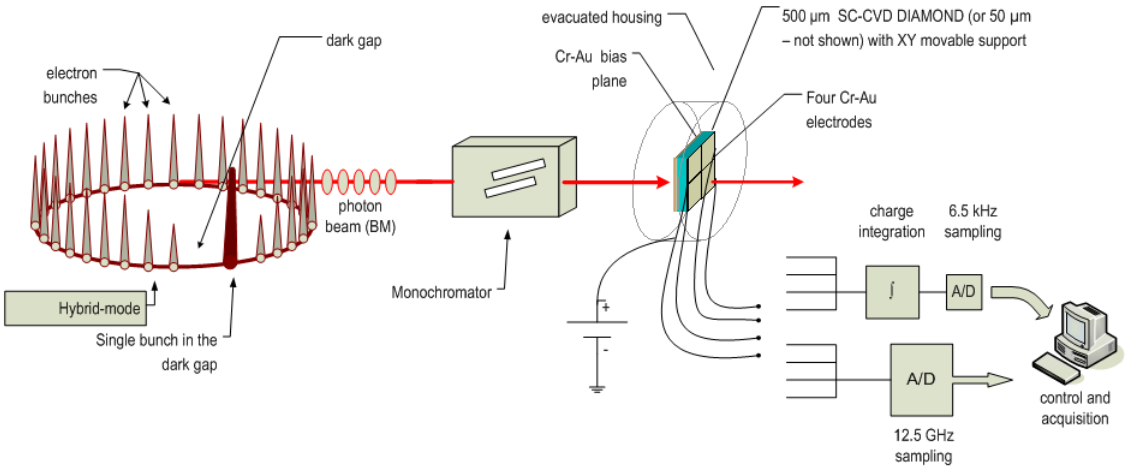

Figure 4.17: *General experimental scheme for SR diamond photon beam monitors.*

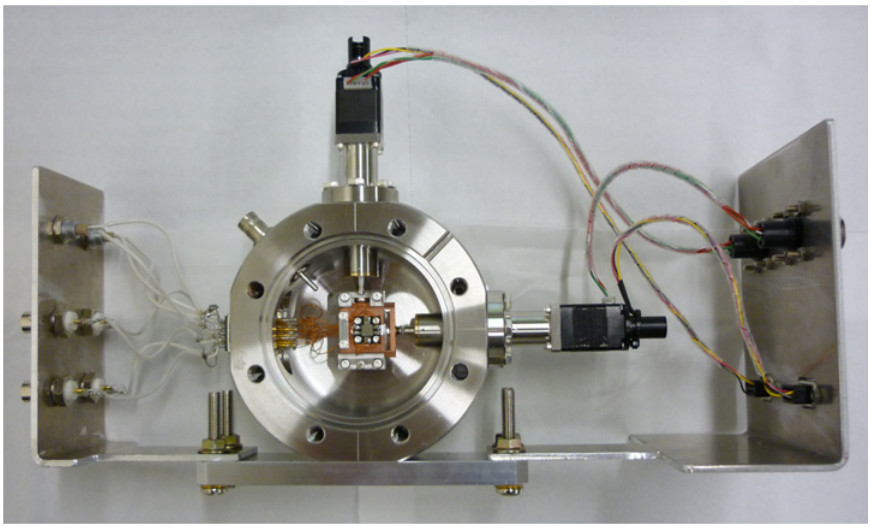

Figure 4.18: *Picture of the compact evacuated chamber housing the diamond detector.*

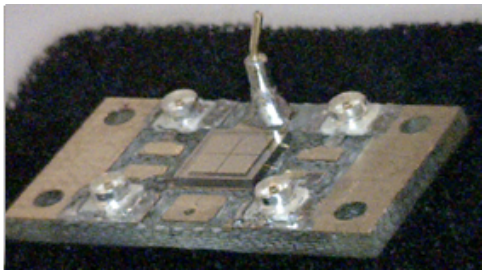

Figure 4.19: *Image of the sCVD diamond detector with a 4-quadrant configuration.*

The stepper motor actuators are computer driven using software developed in Labview, allowing correlation of the readout signal with the position of the detector. In

figure 4.18 signal cables and a bias cable are also visible. Several diamond substrates can be used depending on the application and on the photon wavelength. Fig. 4.19 shows the configuration that we have been used most for BPM and temporal structural monitoring. The detector has been fabricated starting from a commercial standard quality freestanding, 500-μm-thick, single-crystal Chemical Vapor Deposited (sCVD) diamond layer with an area of about 5×5 mm^2. The diamond was coated on both sides with Cr-Au contacts deposited by using standard thermal evaporation techniques; the front electrodes have been provided with a cross shaped aperture of 70 μ m (4-quadrant configuration) to let the XUV radiation interact directly with the bulk of the diamond.
The diamond is usually biased with voltages ranging from 15 V to 500 V and the generated photocurrents are read by means of two different acquisition systems working respectively at low and high sampling frequencies. The low frequency case, used for beam position and beam intensity monitoring, consists in a charge integration and analog-to-digital conversion (ADC) system at 6.5 kHz, by using a four-channel AH501B picoammeter, built by Elettra-Sincrotrone Trieste S.C.p.A [56]. The high frequency case, used for temporal structure monitoring of the light, consists of an oscilloscope (Tektronix DPO71254, 12 GHz, 50 GS/s sampling rate).

CHAPTER 5

Results

This chapter reports some relevant results achieved with the experimental setup presented in the previous chapter. The experiments discussed in publications [40, 45, 57] based on SR have been carried out at the GasPhase beamline, while for those concerning FEL experiments based (discussed in publications [58–60]) at the Low Density Matter beamline. Many other investigations at Gas Phase and at LDM have used the experimental apparatuses decribed in the previous chapter. Their analysis is still in progress and they will not be reported here. In any case the experiments presented in this chapter will fully illustrate performance and capability of the detection systems realized during my thesis work.

5.1 Experiments at Elettra

The results presented in this section have been obtained with the experimental setup described in section 4.1.

5.1.1 Atomic spectra (Ne, Xe)

Photoionization of simple atomic targets is usually one of the most frequently used tools to characterize detector response.
First of all a characterization of the TOF mass spectrometer (presented in the previous chapter) was performed in order to determine the calibration and resolving power of the system. In this case ionization of atomic krypton with photon energy $h\nu$=36 eV has been used. Krypton is an ideal target because it has many isotopes (^{78}Kr 0.3%, ^{80}Kr 2.3%, ^{82}Kr 11.6%, ^{83}Kr 11.5%, ^{84}Kr 57.0%, ^{86}Kr 17.3%, [61]). In the TOF spectrum shown in Fig. 5.1 we can clearly distinguish the following ionic species: singly ionized

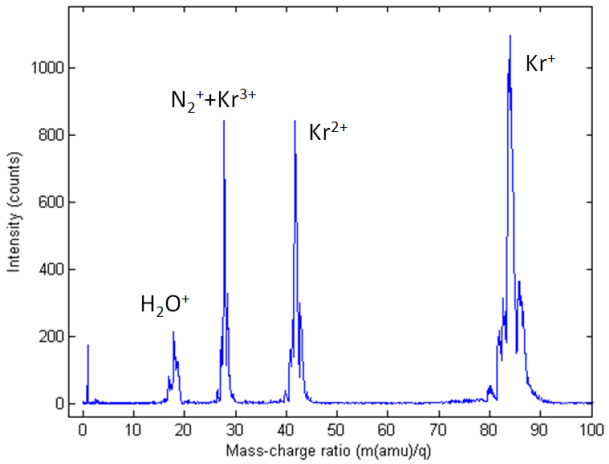

Figure 5.1: *TOF spectrometer mass calibrated ionizing atomic krypton targets.*

Kr (Kr^+), doubly ionized Kr (Kr^{2+}), triply ionized Kr (Kr^{3+}) superimposed on molecular nitrogen (N_2^+) and water (H_2O^+) from ionization of the residual gas. The ionization potentials of Kr are $IP_1 = 14.0$ eV, $IP_2 = 24.3$ eV and $IP_3 = 35.7$ eV [6]. A full width half maximum of 1.2 amu for the main Kr peak at 84 amu ($\Delta m/m$ of 1.4 $\%$) has been found, corresponding to a resolving power $m/\Delta m$ of 70. This measurement has also been used to check the Wiley-McLaren space focusing conditions (discussed in chapter 3), by adjusting the applied voltages, recording spectra and observing changes in the resolution and collection efficiency.
Concerning the VMI spectrometer, in order to obtain a measure of the homogeneity of the response function of the image from the 2D detector and VMI system, photoionization of Ne (IP = 21.56 eV) was used at photon energy of 27.5 eV and reducing the extraction voltages (to $V_{repeller}$= - 200 V and $V_{extractor}$= - 147 V, settings for the collection of electrons with 3.5 eV of maximum kinetic energy) such that the main ring due to the electrons is off the detector. At 27.5 eV Ne 2p has an asymmetry parameter β (see definition in eq. A.1 in section 1.2.1) about 0 and so gives an isotropic angular distribution for detector response calibration. The result of the homogeneity response test is shown in Fig. 5.2.
The homogeneity response of the 46 mm detector, has been found to be around 75$\%$, excluding a small region (white coloured in Fig. 5.2) on one side of the detector. This asymmetric response of the detector is probably due to an uneven tightening of the MCP stack on one side.
An energy calibration has been performed in order to assign the radial position of the electrons on the 2D detector to the corresponding kinetic energy. The energy calibration must be done for each different VMI voltage setting. As an example only the calibration for the most frequently used VMI setting is shown. This calibration has been done again by using atomic gas targets, in particular a neon and argon mixture (12:1) so that at least two rings for each photon energy appear on the image acquired. When selecting the photoelectron, masses correlated with the TOF spectrum reported at the bottom left side of Fig.5.3 were used. The TOF spectrum clearly shows a water peak originating from the background gas of the chamber, the main peaks of singly ionized neon

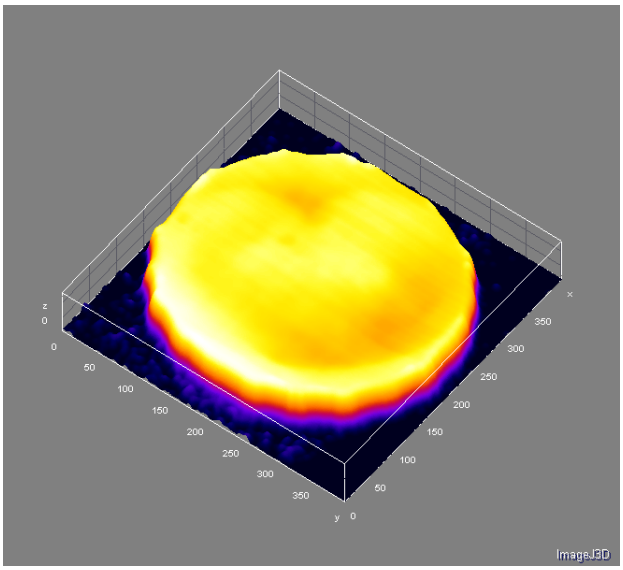

Figure 5.2: *Image illustrating the homogeneity of the detector response function for photoemission from atomic neon at a photon energy of 27.5 eV.*

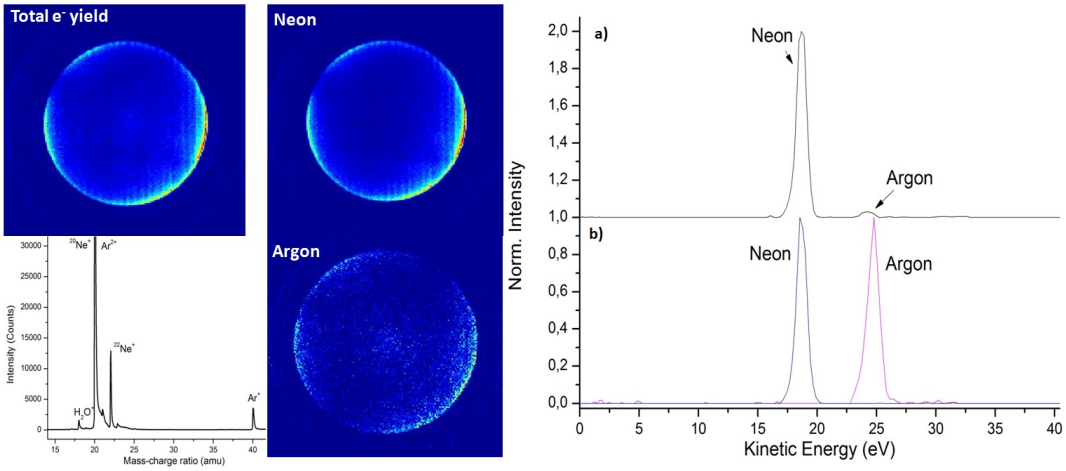

Figure 5.3: *Left: photoelectron images of the neon-argon mixture: total electron yield and mass-correlated with neon and argon ions. Bottom-left: TOF ion mass spectrum. Right: a) PES of the total electron yield, b) PES in coincidence with mass-correlated neon ions (blue) and with argon ions (magenta). Photon energy 40 eV.*

superimposed on doubly-charged argon, the major neon isotope (mass-charge ratio 22 amu) [61] and at 40 amu the signal from singly ionized argon. The ratio between the peaks (30:1) is the one expected at 40 eV photon energy.
Figure 5.3 shows on the top left side the raw photoelectron image of all the electrons collected during the measurement, and also the photoelectrons correlating to a specific mass: neon and argon.
On the right side of Figure 5.3 in a) the PES (after pBasex inverse Abel transformation) is reported obtained from the total electron yield image, the argon peak is barely visible in the image. The plot in a) has been shifted vertically for clarity, In b) the PES coming from the image of the photoelectron mass-correlated respectively with neon

(blue curve) and argon (magenta curve) are reported. The gain in resolution and in the contrast of the signal is clear.
The energy calibration has been done by changing the photon energy from 21.7 to 40 eV, producing electrons with kinetic energies as reported in table 5.1. The neon and argon Ionization Potentials (IP) are 21.56 eV and 15.76 eV respectively [6].

Table 5.1: *Calibration data*

Filename	Photon Energy	Ne (KE)	Ar (KE)
NeAr_058	35 eV	13.5 eV	19.3 eV
NeAr_059	30 eV	8.5 eV	14.3 eV
NeAr_060	25 eV	3.5 eV	9.3 eV
NeAr_061	23 eV	1.5 eV	7.3 eV
NeAr_062	21.7 eV	0.2 eV	6 eV
NeAr_063	40 eV	18.5 eV	24.3 eV

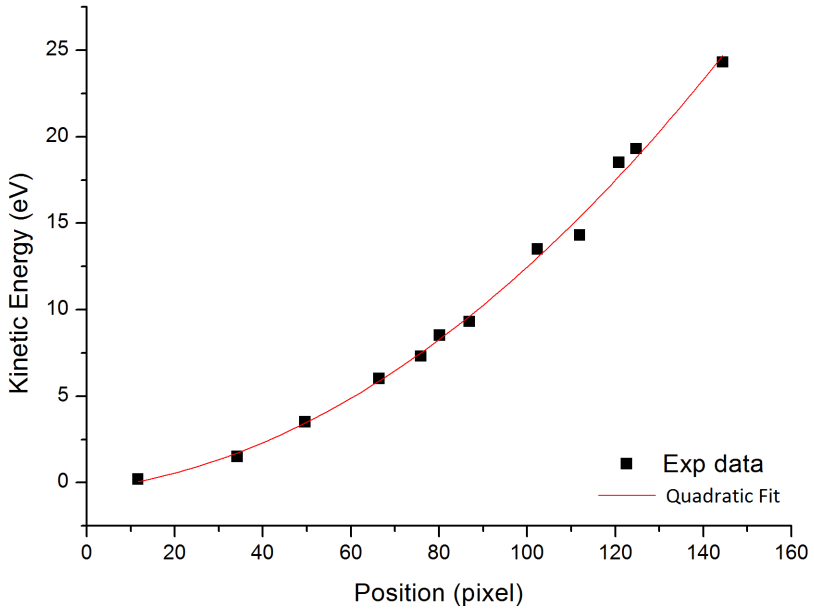

Figure 5.4: *Energy calibration on neon and argon mixture (see table 5.1).*

The energy calibration reported in Fig. 5.4 has been obtained for the most frequently used voltage settings (35 eV maximum electron kinetic energy):
$V_{extractor} = -1472V$ and $V_{repeller} = -2000V$. The curve can be fitted well with a 2^{nd} order polynomial (as expected, see Sec. 3.4): $KE = A + Bx + Cx^2$, here x represents the radius of the circle on the 2D VMI image. The fitted curve gave the following result for the coefficients: $A = 0, B = 1.72 \times 10^{-2}, C = 1.00 \times 10^{-3}$ with an agreement of 99.8% (Adj. R-square). Once the energy calibration has been accomplished, it is also possible to evaluate the maximum kinetic energy of the electrons collected by the detector with this voltage setting. In our case the limitation is given by the MCP stack

dimension (42 mm effective diameter [43]) resulting in a maximum kinetic energy of about 34 eV.
The instrument resolution has also been measured for the VMI settings used. As outlined in section 3 the resolution depends on the diameter of the KE ring. The wider the ring the better the resolution. For the VMI voltage settings mostly frequently used (and data analysis method used) and for an electron kinetic energy of 8.5 eV a $\Delta E/E$ full width half maximum of 9 $\%$ has been found, while for an electron kinetic energy of 30 eV a $\Delta E/E = 5\%$ was found. The energy calibration, the maximum kinetic energy and the resolutions found are in good agreement with the simulation performed by using SIMION as reported in appendix B, thus confirming the reliability of the simulation software used.

5.1.2 Rare gas clusters: XUV ionization of He nanodroplets

The first result to be shown is the study of helium nanodroplet targets. This subsection is extracted from manuscript [40]. Since it is not the purpose of this thesis to enter into details of the description of the various ionization processes, only the main features will be shown in order to validate the capacity of the experimental setup, a more complete description is given in the manuscripts from which the results presented are extracted.
Helium nanodroplets are intriguing many-body quantum systems which feature special properties such as very low equilibrium temperature (0.38 K), superfluidity, and the ability to efficiently cool and assemble embedded species ("dopants"). Therefore, pure He nanodroplets have been extensively studied using electron impact ionization as well as by photoexcitation and ionization with synchrotron radiation [40]. In this experiment, discussed in detail in paper [40], the Velocity Map Imaging spectrometer in PhotoElectron-PhotoIon COincidence (VMI-PEPICO) configuration described in section 4.1 has been used to study pure He nanodroplets. As already mentioned, the experimental setup allows the measurement of photoelectron energy spectra (PES) and angular distribution (AD) in coincidence with specific ion masses detected by the TOF mass spectrometer (for example, the typical mass spectra in fig.5.5).

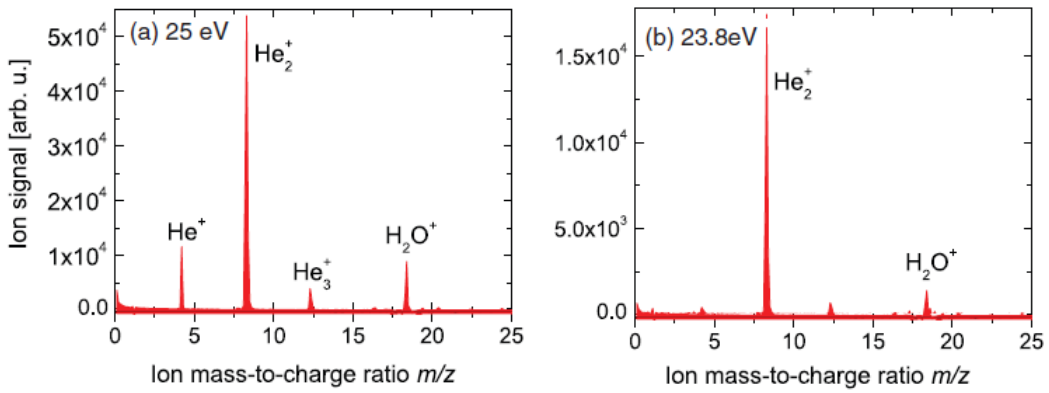

Figure 5.5: *TOF mass spectra of He nanodroplets at different photon energies: a) 25 eV, b) 23.8 eV. The He expansion conditions are p_0 = 50 bar, T_0 = 23K (N = 1900) [40].*

A mechanical chopper periodically intercepts the He droplet beam and allows one to discriminate the ion signals originating from the He droplet beam from background

gas ions. When the beam chopper is in the "open" position, both contributions are measured whereas in the "closed" position, only background ions contribute. Thus, the difference signal shows the contribution correlated to the He droplet beam only. At $h\nu$ = 25 eV (see fig. 5.5a) the He atoms in the droplets are directly ionized, whereas at $h\nu$ = 23.8 eV (fig. 5.5b) the He droplets are resonantly excited into states derived from the $1s3p^1P$ and $1s4p^1P$ atomic He levels, from which they decay by autoionization [40].
Then PES and AD have been measured in correlation with the most abundant ions He_n^+, n =1, 2, 3.
Let us first examine the AD correlating to He^+, He_2^+, and He_3^+. We point out that

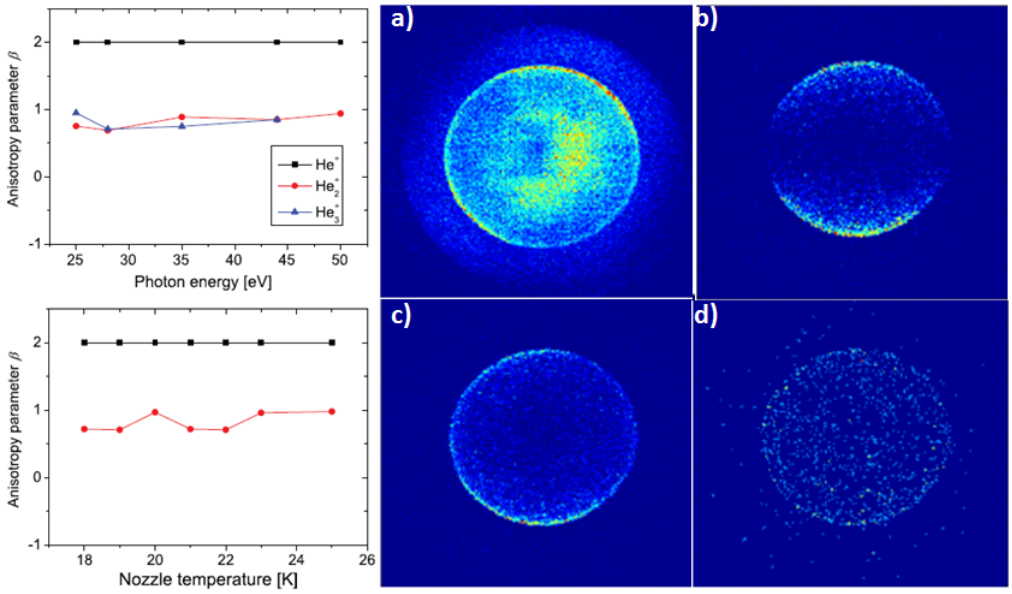

Figure 5.6: *On the Right: Raw photoelectron images: a) all the electrons, b) electrons selected in coincidence with He^+ ions, c) electrons selected in coincidence with He_2^+ ions, d) electrons selected in coincidence with He_3^+ ions. Left: upper graph, the anisotropy parameters β extracted from the relative images, at different photon energy from 25 eV up to 50 eV; lower graph, the anisotropy parameter dependence on the nozzle temperature from 18 K to 25 K and thus on the droplet size.*

without the possibility given by such a spectrometer of selecting the electrons in coincidence, the measurement of the AD of the different ionic species would be impossible as we can see from the raw image of all the events in Fig. 5.6 a). By analysing the mass-correlated photoelectron images, a reduced anisotropy of the photoelectron distributions correlating to the molecular ions He_2^+ and He_3^+ was observed. In fact while for electrons correlating to He^+ we find a constant value β= 2.0 (as expected for the direct ionization of unperturbed He atoms), for He_2^+ and He_3^+ the anisotropy parameter is reduced to β= 0.8. This anisotropy parameter was measured as a function of the photon energy from 25 eV to 50 eV and also as a function the droplet size by changing the nozzle temperature from 18 K to 25 K. No dependence on those parameters was observed. The reduced anisotropy is most probably due to elastic scattering of the outgoing photoelectron from the He droplets. Note that the first observation of the reduction of the anisotropy of the ADs from Xe clusters did not exhibit a size dependence [62]. However a better understanding of the AD and PES spectra is required and will be subject

of future investigations [40].
A PES measured at high photon energy, $h\nu$ = 50 eV, is also reported. In particular the PES correlating to He^+ and He_2^+ TOF signal. As an example, the raw image for He_2^+ is shown in the inset in Fig. 5.7 a). The PES for the two species are nearly

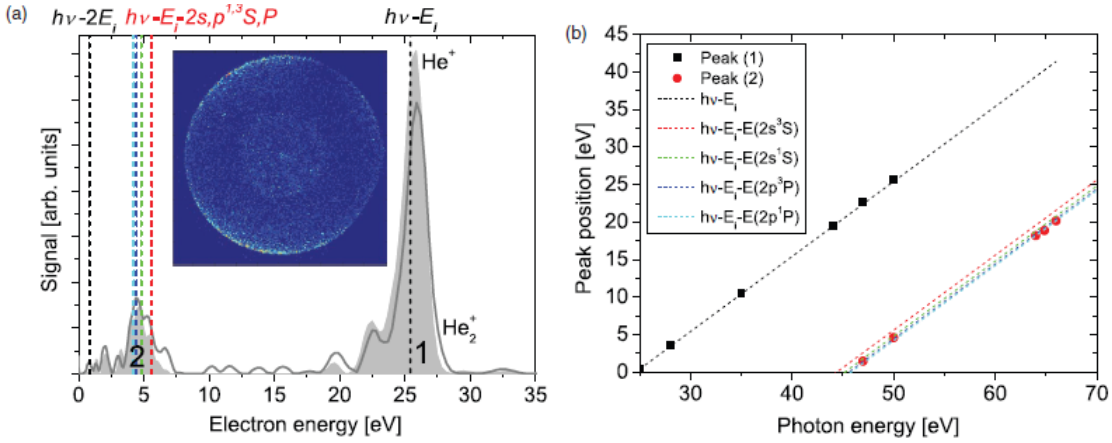

Figure 5.7: *(a) Photoelectron spectra recorded in coincidence with He^+ (shaded area) and He_2^+ (solid line) at $h\nu$ = 50 eV (p_0 = 50 bars, T_0 = 23 K). Peak 1 corresponds to electrons created directly by ionization of He atoms or He_2 dimers in the droplets. Peak 2 stems from electrons that lost energy by inelastic collisions with surrounding He atoms. The inset depicts the photoelectron image correlating to He_2^+. (b) Dependence of the peak positions on $h\nu$. The dashed lines depict the energies of photoelectrons emitted directly (black) or after energy-loss by inelastic collisions (coloured) when considering the He atomic ionization energy $E_{i,He}$ and the level energies of the $1s2s^{1,3}S$ and $1s2p^{1,3}P$ atomic levels [40].*

identical at these high photon energies. In addition to the highest peak from directly emitted electrons with energy $h\nu - E_{i,He}$ = 25.41 eV, a second peak appears at energy $E_{E-loss} = h\nu - E_{i,He} - E_{1s2s,p} \approx$5 eV. This low energy feature is present at the reduced energy E_{E-loss} in all measured spectra where $h\nu$> 46 eV, as shown in Fig. 5.7 b). It is due to the loss of kinetic energy of the photoelectrons by inelastic collisions with surrounding He atoms as they pass through the droplets in a process of the type:

$$e^-(E_{kin}) + \mathrm{He}(1s^2) \rightarrow \mathrm{He}^* + e^-(E_{kin} - E_{E-loss})$$

This interpretation is supported by a vanishing anisotropy parameter β = 0.1(3) of the AD in the full range of electron energies covered by peak (2) as opposed to β = 1.9(1) for peak (1). As expected, the information about the direction of emission of the photoelectrons is completely lost by the inelastic electron-He collisions [40].

5.1.3 Rare gas clusters: Interatomic Coulombic Decay in NeAr Dimers

The second experiment concerns the Interatomic Coulombic Decay process in clusters, which has been extensively studied by our group [57,63]. Again only the main features will be shown in order to validate the capacity of the experimental setup.
Interatomic Coulombic Decay (ICD) is a process which, although only recently predicted theoretically [64] and confirmed experimentally [65] is proving to be quite ubiquitous in van der Waals complexes (see section 1.1.2), H-bonded systems, clusters, and also condensed matter. It occurs when a system containing two or more atoms (or

molecules) is perturbed by an event which leaves a singly ionized system with one of its components with an inner valence hole. If the energy of this state lies below the double ionization potential of the isolated atom (molecule), then the system cannot decay by autoionization, but only via radiative decay which is a slow process. However, if the atom has a neighbor, the system can relax more quickly by transfer of energy from the excited ion to the neutral partner (via the Coulomb interaction) and the emission of a low energy electron from the latter. This leads to two singly ionized atoms which then undergo a Coulomb explosion as schematically reported in figure 5.8 [63].

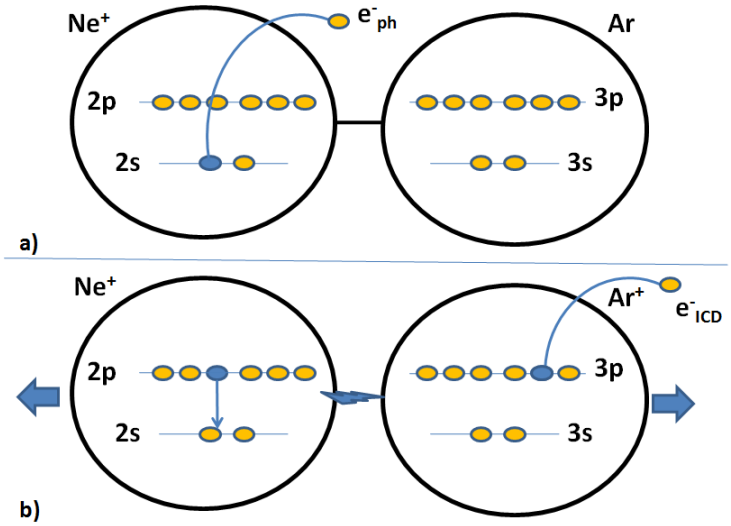

Figure 5.8: *Schematic representation of the Interatomic Coulombic Decay process occurring in NeAr dimers.*

The ICD process can be then described as follows:

$$\begin{aligned} \mathrm{Ne}(2s^2 2p^6)\mathrm{Ar} \xrightarrow{\hbar\omega} \mathrm{Ne}^+(2s^1 2p^6)\mathrm{Ar}(3s^2 3p^6) + e^-_{ph} \\ \rightarrow \mathrm{Ne}^+(2s^2 2p^5)\mathrm{Ar}^+(3s^2 3p^5) + e^-_{ICD} \end{aligned} \tag{5.1}$$

In our experiment a supersonic beam is formed by expanding a 12:1 mixture of Ne and Ar through a liquid nitrogen cooled nozzle with an internal orifice diameter of 50 μm. The resulting supersonic jet, contains < 1 % of Ne_2, Ar_2 and NeAr dimers. Focussed synchrotron radiation at 120 eV photon energy intercepts the cluster beam at right angles in the interaction region. The photoemitted electrons are guided by the electrostatic fields of the electron VMI spectrometer, while ions are accelerated in opposite direction through the TOF spectrometer. In this way, the arrival positions of the low energy electrons (< 35 eV) on the PSD are detected in coincidence with the arrival time of the ion formed in the same event. The resulting data can be analyzed to extract the velocity mapped image of electrons born in triple PhotoElectron-PhotoIon-PhotoIon-COincidence (PEPIPICO) with one Ne^+ and one Ar^+ ion [63]. Furthermore, the shape of the island formed by graphing a 2D histogram of the arrival time of the first ion against that of the second ion allows us to select momentum matched ions formed in a Coulomb explosion (see Fig. 5.9 a)) since these ions form a line with a slope of -1 in

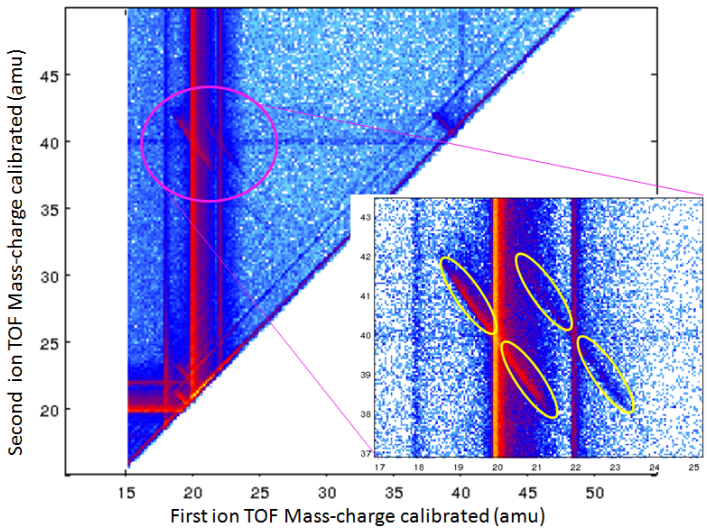

Figure 5.9: *2D histogram of the ion-ion coincidence arrival times. In the inset: zoom over the region around the Ar^+-Ne^+ ions.*

the coincidence map. Fig. 5.9 a) shows the 2D histogram of the arrival times of the first ion in coincidence with the second ion of all electron-ion-ion coincidences; Fig. 5.9 b) contains the zoom of the region with coincidences between Ne^+ and Ar^+ [63]. The vertical lines are due to false coincidences with Ne^+ ions (due to the large majority of Ne monomers in the supersonic beam) while the strong and weak lines with slopes of -1 are due to coincidences of Ar^+ ions with $^{20}Ne^+$ (90 % natural isotope abundance) and $^{22}Ne^+$ (10 % natural isotope abundance) ions [61], respectively. Only the arrival positions of the electrons corresponding to the ion coincidences contained within the ellipses on the ion-ion map are retained for the ICD electron VMI image shown in Fig.5.9 [63].

The peak of the experimental spectrum coincides very well with that of the calculated distribution for the v=0 state (thin black line). But the experimental distribution is much broader, and the FWHM of the peak is 1.5 eV. The most obvious explanation would be that the energy resolution of the instrument is not sufficient to resolve the true width of the distribution.

However, as already reported at the beginning of this chapter, the resolution of the detector system for this kinetic energy range a resolution of 9 % has been found corresponding to a broadening of 630 meV for the peak at 7.1 eV. Thus the broadening can be imputed to some other physical effect.

It is possible that the populations in the v = 1 and v = 2 levels of the ground state of the NeAr can have a large effect on the KE distribution of the ICD electrons due to the more diffuse initial wavepackets.

To demonstrate this clearly, we have calculated the relative populations of the v=0, v=1 and and v=2 vibrational levels for a vibrational temperature of 20 K (consistent with the supersonic beam we have employed) based on the potential energy curve of the ground state [66]. Using these populations as weighting coefficients (1:0.27:0.16) for the PES of the ICD electrons extracted from [67] (and shown in Fig. 5.10 (b)) and summing the resulting PES we obtain an overall distribution which is slightly narrower

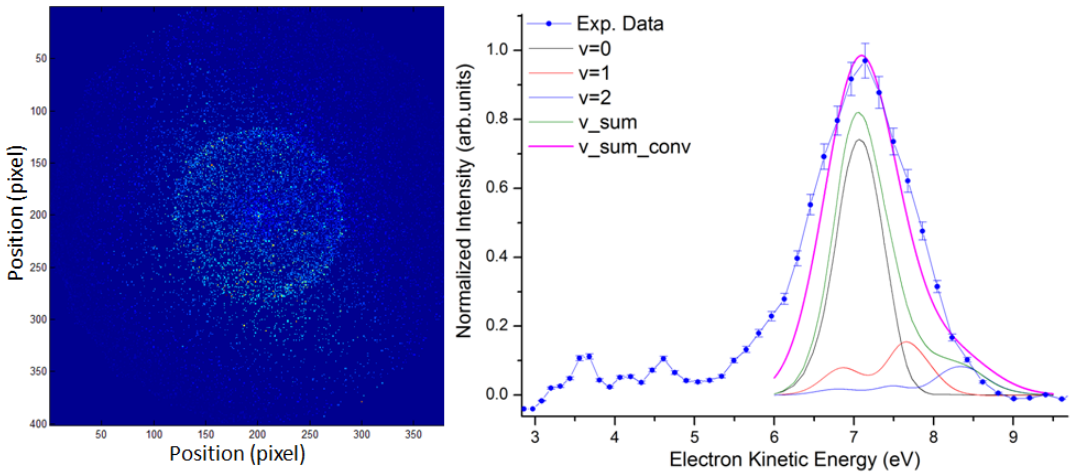

Figure 5.10: *On the left: VMI image of the electrons corresponding to the ion coincidences contained within the ellipses on the ion-ion map shown in Fig.5.9. Right: kinetic energy distribution of the low energy electrons detected in coincidence with one Ne^+ ion and one Ar^+ ion (full red line and squares) together with the ab initio calculations of the PES of ICD electrons produced following photoionization of the Ne 2s orbital of the electronic ground state of NeAr in its v=0 (thin black line), v=1 (thin red line) and v=2 (thin blue line) vibrational states. The relative contributions of the v=0, v=1 and v=2 are normalized according to a vibrational temperature of 20 K and summed (thin green line) and then convolved with the experimental resolution (thick magenta line).*

than the experimental distribution (thin green line in Fig. 5.10(b)). Once the calculated PES has been convolved with the experimental resolution (thick magenta line in Fig. 5.10(b)) the resulting KE distribution fits reasonably well the high energy side of the experimental distribution. Therefore, it is possible to explain the signal at high KE with respect to the ICD peak at 7.1 eV as being due to the initial populations of the ground state NeAr dimer in the in v= 1 and 2 states.

5.2 Experiments at FERMI

The results described in this section have been obtained with the LDM experimental setup described in section 4.2.

5.2.1 Atomic spectra (Ne,Xe)

As in the previous case of the PSD characterization used for SR applications, here again the photoionization of simple atomic targets is used to characterize the detector response. In particular photoionization of neon (IP = 21.56 eV, $\beta = 0$) targets with photons of energy 25.5 eV and an extraction voltage of $V_{repeller}$= -6 V and $V_{extractor}$= -5 V gives an ideal isotropic distribution for detector response calibration. In Fig. 5.11, two areas are clearly less sensitive. The bottom one is due to a reduced MCP efficiency for geometrical factors when the particles hit the MCP stack at an angle parallel to the bias angle. The top one, instead, results from damage due to an excessive flux of scattered photons. Atomic xenon was used to measure the TOF resolution, and the spectrum is reported in Fig. 5.12, with a photon energy of 21.7 eV. In the TOF spectrum singly and doubly ionized xenon are clearly visible as well as the products

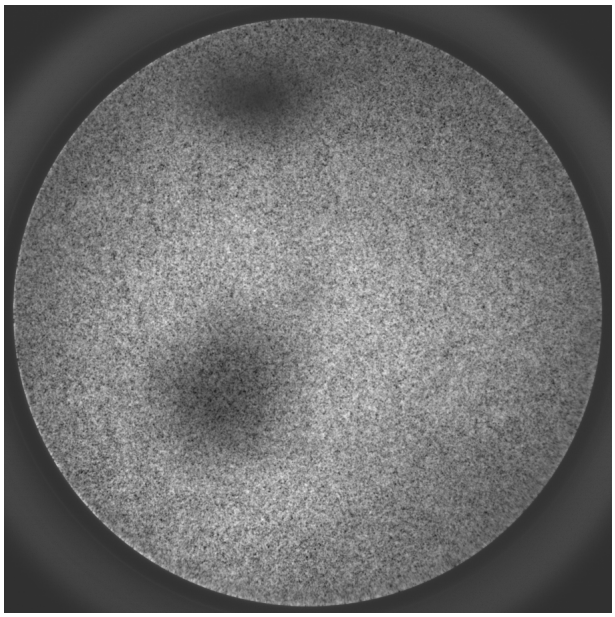

Figure 5.11: *Homogeneity response of the FEL PSD on atomic neon at photon energy 25.5 eV.*

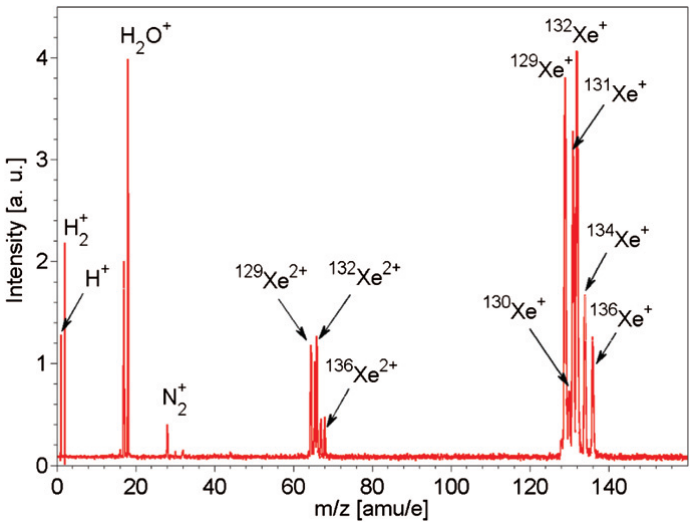

Figure 5.12: *TOF mass spectrum of xenon at photon energy 21.7 eV.*

of the ionization of the residual gas. The resolution of the TOF depends on whether it operates independently or simultaneously with the VMI. By analyzing the spectrum, the mass resolution is found to be about 350 when the VMI is set to detect electrons with maximum kinetic energy 30 eV (mode 1), while it is 1400 in the independent regime (mode 2) [49]. The ratio of xenon doubly and singly ionized ions is used to adjust the focus with the KB mirrors live in order to have the smallest spot size possible. This is possible because the formation of multi-ionized species is a multiphoton process [52] occuring at higher power densities.

5.2.2 Novel collective autoionization process in He clusters

As seen in the previous section, while synchrotron radiation offers the possibility to investigate the energetics of the targets under study, FELs offer also the unprecedented capability to study reaction dynamics and image the structure of extremely diluted complex systems. Moreover, differently from the case of synchrotron radiation studies, FELs allow the exploration of non linear dynamics. Thanks to the high power density of such a light source, large molecules or clusters can absorb a large number of photons on a femtosecond timescale. Thus it is also possible to investigate the behaviour of complex systems when multiple photons are absorbed and a plasma-like state is formed. This places the system in a highly excited, non-equilibrium state. In this section the first experimental results from a novel collective ionization mechanism based on resonant excitation of clusters is presented [58,60]. This particular ionization mechanism occurs as any two neighboring excited atoms in the cluster exchange energy between each other, leading to the decay of one atom and the ionization of the other. The process is shown schematically in Fig. 5.13. This ionization mechanism is analogous to au-

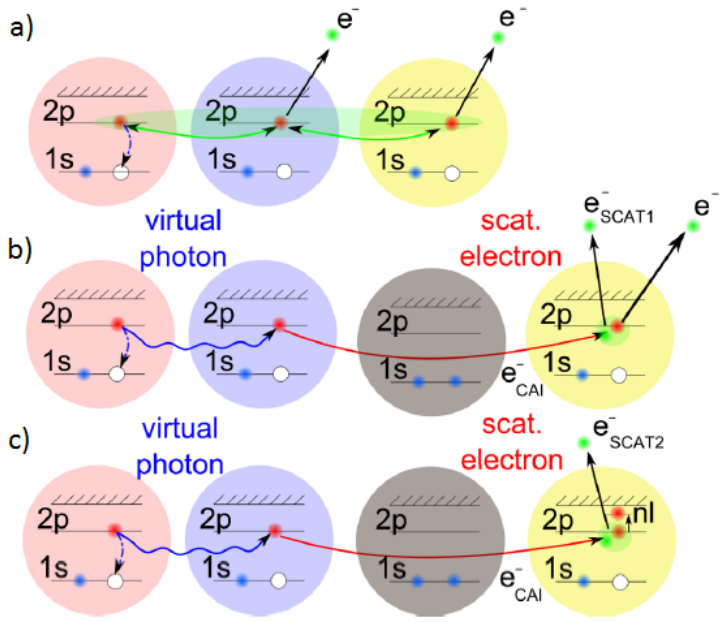

Figure 5.13: *Schematic diagrams of: a) CAI type process involving three excited atoms, and b), c) CAI with electron scattering on a third neighboring excited atom.*

toionization in atomic systems following double excitation of the system. However, in contrast to the atomic case, the excitation occurs between many neighbouring atoms, so the term Collective Autoionization (CAI) provides a better description of the process. Such processes were recently proposed in [68]. Since the decay is dependent on the energy transfer between neighboring atoms, it is a type of ICD. But unlike the conventional ICD, CAI is a resonant process where intense radiation is needed to excite at least two atomic partners. In this section the electron [60] emission and the ion yield [58] from He clusters irradiated by the intense pulses from the FEL FERMI [25] is reported. He droplets were either resonantly excited to the $2p$ atomic-like state, which is well below the ionization potential, or excited into the continuum. The electron spec-

tra recorded following excitation to the $2p$ state provide evidence for a new ionization mechanism. FEL pulses with photon energies of 21.4 and 42.8 eV having a wide range of pulse energies (0.5-60 μJ) were focused by the KB mirrors system to a spot size of around 75 μm (FWHM) diameter. The FEL polarization was chosen to be linear and the axis to be perpendicular with respect to the detector axis. The estimated pulse length is 100 fs (FWHM) (see next section). The power density is calculated to be in the 10^{10}-10^{13} W/cm^2 range. He nanodroplets containing on average up to 50 000 atoms were produced in a supersonic expansion of He gas at 50 bar stagnation pressure through the source system described in section 4.1.1 cooled to 17 $\pm$ 0.1 K. The kinetic energy distribution of emitted electrons was determined using the FEL VMI spectrometer described previously. The total electron yield for direct ionization at 42.8 eV (above IP) and for resonant excitation below the IP to the $2p$ band state at the absorption maximum around 21.4 eV are presented in Fig. 5.14 [60]. The total electron

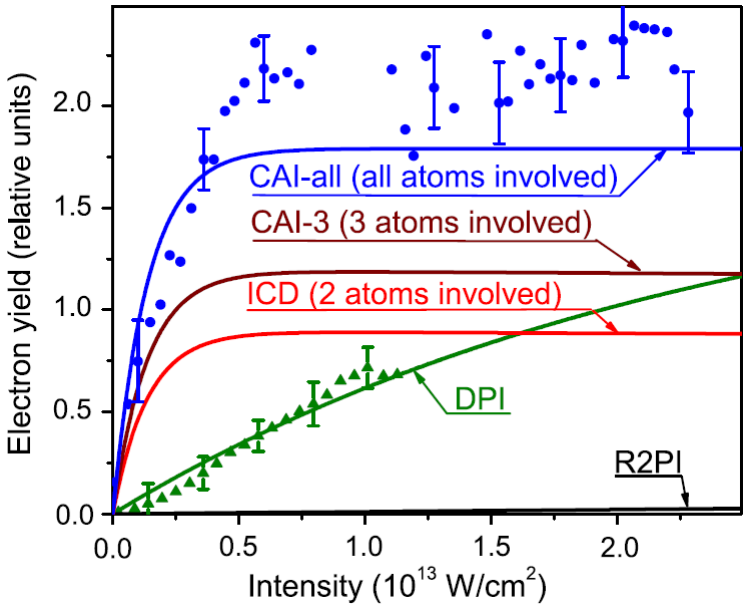

Figure 5.14: *Total electron yield vs FEL intensity for two different photon energies. Dots and triangles represent the experimental data at 21.4 and 42.8 eV, respectively. Curves labelled R2PI and ICD indicate theoretical electron yields for the resonant two-photon ionization process and ICD process at 21.4 eV, respectively. Curves labelled CAI-3 and CAI-all represent the theoretical yield for the CAI process where three and all excited atoms are involved, respectively. DPI shows the rate for the direct photoionization process at 42.8 eV ($\sigma_i \approx 2.89$ Mb [69]). The theoretical electron yields are normalized to the experimental data through the DPI process. Figure taken from the original paper [60]*

yields versus FEL intensity at 21.4 and 42.8 eV are depicted in the figure. Experimental points are obtained by integrating the single-shot VMI images and binning them (5 $\mu J/step$) according to the incoming pulse energies. The experimental results demonstrate that the electron yield of resonant 2p excitation (dots) is much higher than that of direct excitation into the continuum above the IP (triangles). The yield for the direct photoionization process (42.8 eV, DPI in Fig. 5.14) is lower than the electron emission rate at 21.4 eV (ICD), calculated for the ICD process with two excited atoms involved. In these calculations it is assumed that all atoms in the cluster can be excited and that

after the pulse, all excited atoms decay by the ICD process. Although the details of autoionization involving two, three (CAI-3), or many excited atoms (CAI-all) are different, the total electron yield is expected to be rather similar since it is only governed by the large single photoabsorption cross section of the He 1s → 2p transition, at least at high power density. This result is supported by measuring simultaneously the total ion yield, by means of the TOF spectrometer [58]. In first-order perturbation theory the ionization rate is $\Gamma = \sigma I^n$, where σ is the cross section, I is the photon intensity and n the number of absorbed photons. For photon energies below the ionization threshold, multiple photons are required to ionize the system. In contrast, ionization through CAI is based on the absorption of single photons by multiple atoms within the cluster. The energy required for ionization of the excited atom is gained by the ICD of a neighboring excited atom. In the case of CAI one therefore expects a linear intensity dependence of the ionization rate, while in two-photon absorption by a single atom a quadratic power dependence is expected. Then by measurement of the ion yields it should be possible to distinguish CAI from resonant two-photon ionization. The dependence of the ion signal on the light intensity is shown in Fig. 5.15 for three photon energies [58]. Normalized

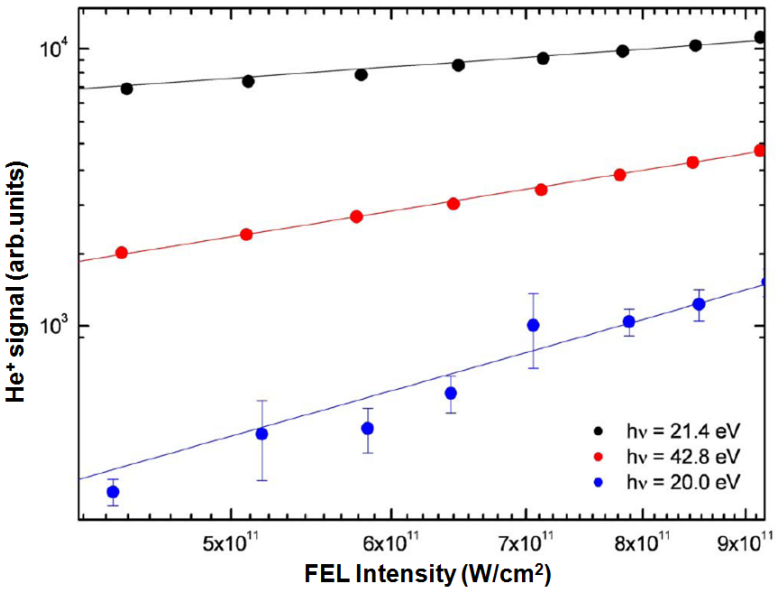

Figure 5.15: *Power dependence and relative ion abundances for photon energies: 21.4 eV (black circles), 42.8 eV (red circles), 20.0 eV (blue circles) along with power dependence fits (lines of corresponding colour). Figure taken from the original paper [58].*

data are plotted on a log-log scale. As a result, the slope of a pseudo-linear fit to the data is proportional to the number of absorbed photons. At a photon energy of 42.8 eV, well above the ionization potential of helium, atoms are ionized by the absorption of a single photon. The slope of 1.07 $\pm$ 0.01 obtained from the fit clearly shows that direct ionization of the system is a one photon process. At 20.0 eV, the clusters are transparent and the absorption of at least two photons is required for ionization. The slope of 2.06 $\pm$ 0.09 determined from the data confirms this. Since the 1s2p $\leftarrow$ $1s^2$ transition has the highest absorption cross section, it is the best candidate for observing CAI. For rare gas clusters, the absorption spectrum is quite different from atomic systems. The transitions are no longer narrow lines, but broad features shifted in energy with respect

to the free atom due to the excited electron being perturbed by neighboring atoms. As a result the maximum of the 1s2p $\leftarrow$ $1s^2$ absorption in the cluster corresponds to a photon energy of 21.4 eV. For this resonant excitation of the system a slope of 0.63 $\pm$ 0.01 is found. The fact that the power dependence is less than one can be attributed to partial saturation of the 1s2p $\leftarrow$ $1s^2$ transition, which is estimated to have a large cross section, 25 Mbarn [58]. Thus the system is ionized via the collective ionization process described above.

5.2.3 Temporal overlap in two colours pump and probe experiments

In two colours pump and probe experiments the spatial and temporal overlap of the two beams is a necessary condition. This subsection shows how this experimental setup has been used to characterize the laser beam transport optics system of the LDM beamline for this class of experiments. The FEL and the Near Infra-Red (NIR) or UV (both avalaible) pulses are combined into the experimental chamber thanks to the recombination mirror (see Fig. 4.13 in section 4.2). The spatial overlap is determined by visual inspection of the images of both beams on an Yttrium Aluminium Garnet monitor which can be inserted into the interaction chamber. The temporal overlap is controlled by a delay stage in the NIR/UV-laser delivery system and optimized using first a coaxial cable antenna and then directly the two-colour two-photon ionization signals of an atomic gaseous target. In Fig. 5.16 the energy level scheme of neon (IP= 21.564 eV [6]) is reported.

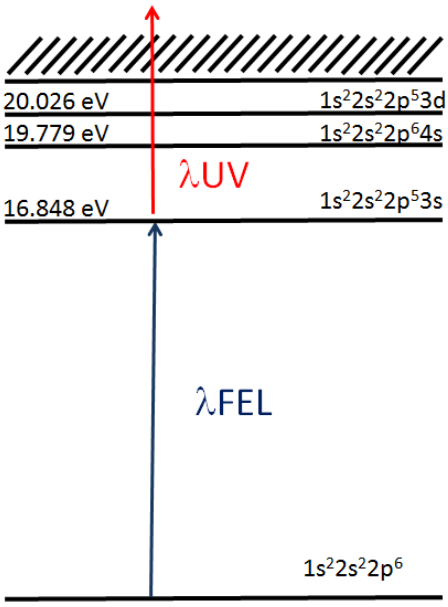

Figure 5.16: *Scheme of the energy levels of Ne and scheme of pump and probe beams for checking the temporal overlap condition in two colours pump and probe experiment.*

In the scheme of 5.16 the FEL light (with a photon energy of 16.85 eV) acts as the pump by resonantly exciting neon gaseous targets from the ground state to the 3s excited level state (lifetime $\tau = 1.6ns$ [6]). The UV laser with a photon energy of 4.75 eV is then used as the probe. When spatial and temporal overlap conditions hold

two-photon ionization of the atomic gas occurs and electron photoemission is observed. This system is then used to find the zero time delay between the two colours in pump and probe experiments. In fact by observing the electron VMI images integrated signal dependence on the time delay between FEL and UV light one obtains a typical graph as reported in Fig. 5.17. In Fig. 5.17 the electron yield has been extracted by integration

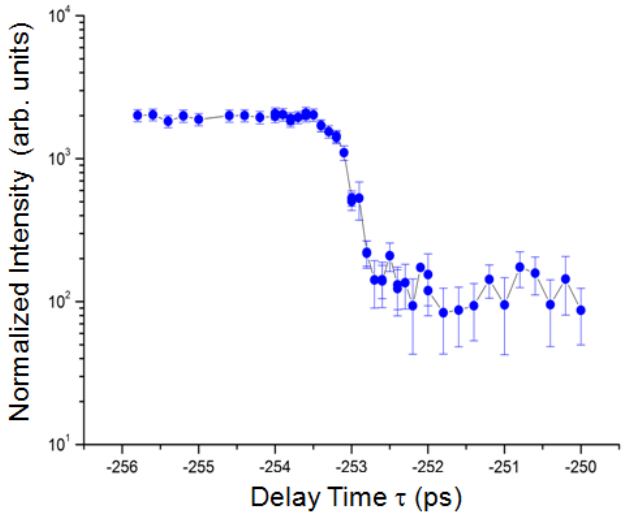

Figure 5.17: *VMI electron yield dependence on the time delay between the FEL light and the UV light. The zero time delay between the two colours is set at the inflection point (-253.15 ps).*

on the VMI image and plotted (log scale) in dependence of the time delay between the FEL and UV beams at a step of 150 fs. At the inflection point of the curve obtained one finds the zero time delay between the two pulses, so in this case at a value of the delay line system of -253.15 ps. The method described above has become a standard procedure at the LDM beamline for checking the superposition of the two colours. Thanks to the high tunability of the FERMI FEL light, this procedure can be performed on whatever gasoues target by selecting a specific resonance. It is noteworthy that the whole aquisition time needed to perform this temporal overlap checking procedure in two colours experiments is about 15 min.

5.2.4 Cross-correlation method for the FERMI pulse duration

A series of experiments have been performed at the Low Density Matter (LDM) beamline for determining the temporal pulse duration of the FERMI FEL light. Differently from the previous case, in this application the FEL light has a photon energy above the IP of the target. The photoelectron energy spectrum consists of a main line associated with the direct photoemission process, which in the presence of a high power NIR laser is accompanied by the so-called “sideband” lines, located symmetrically on each side [70]. The sidebands are very sensitive to the spatial and temporal overlap and to the physical characteristics of both the XUV and NIR pulses. Equally spaced sidebands, that are separated from each other by $\Delta E = h\nu_L$, are associated with the additional exchange of optical laser photons with frequency ν_L, through absorption and/or stimulated emission processes [70]. A scheme of this process for atomic He targets is reported in Fig. 5.18. The FEL light has a photon energy of $h\nu_{FEL} = 48.4$ eV (25.6

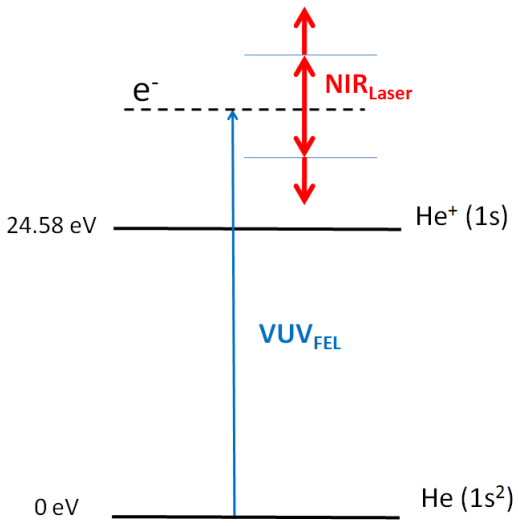

Figure 5.18: *Energy levels of He and scheme of the two-colour experiment with observation of sidebands in He.*

nm), the NIR light from a Ti:Sa laser with photon energy $h\nu_L = 1.58$ eV (783 nm), the He IP is 24.6 eV. The FEL beam spot size is 50 μm diameter while for the NIR is 150 μm. Let us first consider the ponderomotive energy (also called quiver energy) (U_P) which describes the average oscillation energy that is acquired by a free electron in the radiation field of the laser pulse, according to the following equation [71]:

$$U_P = \frac{q^2\xi_0^2}{4m_e\omega^2} = \frac{q^2}{2m_e\epsilon_0 c\omega^2} I_L \tag{5.2}$$

where q is the electron charge, ξ_0 is the electric field amplitude, m_e is the electron mass, c the speed of light, ω the angular frequency of the laser radiation and I_L the laser intensity. In more practical units it can be expressed as [72]:

$$U_P[eV] = 9.34 \times 10^{-20} \times (\lambda[nm])^2 \times I_L[W/cm^2] \tag{5.3}$$

Then the ponderomotive energy (U_P) is expected to shift the kinetic energy by a very small amount ($\approx 5 \times 10^{-2}$ eV) at the laser intensity used $I_L = 2.5 \times 10^{11}$ W/cm^2. The outgoing photoelectron kinetic energy, neglecting the small shift due the ponderomotive energy, results is found to be equal to:

$$E^e_{kin} = h\nu_{FEL} - IP \pm nh\nu_L \tag{5.4}$$

The corresponding image acquired with the VMI spectrometer at the zero time delay is reported in Fig. 5.19: In Fig. 5.19 a) the raw electron VMI image, background subtracted; b) enlarged image of the main normal photoline where the appearance of the sidebands due to the dressing of the NIR laser is clearly visible. As stated above, the high sensitivity of the sidebands to the spatial and temporal overlap and to the physical characteristics of both the XUV and NIR pulses has been used here to characterize the FERMI FEL pulse duration via cross-correlation measurements, by changing the delay between the NIR laser pulse and the FEL pulse. It is important to point out that

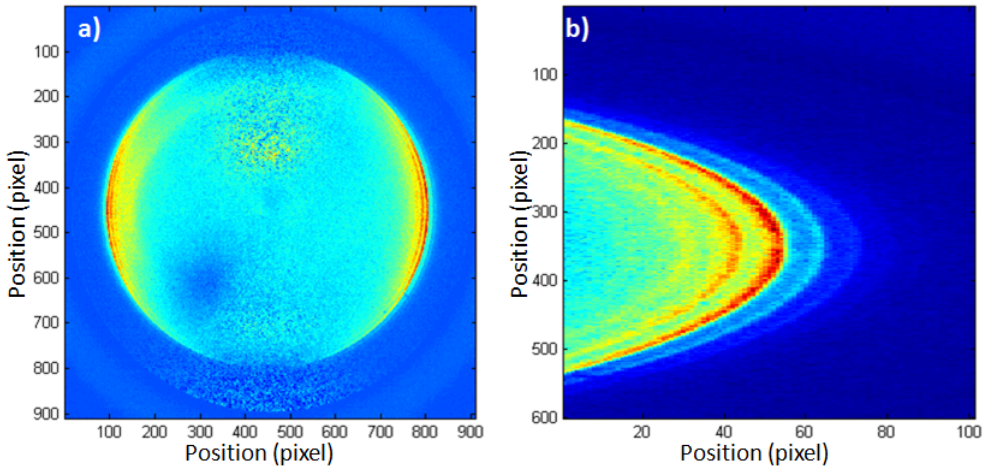

Figure 5.19: *a) the raw electron VMI image, background subtracted; b) zoomed image showing the He sidebands in detail.*

this kind of measurement is feasible at FERMI because it is a seeded FEL and can be considered a light source with nearly jitter-free timing [73]. In fact in SASE FELs, such an experiment is very difficult considering that the typical timing jitter between consecutive pulses, within the electron bunch, can be of the order of hundreds of fs, thus equal or even higher than the pulse duration itself that one should measure. According to lowest-order perturbation theory [74], the population of the n-th sideband, $I_{sb}^{(n)}$, is proportional to the product of the intensity of the pump pulse, I_{FEL}, and of the probe pulse raised to the power n, $(I_L)^n$ [74, 75]. Assuming Gaussian temporal profiles for both laser pulses in the cross-correlation experiment, the full-width at half-maximum (FWHM) of the cross-correlation signals (τ_C) for the n-th sideband is related to the X-ray FEL pulse duration (τ_{FEL}), the IR laser pulse duration (τ_L), and the jitter time (τ_{jitter}) between the FEL and IR laser by the following equation:

$$\tau_C = \sqrt{\tau_{jitter}^2 + \tau_{FEL}^2 + \frac{\tau_L^2}{n}} \tag{5.5}$$

As mentioned, timing jitter (i.e., the first term in the sum) can be neglected. More importantly, lower-order perturbation theory breaks down when the IR laser field becomes more intense and n should be replaced by an effective parameter α [75]. Therefore, the relationship between the cross-correlation width and the IR pulse duration in Eq.5.5 can be simplified as follows:

$$\tau_C = \sqrt{\tau_{FEL}^2 + \frac{\tau_L^2}{\alpha}} \tag{5.6}$$

where the parameter α represents the effective intensity dependence of the n-th sideband on the IR laser intensity, specifically, $I_{sb}^{(n)} \approx (I_L)^{\alpha}$. To characterize the FEL pulse duration or jitter time reliably, the parameter α must be carefully considered [75]. As reported in reference [75], the intensity dependences of the sidebands are studied based on the soft-photon approximation (SPA) [70]. In this paper it is stated that for NIR laser intensities below 3×10^{11} W/cm^2 the parameter α can be approximated by n, the order of the sideband and thus eq. 5.6 is considered. Then by changing the delay

between the NIR laser and the FEL pulse in steps of 20 fs (in the central region) and plotting the integrated signal by selecting the region of interest of the 1^{st}, 2^{nd} and 3^{rd} sideband (SB1, SB2, SB3) on the electron VMI image normalized to the integrated signal from the main band, the graph in Fig. 5.20 is obtained. By fitting our results

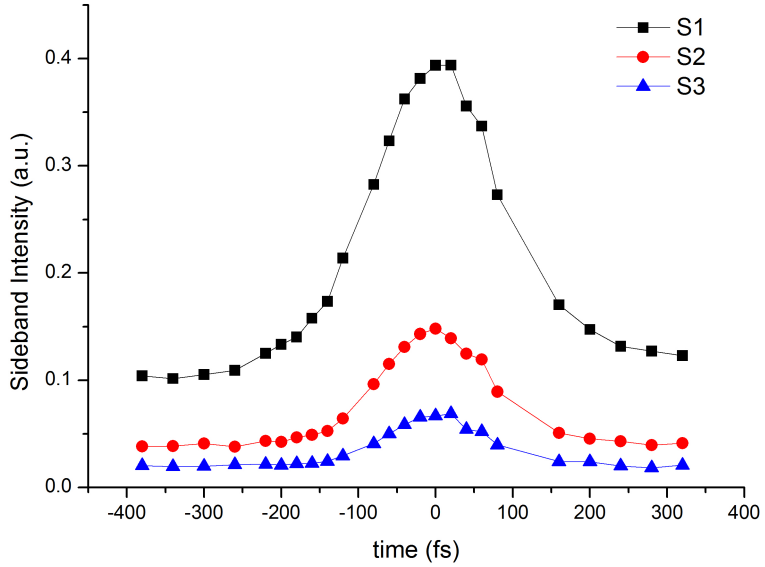

Figure 5.20: *Electron VMI image integrated signal over the region of interest for the 1^{st}, 2^{nd} and 3^{rd} sideband (SB1 (black), SB2 (red), SB3 (blue)) normalized to the integrated main band signal vs the time delay between FEL and IR laser.*

with a Gaussian distribution model of the the cross-correlation curves, a FWHM (τ_C in 5.6) of (196 $\pm$ 6) fs, (164 $\pm$ 4) fs and (146 $\pm$ 5) fs is obtained for the SB1, SB2, SB3 respectively and thus considering the FWHM of the NIR laser was equal to τ_L=175 fs this leads to a FWHM of the FEL pulse of τ_{FEL}= 88 fs, 108 fs, 105 fs. The error of the measurement, has been estimated to be around 31 fs. These results confirm that the approximation used, ($\alpha \approx n$), is reasonable within the error limits. However the values obtained exhibit a certain difference in particular between SB1 and SB2, SB3. This can be explained by the fact that for lower order sidebands the signal saturation occurs at a lower power intesity than for the higher order ones as confirmed also in [75]. Hence the values obtained for the FEL pulse duration by the higher order sidebands (SB2 and SB3) are considered more realiable than the one obtained by integrating on SB1.

5.2.5 Auto-correlation method for the FERMI pulse duration

In the previous sections we have exploited the capabilities of our detection system in the investigation of a new ionization process promoted by light-matter interaction. It has been also demonstrated that the setup can be used to characterize one of the most important light source parameters, the pulse duration, by means of two colours pump and probe experiments. In this section we will describe its use in a one colour pump and probe scheme for the commissioning of the recently built XUV/XUV delay line

of FERMI. In this case we carried out autocorrelation measurements on helium two-photon double ionization with a double goal: probe the capabilities of the new delay line, while at the same time, give an alternative measure of the FERMI pulse duration. In particular the He^{2+} ion yield dependence on the time delay between the pulses of incident light with photon energy of 52.24 eV (23.73 nm) has been examined in order to determine the pulse duration of FERMI. The FEL pulse delay is controlled by splitting the beam and using a new delay line designed and commissioned by the Photon Analysis Delivery and REduction System (PADReS) group of Elettra [50]. If the contribution to the He^{2+} signal is purely due to the direct two photon (D2P) double ionization process , the simple auto-correlation measurement of doubly charged helium can be used to determine the average pulse duration of FERMI. FEL-1 was optimized at 23.73 nm (52.24 eV), which corresponds to the 11^{th} harmonic of the seed laser wavelength (261.0 nm) for technical reasons independent from the double ionization experiment, but mainly related to the best tuning of the electron beam and control of the FEL output, in view of a thorough campaign of measurements of FEL photon pulse duration as a function of FEL-1 machine parameters. At the FEL intensity regime of about 10^{14} W/cm^2 and for this particular choice of wavelength, though, double ionization of helium could in principle proceed not only through the D2P process, but also through two other ionization channels, both related to the probability of second ionization of a singly charged helium ion produced by interaction of a first FEL photon with neutral helium. In fact at wavelengths below 45.6 nm sequential three photon double ionization of helium at a FEL may occur by direct non resonant two photon ionization (NR2P) of the singly charged helium. Additionally, at specific wavelengths below 30.4 nm excitation of He^+ to a Rydberg state may occur, enhancing the probability of the sequential 3 photon (S3P) double ionization of helium. This could be case at 23.73 nm, where absorption of a FEL photon may promote the singly charged helium ion to the He^+1s5p Rydberg excited state. A scheme of the three possible processes is reported in Fig. 5.21.

In any case for the FEL intensity used, the doubly ionized helium production is mostly due to the D2P process and the effect of the NR2P and S3P channels can be neglected (for a complete discussion refer to appendix C). The autocorrelation signal can be considered due only to the D2P process and thus used for measuring the pulse temporal duration of FERMI. The results that follow have been acquired during the beamtime on 11-21/11/2013 at the Low Density Matter (LDM) beamline [49].
The FEL beam is split in two delayed pulses of comparable intensity obtained by using the newly built PADRES delay line, a scheme is reported in Fig. 5.22.

The FEL beam is split by a mirror and fed into two different arms. Arm1 in Fig. 5.22 is a fixed path arm, while in Arm2 the optical path can be varied by moving two mirrors with a resolution defined by the motor step of 10 μm corresponding to a minimum adjustable delay step of 0.3 fs. The beam path can be varied from -0.45 mm to 9 mm corresponding to a delay -1.5 ps to 30 ps between the two pulses. At the exit side of the delay line chamber the two pulses are recombined. The spatial overlap between the two pulses has been monitored by using a YAG screen in the LDM experimental chamber, with the screen located in the focal plane of a CCD camera. The temporal overlap has been measured by using a Shack-Hartmann wavefront sensors [76] located downstream of the LDM chamber. The LDM endstation is equipped

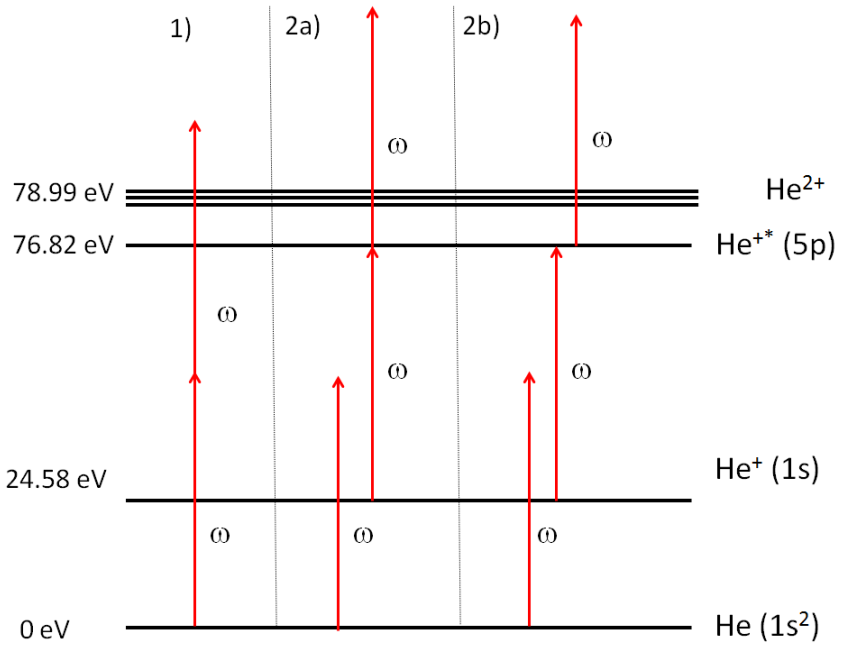

Figure 5.21: *Excitation scheme for a photon energy of 52.24 eV: 1) direct two photon (D2P) double ionization, 2a) non-resonant two-photon ionization (NR2P), 2b) sequential three photon (S3P) double ionization.*

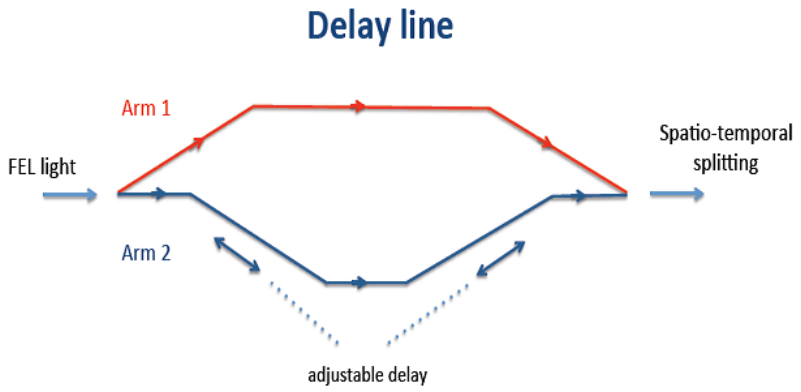

Figure 5.22: *PADReS Delay Line conceptual scheme.*

with the pulsed source described in 4.1.1 that provides a pulsed beam of helium gas synchronized with the FEL shots. The LDM interaction chamber consists of a Velocity Map Imaging focusing system coupled with a 2D detector (not used in this experiment) and a Time-Of-Flight mass spectrometer (TOF) [49] used to extract the autocorrelation signal described in the previous sections. The choice of using the TOF spectrometer instead of the VMI has been adopted in this case in order to have a simpler and faster detection and data analysis system with the purpose of characterizing the new delay line setup performance. Then the TOF spectrum of the ionic species produced by photoionization has been recorded. In Fig. 5.23 a typical TOF spectrum obtained with

such a detector is shown. In order to extract the FEL pulse duration a series of TOF

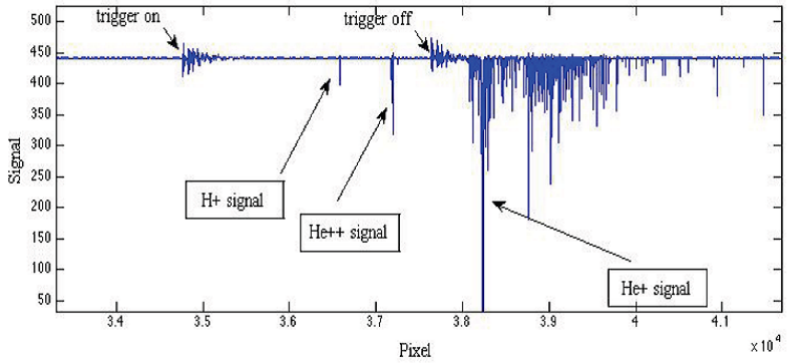

Figure 5.23: *TOF spectrum obtained at the LDM endstation.*

spectra have been acquired while changing the delay between the two pulses and monitoring the He doubly ionized signal rate. Since the signal of the helium singly ionized species was too high and could saturate the detector, a fast HV switch (Behlke [77]) has been used for gating the MCP to suppress the He^+ signal. In the TOF spectrum, noise from the trigger start and trigger stop signal of the HV switching, the He doubly ionized signal are clearly visible. In Fig. 5.24 a scan of the delay between the two pulses was recorded when the seed laser pulse was nearly chirp compensated. A shot-to-shot normalization to the incident flux was performed. Assuming a Gaussian-shaped pulse,

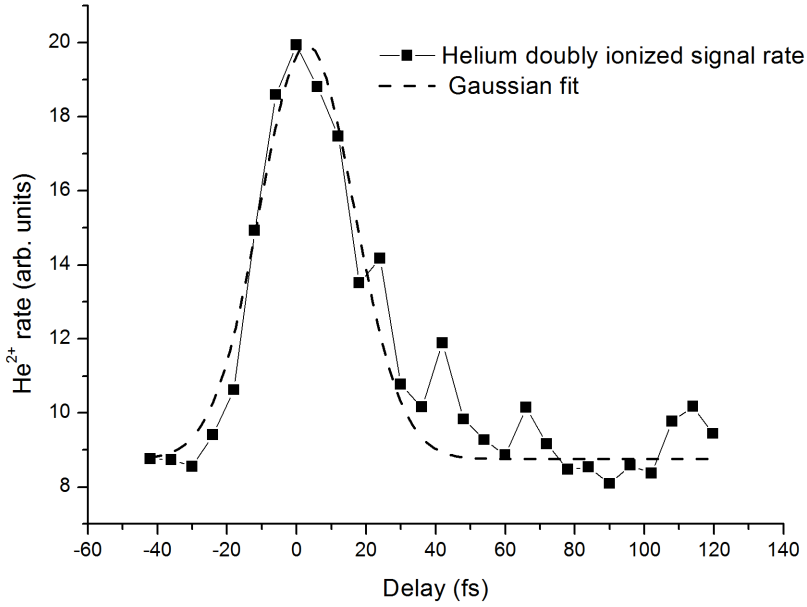

Figure 5.24: *Auto-correlation signal of doubly charged helium vs time delay between the FEL pulses (solid line + squares) and Gaussian fit (dashed line). Shot-to-shot normalization to incident flux was performed.*

the experimental data was fitted with a FWHM of 36 fs (goodness of fit 91 $\%$ (Adj. R-Square). Assuming that only the D2P process is dominant (as discussed in appendix C) and dividing then by the $\sqrt{2}$ factor the pulse duration estimation is then about 25.4 fs. This result is clearly in contrast with the result obtained with the cross-correlation method. For these reasons, it is believed that something was not working properly, the newly built delay line was suspected. As a result of this measurements a thorough investigation of the delay line system was performed and a problem with the splitting mirrors was then found. A mechanical problem with the translation stage of one of the mirrors was found. In particular, the spatial overlap between the two photon beams coming from different arms could not be guaranteed for the whole range of delays at the tight focusing conditions required for this experiment. This problem explained the unrealistically short pulse duration measured. The experiment will be repeated after factory mainteinance of the delay line.

5.3 Fast beam monitors based on diamond detectors

In new generation light sources, the use of devices able to measure the photon beam characteristics (such as photon beam position, absolute intensity and temporal structure [78]) is fundamental for users and machine operation. Real time feedbacks are necessary for optimal function of radiation sources, stability of the performance and to deliver quantitative bunch to bunch informations to users [79]. The low frequency readout system (see section 4.3) has been used to measure the homogeneity response of the diamond detector as well as for Beam Position Monitoring purposes [32, 33]. In particular, the homogeneity test reported in Fig. 5.25 was carried out at the X-ray Fluorescence bending-magnet beamline of Elettra [80]. After being generated by the accelerator, broad-band radiation (ranging from infrared to hard X-rays) passes through several absorption stages; since no monochromator was inserted in the light path, the present experiments were performed with radiation showing a maximum estimated flux of $7.30\times10^{10}\ ph/s/mrad^2/0.1\%BW$ at an energy of 20 keV and a spread of about 15 keV. At the end of the evacuated tubes, a double-slit collimator was used to obtain a rectangular beam with adjustable cross section dimensions ranging from 75 μm to 2 mm. For the test a rectangular slit with a section of 70×350 μm^2 has been used in combination with the stepper motors. The mesh scan in Fig. 5.25 a) has been obtained where an inhomogeneity, defined as the standard deviation from the mean response, of the order of 2% has been found.
In Fig. 5.25 b) the beam position on one axis (horizontal) was determined by measuring separately the current from each front electrode and moving again the detector with respect to the incident beam (as outlined in the inset of the figure). The difference-over-sum technique (see section 3.3) can be used to calculate the beam centroid position during the scans. The detectors proved to be capable of monitoring position in the central linear region with a precision below 150 nm.

With the high frequency readout system, it is possible to monitor the intensity and temporal structure for SR light sources. For this purpose the Elettra synchrotron storage ring was filled, upon our request, in Hybrid Mode (HM). In such a configuration most of the 432 buckets (separated by 2 ns) are uniformly filled leaving an empty gap,

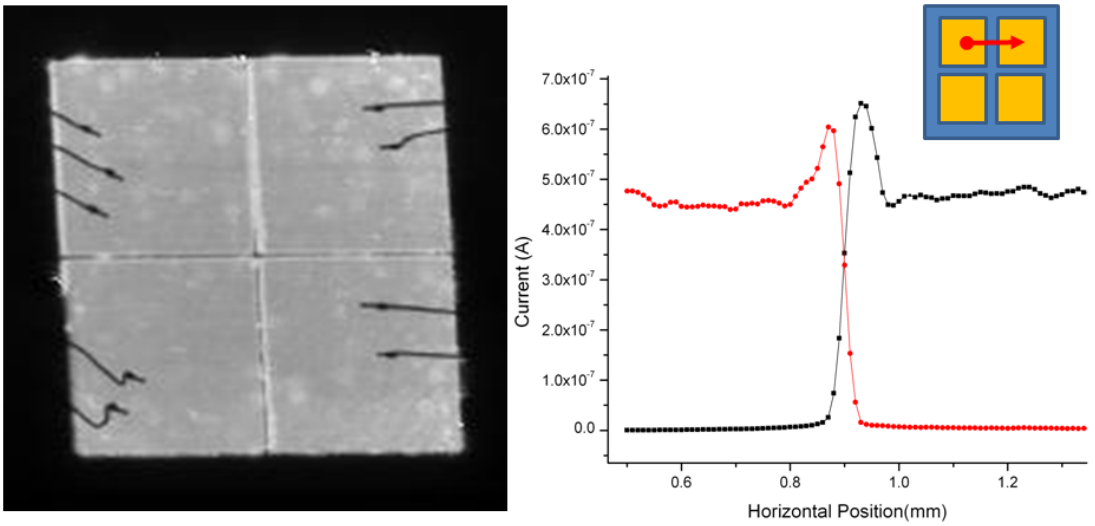

Figure 5.25: *a) Homogeneity mesh scan test of the detector. b) Horizontal beam position estimation, measured by moving the detector at a motor step of 10 μm with respect to the incident beam.*

called Dark Gap (DG) of about 40 buckets. In the middle of that gap a single electron bunch (with about 4 mA) is injected. Such a bunch is called the Hybrid Peak (HP). Since ELETTRA was in "Top-Up" operation mode the current for the bunches was not decaying in time.
The characterization was carried out at the end station of the Circular Polarization (CiPo) beamline of Elettra [81]. The insertion device of the beamline can provide radiation between 40 eV and 1000 eV in which the energy can be selected with a Spherical Grating Monochromator working in Padmore-type configuration and is equipped with a variable angle plane mirror and four different spherical gratings. In order to maximize the signal on the detector the grating with higher efficiency was selected (G4, centre energy 70 eV) and the slits of the beamline were adjusted in order to provide a $200 \times 200 \mu m^2$ spot size at the device position. Figure 5.26 a) reports the data acquired with the diamond detector for two synchrotron revolution periods that shows the time structure of the beam in hybrid mode configuration. In fact we can clearly distinguish the hybrid peaks in the middle of the dark gap separated by 864 ns which is exactly one synchrotron period.
It is noteworthy that the baseline level of the signal is the same for the isolated peak in the dark gap and the one in the multi peaks, which provides the possibility to separate the contribution from single peaks. In b) an enlargement of the hybrid peak reveals the presence of a small bunch probably due to some electrons injected into the adjacent bucket. This is also confirmed by the electron beam position monitor presently used by the control room as a diagnostic system and reported in Fig. 5.26 d).
Analysing the central peak of Fig. (5.26 b), it is evident that there is no signal reflection, confirming the good quality of the 50 Ω matched system. A single Gauss curve (corresponding to the shape of the emitting electron bunch) was used to fit the peak. The fit results are in agreement with the experimental data with a correlation coefficient of 0.988. Part of the mismatch between the fit and the data has to be attributed to a small tail after the peak probably due to the relaxation of charge into the diamond device after

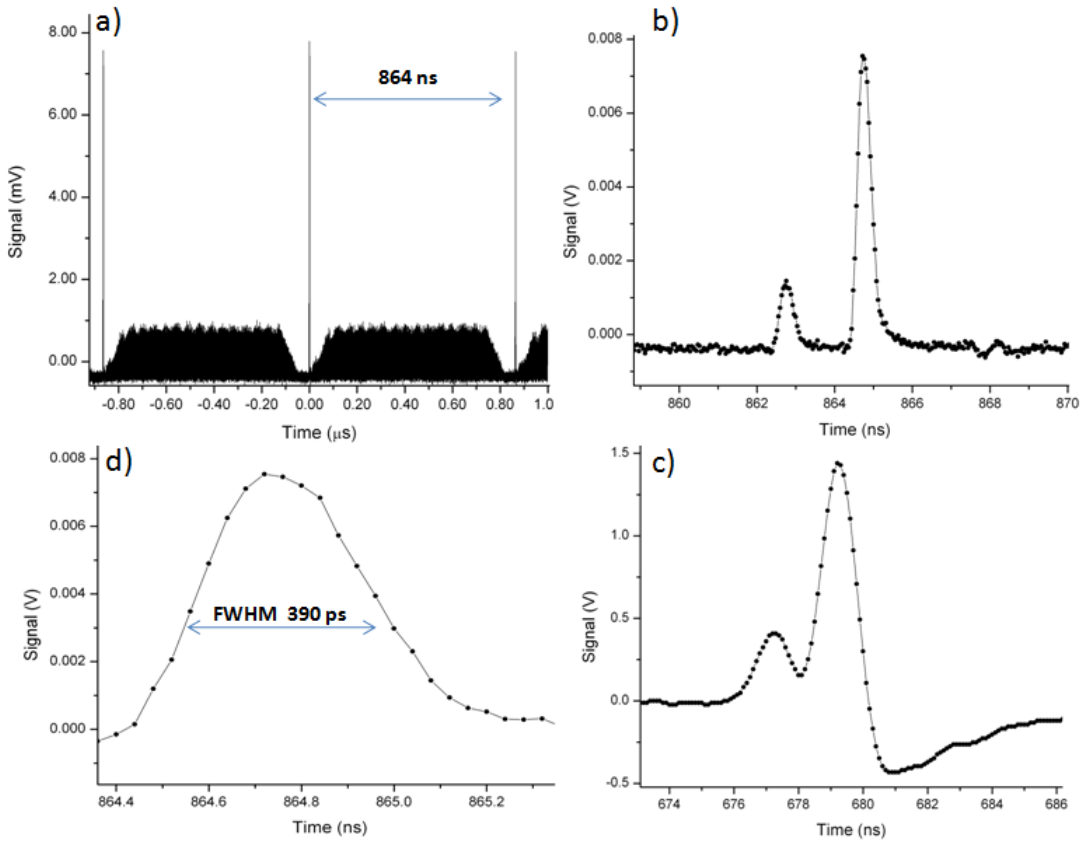

Figure 5.26: *a) the hybrid mode temporal structure of Elettra with the dark gap and the single bunch in the middle. b) zoom of the single bunch in the dark gap. c) The corresponding signal from the control room diagnostic system. d) zoom of the single Hybrid Peak for response time estimation.*

the incident pulse. The peak rise time is about 200 ps with a FWHM of 389 ps. The latter has to be compared with the width of the electron bunches that is expected to be 180 ps. The difference can be attributed to the time required to inject the charge into the diamond. By reducing the thickness of the detector we can expect to increase the time resolution.

Conclusions

The results presented in this thesis fall into two categories: the development of advanced methods for electron spectroscopy in the gas phase at modern accelerator based light sources; the characterization of the light sources for such advanced spectroscopic applications.
In particular the first category concerns the development of an experimental setup devoted to the analysis of energy and angular distribution of photoelectrons by means of VUV spectroscopy for the GasPhase beamline of the Elettra Italian synchrotron laboratory in Trieste. This experimental setup consists of a detection system built around a time-of-flight mass spectrometer and a velocity map imaging electron spectrometer. During my doctoral project, this system, including the position sensitive detector based on a cross delay line detector, has been completely assembled and characterized (paper 8 submitted).
The experimental setup has also demonstrated the required flexibility for possible Free Electron Laser applications, where the use of a different position sensitive detector is needed to overcome problems due to the high rate of events per photon pulse. In fact by replacing the last stage of the detection system with a position sensitive detector based on a homemade phosphor screen, the use of this second expertimental setup has been demostrated with a preliminary test performed at the Low Density Matter beamline of the seeded FEL FERMI. This test has been done in parallel to the construction of the current LDM endstation (a project involving several international institutions) where a commercial phosphor screen as 2D detector has been used (paper 3 and 7). A complete characterization of this detection system has been performed as well and reported in this thesis.
By using these experimental setups interesting results concerning photoelectron transition processes in simple atomic species and rare gas clusters have been obtained. In particular results on pure helium clusters and NeAr dimers (papers 1,2,10,11) by using PhotoElectronPhotoIonCOincidence as well as PhotElectronPhotoIonPhotoIonCOincidence spectroscopy at the Gasphase beamline have been reported. The results obtained have revealed energy-loss processes by inelastic collisions of the photoelectrons with He atoms in the droplets. Studies on NeAr dimers investigating in particular the kinetic energy distribution of ICD electrons following photionization of 2s electrons, have re-

vealed a good agreement with the calculations. Also a contribution to the spectrum due to the population of the vibrational excited states v=1 and v=2 has been found.
In addition at the LDM beamline novel multiphoton processes occurring in helium clusters have been investigated (papers 4, 5 and 15) and discussed in this thesis work. The results obtained have revealed a novel collective ionization mechanism based on resonant excitation of clusters.
If on the one hand these results have validated the experimental setup used, on the other some limitations have also emerged. In fact the use of such a VMI system limits its application to the kinetic energy ranges exploited in this thesis work (tens of eV). For lower kinetic energy ranges (hundreds of meV) such a design is no more suitable, since one should use very low extraction voltages heavily affecting the efficiency of the detection system. To overcome this limitation, at the very end of this doctoral project, the design for the VMI has been changed in order to include additional electrodes. Then a new setup for the GasPhase beamline has been realized (to which I have contributed with simulations, following the workshop job, pre-assembly, offline tests, final assembly for the ensuing beamtime) but not presented in this thesis. This new system, with additional electrostatic lenses, is capable of detecting low and high kinetic energy ranges by only changing the voltage settings. The low energy setting can image particles with kinetic energy up to 300 meV (with a max resolution of 10 meV) while the high energy one can collect particles up to 22 eV (with a max resolution of 1.1 eV). More recent beamtimes have demonstrated the validity also of this new flexible design, that could be also suitable for FEL application (provided that the 2D detector will be changed accordingly).
The second category of results concerns the characterization of the light sources used. In particular with the FEL setup an estimation of the FERMI pulse duration has been discussed by means of cross-correlation measurements on helium sidebands, where a pulse duration of about 100 fs has been found in agreement with the expected value. A second experiment about the pulse duration has been performed on helium doubly ionization, during the commissioning of the PADReS newly built delay line chamber for auto-correlation measurements. The pulse duration obtained was suspiciously too short. In fact an investigation performed at a later stage confirmed the newly built delay line was not properly working, in particular parts of the mechanics needed to be recommisioned after factory manteinance. However these experimental runs at FERMI could also demonstrate the value of our experimental methods for probing the main parameters of the FERMI light source (see also paper 6).
Finally, again with the aim of characterizing the incident light source, progresses done in the development of novel diamond photon beam monitors have been reported. This work has been done in collaboration with the Detector and Instrumentation group at Elettra and the XUV_lab of the University of Firenze. The results reported in this thesis have demonstrated that this kind of detectors, with a high radiation hardness, are well suited for the construction of beam position monitors (papers 12, 13, 14) with a resolution of 150 nm and as temporal structure monitors for synchrotron radiation light sources (paper 9). These investigations have recently resulted in the development of the first permanent beam monitor system based on a diamond detector operating at a bending magnet beamline at Elettra, continuously running since one year to present day (see ref. [82] and [83]). Such a system could also be useful in the development of

the new Elettra2.0 project, where an upgrade of the existing storage ring for a higher brilliance is expected.
Finally preliminary tests (not presented in this thesis work, see paper 13) have been also performed with a 50 μm diamond with the FERMI FEL source. In particular, a precision of 85 μm in the beam position encoding has been found. The reduced resolution is due to the fact that the experiment has been performed out-of-focus, with a considerable spot size dimension of about 1 mm. However intensity and position monitoring capabilities for FEL light have been demonstrated as well.

APPENDIX $\mathcal{A}$

Image inversion

In a Velocity Map Imaging spectrometer the image of photoelectrons (or in general charged particles) consists of a projection of the original 3D distribution of electrons emitted from the target onto a 2D position sensitive detector, shown in figure A.1.

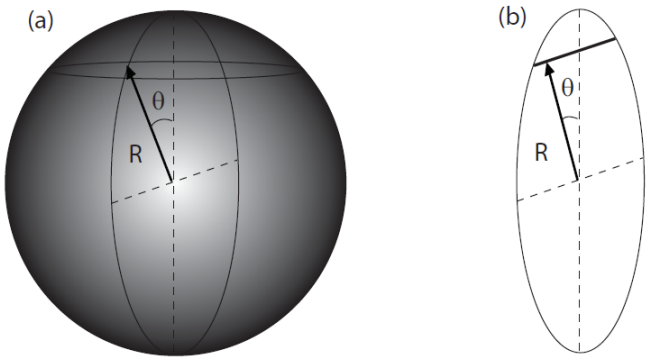

Figure A.1: *Mapping 3D distributions onto a 2D image. (a) Sphere in 3 dimensions representing the photoelectrons given by the ionisation event. The 3D sphere is mapped onto a 2D image (b) by the ion optics. (b) A 2D image of the 3D sphere expressed in polar co-ordinates. The 2D image is inverted by means of an inverse Abel transform, to recover the original distribution; the photoelectron kinetic energy is proportional to the square of the sphere radius.*

The photoelectron velocity is linearly proportional to the radius from the centre of the detector in the image plane. From this relationship the electron kinetic energy is obtained as discussed in section 3. When using an excitation pulse polarised in the image plane, orbital angular momentum information of the emitted photoelectron can be obtained from the anisotropic distribution of the image. In order to gain the photoelectron spectrum of the ionisation event the 3D sphere must be retrieved from

the 2D image that is projected onto the detector. The photoelectron angular distribution of electrons emitted in an n-photon process involving linearly polarized light, when the polarization of all photons is parallel, is completely described within the dipole approximation by the formula discussed in section 1.2.1 and reported here:

$$\frac{d\sigma}{d\Omega} = \frac{\sigma}{4\pi}\left[\sum_{j=0}^{n}(\beta_{2j}P_{2j}(\cos\theta))\right] \tag{A.1}$$

where $d\sigma/d\Omega$ is the differential photoionization cross-section, n is the numer of photons inveloved in the process, σ the total (angle-integrated) cross section, θ is the angle between the photon's polarization vector and the photoelectron's momentum direction, $P_{2j}(x)$ are the Legendre polynomials of order $l = 2j$, and β_{2j} is the asymmetry parameter.

A.1 The Method

The goal of a measurement of angular distribution of charged particles emitted from a photoionization process is to extract these asymmetry parameters. One of the fastest and most accurate approaches to the numerical solution is the use of the polar basis set expansion Abel transform (pBasex) method, introduced by Garcia et al in [84]. The inversion problem can be divided into 2 sections. These are the inverse Abel transform that must be solved and the form chosen to represent the image to be transformed. The pBasex method tries to solve the inverse Abel transform integral using a set of forward basis functions with analytical inverse Abel transforms fitted to the image. The image is effectively modelled with these basis functions that are computationally easy to inverse Abel transform. The inverse Abel transform expressed in polar coordinates for a system that is cylindrically symmetric, as is the case in velocity mapping of electrons, is:

$$\begin{aligned} T(R',\theta') &= 2\int_{|x|}^{\infty}\frac{rF(R,\theta)}{\sqrt{r^2-x^2}}dr \\ x &= R'\sin\theta' \\ r &= R\sin\theta \end{aligned} \tag{A.2}$$

The original distribution $T(R',\theta')$ and projected distribution of the 3D sphere, $F(R,\theta)$ are shown in figure A.1, where R is the radius and θ, the angle from the axis of symmetry. To solve this integral directly for a raw image is numerically challenging due to singularities, when $r = x$, instead a basis set is used to fit to the data which does not suffer from this problem. An expansion in Legendre polynomials in spherical coordinates is used as the basis set to describe the angular distributions of the photoelectrons with respect to the polarisation vector of the light. The energy distribution of the particles is then modelled using a discrete number of Gaussian functions with a width, η, which is set as the width of a pixel to give the expression:

$$F(R,\theta) = \sum_{k=0}^{k=k_{max}}\sum_{l=0}^{k=k_{max}} c_{kl}f_{kl}(R,\theta) \tag{A.3}$$

with

$$f_{kl}(R,\theta) = e^{-(R-R_k)^{2/\eta}} P_l(\cos\theta) \tag{A.4}$$

Here, θ is measured with respect to the polarisation direction (linearly polarised) of the light, P_l is the Legendre polynomial of order l and R_k represents the centre of the k-th Gaussian. R represents the ejection energy and is taken as related to the radius within the image as explained earlier. The basis function used to model the detector, as shown below, is obtained by combining equations A.3 and A.4:

$$g_{kl}(R',\theta') = 2\int_{|x|}^{\infty} \frac{r f_{kl}(R,\theta)}{\sqrt{r^2-x^2}} dr \tag{A.5}$$

This integral of the inverse Abel transform of the basis functions corresponding to the image can be expressed now as a linear expansion:

$$T(R',\theta') = \sum_k \sum_l c_{kl} g_{kl}(R',\theta') \tag{A.6}$$

From this equation the coefficients c_{kl} can be taken and substituted into equation A.3 to reconstruct the original distribution. Equation A.6 describes a case in which the distribution in the detector is continuous while an image is a discrete matrix of Cartesian pixels. For that reason the width of the Gaussian is set to be the width of a pixel and the linear expansion can be converted into terms relating to the pixels:

$$T_{ij} = \sum_k \sum_l c_{kl} g_{ij,kl} \tag{A.7}$$

where i, j are the detector radial and angular pixels respectively, and T_{ij} is obtained by converting the initial Cartesian coordinates of the detector to polar coordinates. Using Legendre polynomials has the benefit of allowing terms in the expansion to be eliminated depending on the distribution expected from the photoionisation event. When the light is linearly polarised the odd Legendre terms are eliminated. The more general rule for number of terms in the polynomial, l_{max}, is $l_{max} = 2n$, where n is the number of photons.

APPENDIX B

SIMION® simulation software

SIMION® is a software package used primarily to calculate electric fields, when given a configuration of electrodes with voltages, and calculate trajectories of charged particles in those fields, and given particle initial conditions, including optional RF, magnetic field, and collisional effects. In this, SIMION provides extensive supporting functionality in defining system geometry and conditions, recording and visualizing results, and extending the simulation capabilities with user programming [28]. A SIMION geometry file (GEM) defines electrode geometries, is a text file and has the file name extension '.GEM'. SIMION can convert a GEM file to a Potential Array (PA) file. A PA is a 2D or 3D rectangular grid (sometimes called a 'mesh') of points in space. Its purpose is to store electrode geometries and/or potentials. Each point defines a potential (electrostatic or scalar magnetic potential) and/or a flag marking the point as an electrode or non-electrode point [28]. SIMION's methods are fairly direct via finite difference methods (optimized over-relaxation and multimesh methods) and Runge-Kutta for solving the required partial differential equations (PDEs), particularly the Laplace Equation, and ordinary differential equations (ODEs) respectively [28].

B.1 Potential optimization example

Once the geometry .GEM (text) file has been created and converted into a PA (in this first example the VMI and PSD detector geometry has been created) one can assign potentials to the electrodes, calculate and visualize the potential energy surfaces, calculate and visualize charged particles trajectories (to "fly" particles, in SIMION terminology). When dealing with a VMI spectrometer one seeks to find the potentials such that VMI conditions hold (particles with the same kinetic energy momentum arrive in the same spatial region of the PSD even if the particle' source dimension is not a point but an

extended volume) To do so let us first define the geometry and the frame of reference as in figure B.1.

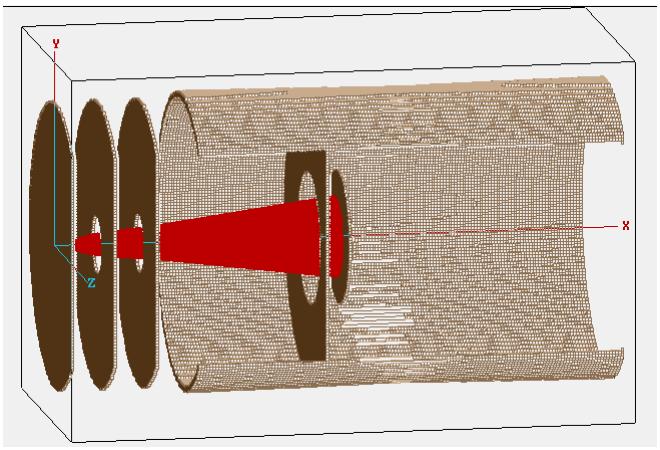

Figure B.1: *Geometry file of the electrodes for the VMI spectrometer and coordinate system used in SIMION.*

Where the X-axis is the detector axis, the Z-axis is the light propagation axis, the Z and Y define the plane of the PSD where the image of the arriving particles is collected. Usally in order to check the VMI conditions a source volume of 3 mm in the Z direction, and 0.5 mm in the Y and X directions is set. Then the potentials are set in the 'Fast Adjust' SIMION's panel for each electrodes, and clicking on the Potential Energy 'PE' panel it is possible to view the potential energy surfaces and equipotential lines (in blue in figure B.2).

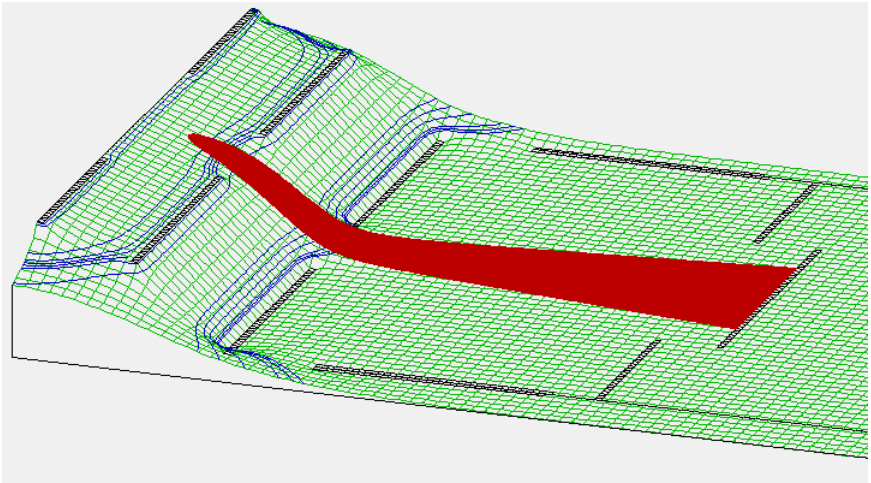

Figure B.2: *Potential Energy surfaces in SIMION.*

Then 3 groups of particles (blue, red and green in fig.B.3) with the same kinetic energy but different directions are flown (each group with 3 particles spaced along the Z-axis by 1 mm): In a) potentials are set so that VMI conditions holds and the particles are indeed focussed. In b) VMI conditions do not hold and indeed the particles are spread out at the detector plane.

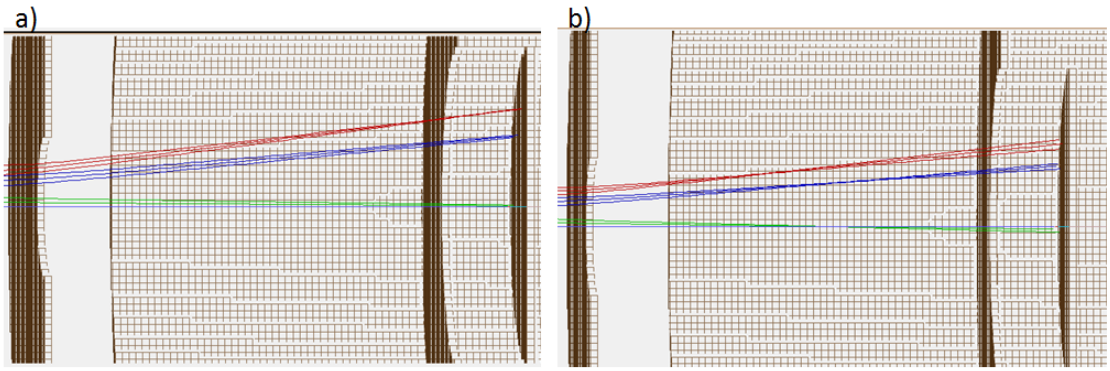

Figure B.3: *Particle's trajectory for two different extraction voltages.In a) potentials optimized for VMI conditions in b) potentials non optimized.*

B.2 Energy calibration simulation

SIMION has been also used, once the potential optimization is done, to estabilish what maximum kinetic energy of the particles (i.e. electrons) is possible to collect with such a detector, for a fixed potential configuration. Assuming a certain MCP effective diameter, particle with incresing kinetic energy are flown until they fall off the detector. A typical simulation is reported in fig.B.4, with 100000 electrons with 35 eV of kinetic energy having an uniform direction distribution. The data are binned into a 200×200 pixel image with a side lenght of 40 mm.

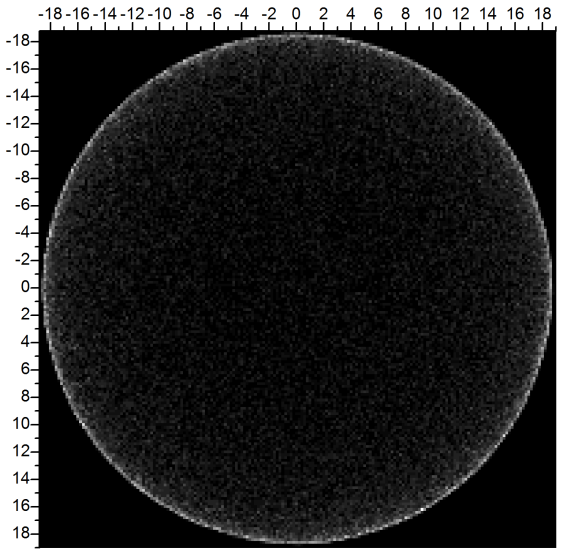

Figure B.4: *Typical particle's trajectory simulation. 100000 electrons with 35 eV of KE randomly distributed.*

In addition, in order to have an idea of the energy calibration, a simulation has been performed (voltage settings: $V_{extractor} = -1472V$ and $V_{repeller} = -2000V$) by flying 12 groups of electrons (for a total of 420000 electrons). With the aim of simulating the

measurement that has been performed to extract the real energy calibration (as reported in 5.1.1), the 12 groups of electrons are flown with kinetic energies of: 0.2 eV, 1.5 eV, 3.5 eV, 6 eV, 7.3 eV, 8.5 eV, 9.3 eV, 13.5, 14.3 eV, 18.5 eV, 19.3 eV and 24.3 eV respectively. The results have been binned into a 200×200 pixel image and reported in figure B.5 a), while the pBasex (see section A) inverted image is reported in figure B.5 b).

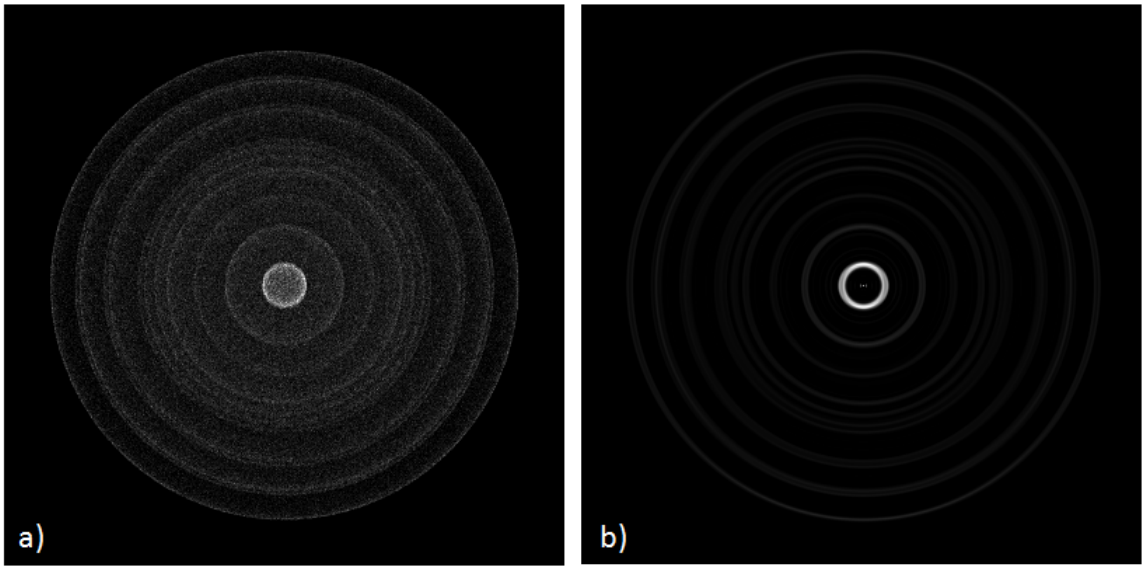

Figure B.5: *In a) VMI image simulation for photoelectrons with 0.2 eV, 1.5 eV, 3.5 eV, 6 eV, 7.3 eV, 8.5 eV, 9.3 eV, 13.5, 14.3 eV, 18.5 eV, 19.3 eV and 24.3 eV kinetic energy. In b) Transformed image with pBasex inversion software.*

After the image inversion, it is then possible to analyze the PES as reported in in figure B.6 a). The peak centers are plotted on the x-axis in the graph of figure B.6 b) while on the y-axis the nominal kinetic energies have been reported.

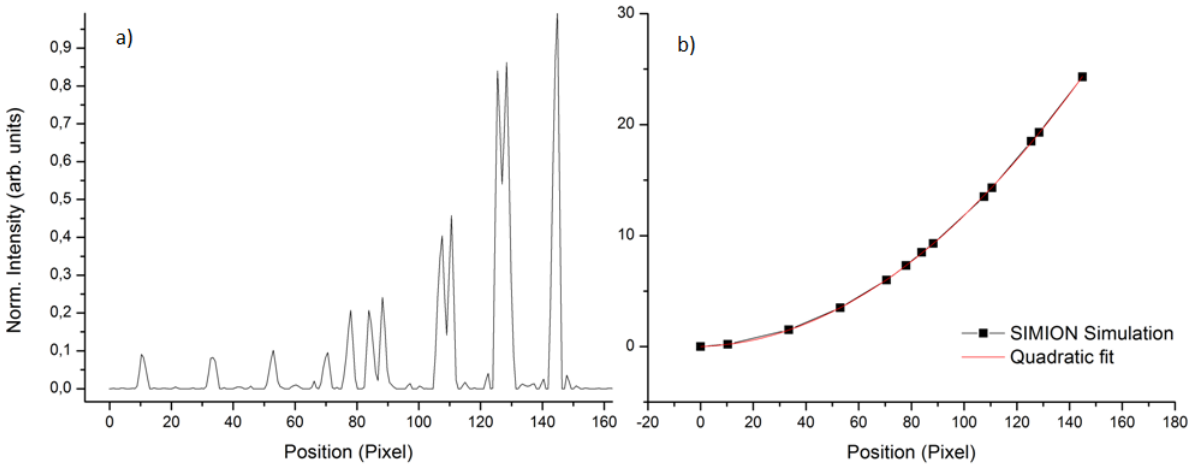

Figure B.6: *In a) PES after pBasex inversion. b) Energy calibration simulation.*

The curve can be fitted with a 2^{nd} order polynomial (red curve in figure B.6 b)), as expected : $KE = A + Bx + Cx^2$, here x represents the pixel position of the peak center in the PES obtained with pBasex. The fitted curve gave the following result for the coefficients: $A = 0, B = 0.72 \times 10^{-2}, C = 1.11 \times 10^{-3}$ with an agreement of 99.9% (Adj. R-square). The goodness of the fit can be evaluated by rescaling the x-axis of fig. B.6 a) according to the fitting parameters just calculated. The rescaled graph is reported in B.7.

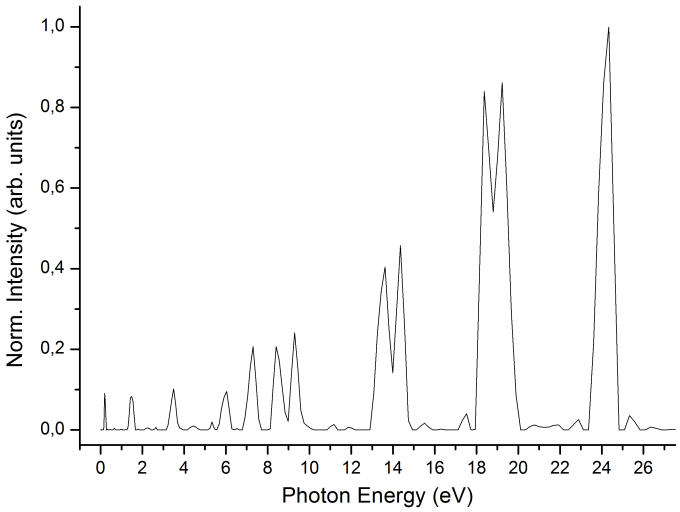

Figure B.7: *Energy calibrated PES of fig. B.6.*

The resolutions obtained, by fitting the outer and inner peaks (24.3 eV and 1.5 eV respectively) with a gaussian curve and evaluating the FWHM (ΔE), are: for the outer peak ΔE= 730 meV and thus a resolution of $\Delta E/E$= 3%, while for the inner peak a ΔE= 260 meV and thus a resolution of $\Delta E/E$= 7%.

APPENDIX C

Helium multiphoton double ionization

C.1 Theoretical Background

In the FEL intensity regime of $\sim 10^{14}$ W/cm^2 and at the photon energy of 52.24 eV (23.73 nm), not only the double two photon ionization process, but also the sequential three photon (S3P) ionization channel contributes to the total He^{2+} ion yield. The excitation scheme is shown in figure C.1: 1) and 2) denote the two processes (channels) which lead to doubly ionized He species at this wavelength. Those processes are described by:

1. He $1s^2 + 2h\nu \rightarrow He^{2+} + 2e^-$

2. He $1s^2 + h\nu \rightarrow He^+\ 1s + e^-$
   $He^+\ 1s + h\nu \rightarrow He^+\ 5p$
   $He^+\ 5p + h\nu \rightarrow He^{2+} + e^-$

The first process (1) is the direct two photon two electron process (D2P), while the second process (2) is the sequential three photon process (S3P) through the $5p$ state of He^+ which is a very long lived state (of the order of tens of ps) compared to the pulse duration.
Since the photon energy is resonant with the $1s \rightarrow 5p$ transition in He^+, the non-resonant two-photon ionization of He^+ is not considered. In fact, by using the hydrogenic scaling laws [85] for the cross-section considering also the energy scaling:

$$\hat{\sigma}_N(\mu, Z, \omega) = \left(\frac{\mu}{m_e}\right)^{-3N+1} Z^{-4N+2}\, \hat{\sigma}_N\left(m_e, Z = 1, \frac{\omega}{(\mu/m_e)Z^2}\right) \tag{C.1}$$

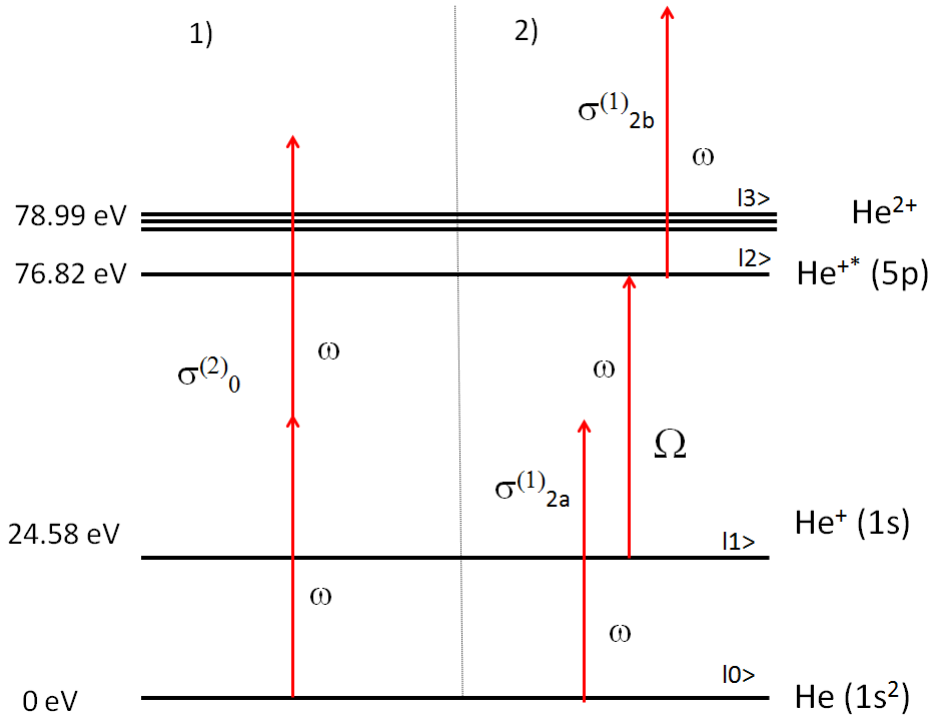

Figure C.1: *Excitation scheme for the photon energy of 52.24 eV: 1) the direct two photon (D2P) double ionization and 2) the sequential three photon (S3P) double ionization.*

The cross section for the non-resonant process is found to be $\sigma = 5.4 \times 10^{-54}$ cm^{4}s and its contribution to the total ion yield calculated latter is expected to be of the order of 0.6 %, thus negligible in comparison with the resonant contribution. The interaction of an atom with a classical monochromatic field can be described by the following Hamiltonian operator [16]:

$$\mathcal{H} = \mathcal{H}^A + \mathcal{V}^{AF}(t), \tag{C.2}$$

where $\mathcal{H}^A$ is the atomic term and the $\mathcal{V}^{AF}(t)$ is the interaction term:

$$\mathcal{H}^A = \sum_i E_i |i\rangle\langle i|, \tag{C.3}$$

$$\mathcal{V}^{AF} = -\vec{d} \cdot \vec{E}(t) = -d\, E(t). \tag{C.4}$$

The energies of the atomic eigenstates $|i\rangle$ are denoted by $E_i = \hbar\omega_i$, and $d = \vec{D} \cdot \hat{e}$ is the electric dipole operator which describes the interaction of the atom with linearly polarized light with polarization $\hat{e}$. The amplitude of the electric field is:

$$E(t) = \frac{\xi}{2} e^{-i\omega t} + \frac{\xi^*}{2} e^{+i\omega t} = |\xi| \cos(\omega t - \varphi). \tag{C.5}$$

The time evolution of the system $|\Psi(t)\rangle$ is described by the Schrödinger equation:

$$\frac{\partial |\Psi(t)\rangle}{\partial t} = -\frac{i}{\hbar} \mathcal{H} |\Psi(t)\rangle. \tag{C.6}$$

Using Eq. (C.6), we can also take into account the spontaneous decay of the states (through their decay widths Γ_i) if the energies E_i are replaced with $E_i - i\Gamma_i/2$. Thus, the FEL-induced coupling between a pair of selected states is represented by the following matrix:

$$\mathcal{H} = \begin{pmatrix} E_1 - i\frac{\Gamma_1}{2} & \mathcal{V}_{12}^{AF} \\ \mathcal{V}_{21}^{AF} & E_2 - i\frac{\Gamma_2}{2} \end{pmatrix}. \tag{C.7}$$

C.1.1 Process 1: Direct Two Photon process (D2P)

The creation of He^{2+} due to the D2P process can be described by the following set of rate equations:

$$\frac{\partial \rho_{00}(t)}{\partial t} = -\Gamma_0 \rho_{00}(t), \tag{C.8}$$

$$\frac{\partial \rho_{33}(t)}{\partial t} = \Gamma_0 \rho_{00}(t), \tag{C.9}$$

where $N_0 \equiv \rho_{00}(t)$ and $N_3 \equiv \rho_{33}(t)$ represent the time-dependent population of the ground state He atoms and the population of He^{2+} ions, respectively. The two-photon ionization rate is:

$$\Gamma_0 = \sigma_0^{(2)}\, \Phi^2, \tag{C.10}$$

where $\sigma_0^{(2)}$ is the (direct) two-photon double ionization (D2P) cross section of the ground state He atom, $\Phi(t) = I(t)/(\hbar\omega)$ is the photon flux (in $\mathrm{cm^{-2}s^{-1}}$), and $I(t)$ is the intensity (in $\mathrm{W\,cm^{-2}}$). Since we assume that at the beginning (i.e., at $t = 0$) all the atoms are in the ground state, the initial conditions are: $\rho_{00}(-\infty) = 1$ and $\rho_{33}(-\infty) = 0$, where the limit $t \to -\infty$ corresponds to times long before the arrival of the light pulse(s) to the interaction region.

C.1.2 Process 2: Sequential Three Photon process (S3P)

For a rigorous treatment of the S3P process and in order to correctly take into account the Rabi oscillations between the two states of He^+, it is convenient to use the density matrix formalism. Denoting the He^+ $1s$ state with $|1\rangle$ and the He^+ $5p$ state with $|2\rangle$, the time-dependent wave function of the system can be expressed as:

$$|\Psi(t)\rangle = \sum_{i=1}^{2} c_i(t)|i\rangle, \tag{C.11}$$

where $c_i(t)$ are the time-dependent amplitudes of the atomic eigenstates $|i\rangle$. In the case of a "pure" ensemble [16], the density operator ρ is defined as:

$$\rho = |\Psi(t)\rangle\langle\Psi(t)|, \tag{C.12}$$

and using the expansion for $|\Psi(t)\rangle$ defined in Eq. (C.11), follows that:

$$\rho = \sum_n \sum_m c_n c_m^* |n\rangle\langle m| = \sum_{n,m} \rho_{nm} |n\rangle\langle m|, \tag{C.13}$$

where $\rho_{nm} = \langle n|\rho|m\rangle = c_n c_m^*$ are the matrix elements of the density operator. The diagonal elements $\rho_{nn}(t)$, also called *populations*, represent the probability of finding

the system in the states $|n\rangle$ at time t. The off-diagonal matrix elements are called *coherences* because they depend on the phase difference of c_n and c_m. The time evolution of the system [see Eq. (C.6)] in terms of the density operator is then described by the following equation:

$$\frac{\partial \rho}{\partial t} = -\frac{i}{\hbar}(\mathcal{H}\rho - \rho\mathcal{H}^\dagger), \tag{C.14}$$

or in matrix form:

$$\frac{\partial \rho_{nm}}{\partial t} = -\frac{i}{\hbar}\sum_a (\mathcal{H}_{na}\rho_{am} - \rho_{na}\mathcal{H}^\dagger_{am}) \tag{C.15}$$

$$= -\frac{i}{\hbar}\sum_a (\mathcal{H}_{na}\rho_{am} - \rho_{na}\mathcal{H}^*_{ma}). \tag{C.16}$$

Denoting the decay width of the upper state by Γ_2 and using Eq. (C.15), one obtains the following set of equations:

$$\frac{\partial \rho_{11}(t)}{\partial t} = -i\frac{\Omega}{2}\rho_{21} + i\frac{\Omega^*}{2}\rho^*_{21}, \tag{C.17}$$

$$\frac{\partial \rho_{22}(t)}{\partial t} = -\Gamma_2\rho_{22} - i\frac{\Omega^*}{2}\rho^*_{21} + i\frac{\Omega}{2}\rho_{21}, \tag{C.18}$$

$$\frac{\partial \rho_{21}(t)}{\partial t} = \left(i\Delta - \frac{\Gamma_2}{2}\right)\rho_{21} - i\frac{\Omega^*}{2}\rho_{22} + i\frac{\Omega}{2}\rho_{11}. \tag{C.19}$$

Used $\Omega = \Omega_{21} = d_{5p\leftarrow 1s}\,E(t)$ to denote the Rabi frequency associated with the He^+ $1s \rightarrow 5p$ transition and introduced the detuning $\Delta = \omega - (E_2 - E_1)$, where ω is the photon energy. Contrary to the simple two-state system described by these equations, the complete system under consideration is not closed. Simultaneously with the driving described by Eqs. (C.17)–(C.18), excitations due to the D2P process also take place. Thus modifing Eqs. (C.17)–(C.18) to also account for the D2P process:

$$|0\rangle : \frac{\partial \rho_{00}(t)}{\partial t} = -(\Gamma_0 + \Gamma_1)\rho_{00}(t), \tag{C.20}$$

$$|1\rangle : \frac{\partial \rho_{11}(t)}{\partial t} = \Gamma_1\rho_{00}(t) - i\frac{\Omega}{2}\rho_{21} + i\frac{\Omega^*}{2}\rho^*_{21}, \tag{C.21}$$

$$|2\rangle : \frac{\partial \rho_{22}(t)}{\partial t} = -\Gamma_3\rho_{22}(t) - i\frac{\Omega^*}{2}\rho^*_{21} + i\frac{\Omega}{2}\rho_{21}, \tag{C.22}$$

$$\frac{\partial \rho_{21}(t)}{\partial t} = (i\Delta - \frac{\Gamma_3}{2})\rho_{21} - i\frac{\Omega^*}{2}\rho^*_{22} + i\frac{\Omega}{2}\rho_{11}, \tag{C.23}$$

$$|3\rangle : \frac{\partial \rho_{33}(t)}{\partial t} = \Gamma_0\rho_{00}(t) + \Gamma_3\rho_{22}(t). \tag{C.24}$$

Again used Γ_0 for the D2P rate, Ω for the Rabi frequency, and Δ for the detuning. The other quantities are: (i) $\Gamma_1 = \sigma^{(1)}_{2a}\Phi$ the decay rate of the ground state due to one-photon one-electron ionization process; (ii) $\Gamma_3 = \sigma^{(1)}_{2b}\Phi$ the He^+ $5p \rightarrow He^{2+}$ ionization rate. The single-photon single-electron ionization cross sections of the ground state He atom and the ground state He^+ ion are denoted with $\sigma^{(1)}_{2a}$ and $\sigma^{(1)}_{2b}$, respectively. The initial conditions are: $\rho_{00}(-\infty) = 1$, $\rho_{11}(-\infty) = \rho_{22}(-\infty) = \rho_{33}(-\infty) = \rho_{21}(-\infty) = 0$.

C.1.3 Photon flux

In the case of a single incident pulse (i.e., when the delay line is not used) the photon flux may be written as:

$$\Phi(t) = \Phi_0\, e^{-4\ln 2\,(t/T)^2}, \tag{C.25}$$

where it is assumed that the temporal profile of the pulse is Gaussian. The peak amplitude of the flux is defined as $\Phi_0 = I_0/(\hbar\omega) \equiv N/(S\,T)$, I_0 is the peak intensity, N is the number of photons incident on the focal spot with the surface area equal to S, and T is the FWHM of the pulse duration. The number of photons N is obtained from the measured total energy $E_{\rm tot}$ (in units of μJ) using $N \approx E_{\rm tot}/(1.2\,\hbar\omega)$, which takes into account the numerical factors due to the Gaussian shape. Taking into account the 50% beamline transmission, the spot size measured by a wavefront sensor was $S = 15 \times 15$ μm^2. Setting the pulse duration to $T = 50$ fs, we obtain the peak amplitude of the flux:

$$\Phi_0 = 1.3 \times 10^{31}\text{cm}^{-2}\text{s}^{-1}. \tag{C.26}$$

This corresponds to the peak intensity:

$$I_0 = 1.3 \times 10^{14}\text{W/cm}^2. \tag{C.27}$$

The electric field in Hartree atomic units is given by

$$E(t) = \sqrt{8\pi\alpha\omega\,\Phi(t)}, \tag{C.28}$$

where α is the fine structure constant, and both $\Phi(t)$ and ω should be given in a.u. Note that the atomic unit of energy is

$$E_{\rm a.u.} = E_H \approx 27.2\ \text{eV} \tag{C.29}$$

and the atomic unit of flux is

$$\Phi_{\rm a.u.} = \frac{1}{a_0^2\, t_{\rm a.u.}} \approx 1.48 \times 10^{33}\ \text{cm}^{-2}\text{s}^{-1}, \tag{C.30}$$

where a_0 is the Bohr radius and $t_{\rm a.u.} = \hbar/E_H \approx 2.4189 \times 10^{-17}$ s is the atomic unit of time.

It is possible now to generalize these results to the case where the delay line is used. Assuming that the total electric field may be written as:

$$E(t;\tau) = E_1(t) + E_2(t;\tau) \tag{C.31}$$

$$= \frac{\xi_1(t)}{2} e^{-i\omega t} + \frac{\xi_2(t-\tau)}{2} e^{-i\omega(t-\tau)} + \text{c.c.}, \tag{C.32}$$

where $E_1(t)$ describes the part of the field at time t and $E_2(t,\tau)$ the part which is delayed by time τ. The time-dependent amplitudes $\xi_1(t)$ and $\xi_2(t)$ describe the envelopes of the two fields and c.c. stands for complex conjugation. In the case of the D2P process, we are interested in absorption of two photons, so only the terms associated with the positive frequency in (C.32) will be considered:

$$E(t;\tau) = \frac{\xi_1(t)}{2} e^{-i\omega t} + \frac{\xi_2(t-\tau)}{2} e^{-i\omega(t-\tau)}. \tag{C.33}$$

Taking the envelopes $\xi_i(t)$ to be Gaussian

$$\xi_1(t) = \xi_{10}\, e^{-t^2/(2T^2)}, \tag{C.34}$$

$$\xi_2(t-\tau) = \xi_{20}\, e^{-(t-\tau)^2/(2T^2)}. \tag{C.35}$$

Here ξ_{10} and ξ_{20} are the time-independent peak amplitudes. Is assumed that $\xi_1(t)$ and $\xi_2(t)$ do not vary appreciably on the time scale of the period of oscillations of the field, i.e., we assume that $T \gg 2\pi/\omega$.

The quantity we are interested in is the two-photon rate, e.g., the rate Γ_0 introduced in (C.10), which describes a second order process, and is thus proportional to the square of the flux. Neglecting other processes for the moment, the corresponding ion yield $Y^{(2)}$ will thus be proportional to:

$$Y^{(2)} \propto \sigma^{(2)} \int_{-\infty}^{\infty} |E(t;\tau)|^4\, dt, \tag{C.36}$$

where the two-photon ionization cross section $\sigma^{(2)}$ is time-independent. Due to the finite temporal resolution of the delay line (e.g., due to mechanical constraints), the measured yield Y_m is proportional to:

$$Y_m^{(2)} = \frac{1}{\sqrt{2\pi}\, s} \int_{-\infty}^{\infty} d\tau\, Y^{(2)}(\tau)\, e^{-(\tau_0-\tau)^2/(2s^2)} \tag{C.37}$$

$$= \frac{\sigma^{(2)}}{\sqrt{2\pi}\, s} \int_{-\infty}^{\infty} dt \int_{-\infty}^{\infty} d\tau |E(t;\tau)|^4 \times e^{-(\tau_0-\tau)^2/(2s^2)}, \tag{C.38}$$

where a Gaussian response function has been assumed, where the width s is directly proportional to the delay line resolution. The nominal delay has been denoted by τ_0. In this particular case, the resolution of the delay line (~ 0.3 fs) is large in comparison with the period of the oscillations, so $s \gg 2\pi/\omega$. This means that the oscillations of the field will be smeared out because of the finite resolution. Since this is the case and since the envelopes vary slowly as well, $|E(t;\tau)|^4$ may be replaced by its average $|E_{\text{avg}}(t;\tau)|^4$ where the harmonic factors are replaced by their averages over τ. Formally, this is achieved by evaluating the inner integral in (C.38) by assuming the envelopes to be constant, i.e., $\xi_2(t-\tau) \approx \xi_2(t-\tau_0)$, and taking the limit $s^2\omega^2 \to \infty$:[1]

$$|E_{\text{avg}}(t;\tau_0)|^4 = \frac{1}{16}\Big\{|\xi_1(t)|^4 + |\xi_2(t-\tau_0)|^4 + 4|\xi_1(t)|^2|\xi_2(t-\tau_0)|^2\Big\}. \tag{C.39}$$

The measured yield is thus proportional to:

$$Y_m^{(2)} = \frac{(2\pi)^{3/2}\alpha^2\omega^2\sigma^{(2)}}{s} \int_{-\infty}^{\infty} dt \left\{\Phi_1^2(t) + \Phi_2^2(t-\tau) + 4\Phi_1(t)\Phi_2(t-\tau)\right\}. \tag{C.40}$$

[1] Note that this implies that $T \gg s$.

The same procedure can be used in the case of a single-photon process, where the yield is seen to be proportional to

$$Y_m^{(1)} \propto \sigma^{(1)} \int_{-\infty}^{\infty} \{\Phi_1(t) + \Phi_2(t-\tau)\}. \tag{C.41}$$

C.2 Simulation Results and Discussion

The D2P cross-section and the single-photon one-electron cross section of the ground state He atom can be found in Ref. [86]: $\sigma_0^{(2)} = 2.0 \times 10^{-52}$ cm^{4}s and $\sigma_{2a}^{(1)} = 1.9 \times 10^{-18}$ cm^2. By means of the LANL web interface [87] we get the He^+ $5p$ ionization cross section: $\sigma_{2b}^{(1)} = 2.6 \times 10^{-21}$ cm^2. The dipole matrix element has been calculated $d_{21} = d_{5p \leftarrow 1s}$ using the $Z = 2$ (real) hydrogenic wave functions: $d_{12} = d_{21} = 0.060$ a.u.

By varying the FEL intensity from 10^8 W/cm^2 up to 10^{16} W/cm^2, we have calculated the dependence of the He^{2+} yield on the peak intensity shown in Fig. C.2.

Figure C.3 shows a detail from Fig. C.2. To be noticed that at intensities of about

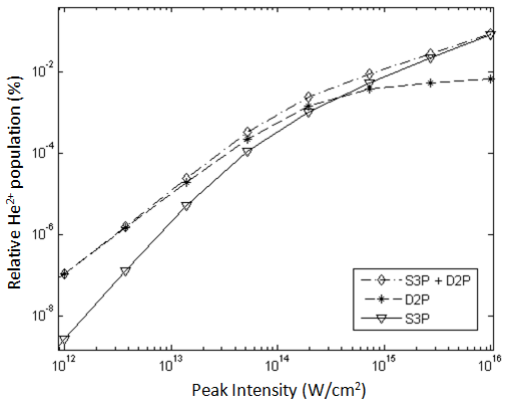

Figure C.2: *The He^{2+} yield dependence on the FEL peak intensity for the D2P (crosses) and S3P (triangles) processes seperately and combined (diamonds).*

10^{14} W/cm^2, the D2P is the dominating process accounting for approximately 63% of the total He^{2+} signal. In order to take into account the effects of the beam focusing, a Gaussian spatial profile has been assumed. The dependence of the peak intensity I_0 (which now depends on the spatial coordinates inside the interaction volume) is:

$$I_0(r,z) = I_f \, \exp\Big\{ -2\Big(\frac{r}{w(z)}\Big)^2 \Big\}, \tag{C.42}$$

where r and z are coordinates perpendicular and parallel to the beam direction, respectively, $w(z)$ is the beam waist and I_f is the maximum intensity, i.e., the intensity in the focus. The dependence of $w(z)$ is:

$$w(z) = w_0[1 + (z/z_0)^2]^{1/2}, \tag{C.43}$$

where w_0 is related to the FWHM (the spatial extent of the beam in the focus)[2] and z_0 is called the Rayleigh range defined as $z_0 = \pi w_0^2/\lambda$. In the present case, for $\lambda =$

[2]The relation is: $w_0 = 0.84932 \times$ FWHM.

23.73 nm, the FEL spot size of 15 μm, and taking the dimension of the interaction volume to be of about 1 mm in the z direction, $z \ll z_0$ for any point of the interaction volume. As a consequence, $w(z) \approx w(0)$ may be assumed to hold, and the integration over z becomes trivial. Looking at fig. C.2, the volume integration should result in an autocorrelation peak (due to the D2P process) which is even more pronounced (it is higher in comparison with the background due to the S3P process) than the peak calculated without taking care of the volume effects: the relative contribution of the D2P process to the total yield is higher when the peak intensity is lower. Indeed, our calculations have shown that upon volume integration, a relative increase of about 1.5% of the D2P peak occurs. Considering the volume integration, the D2P process accounts for 64.5%, while the S3P process accounts for 35.5% of the total He^{2+} signal.

Up to now monochromatic pulses has been considered, i.e., pulses with a well defined carrier frequency ω. Nevertheless, the results are valid also for realistic FEL pulses with a finite bandwidth. In fact, by using the density matrix formalism [see equations (C.21), (C.22), and (C.23)], the signal broadening due to the Fourier width of the pulse has been already taken into account. The effect of a non-monochromatic beam must be considered explicitly only for the non-resonant processes, so for the D2P process and the single-photon single ionization. For those processes, the corresponding cross sections are seen to be smooth functions of the photon energy [86, 88], and the finite bandwidth (i.e., the convolution with the spectral function) does not affect the width of the temporal correlation signal. By changing the time delay between the two pulses in the range between -300 fs and 300 fs and calculating the He^{2+} yield, the plot shown in Fig. C.4 has been obtained. Fitting those results with a Gaussian distribution an agreement of 99.8 % (Adjusted R^2) has been found. By changing the

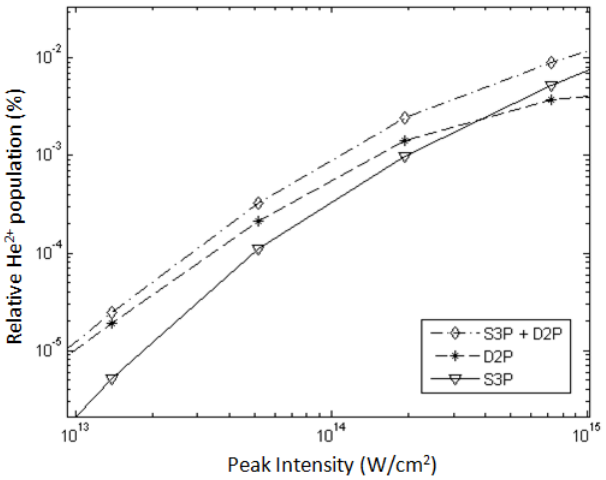

Figure C.3: *The dependence of the He^{2+} signal on the FEL intensity (single pulse) for the D2P and S3P processes.*

assumed temporal width (FWHM) of the FEL pulse from 50 fs to 30 fs, 80 fs, and 100 fs, the autocorrelation signal width (FWHM) has been simulated and reported in figure C.5. The width of the calculated autocorrelation signal due to both processes (D2P and S3P) differs from the width due to the D2P process alone by about 4%. This difference is negligible in comparison with the experimental uncertainties (intensity fluctuations,

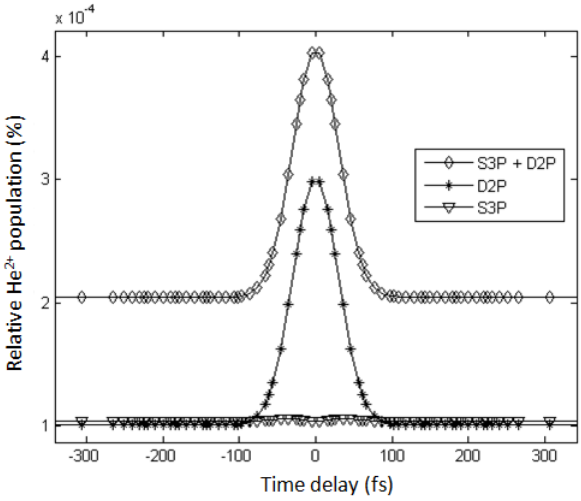

Figure C.4: *The He^{2+} yield signal for the D2P and S3P processes dependence on the time delay between the two FEL pulses with a peak intensity of 10^{14} W/cm^2. D2P (crosses) and S3P (triangles) processes, D2P + S3P (diamonds). Also a Gaussian fit curve is shown.*

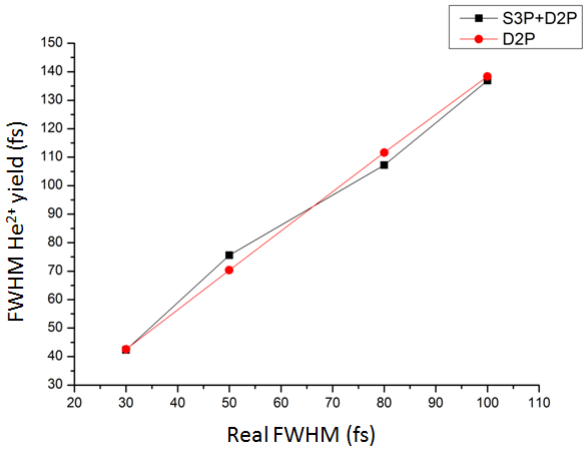

Figure C.5: *The FWHM autocorrelation signal for the D2P + S3P and for the pure D2P processes versus FEL pulses (5×10^{13} W/cm^2 each) with different nominal FWHM width (30 fs, 50 fs, 80 fs, and 100 fs). D2P + S3P (black squares) and D2P (empty circles).*

spot size uncertainty, etc.). By dividing the widths of the signals obtained in this simulation by a factor of $\sqrt{2}$, we obtain an estimation of the real pulse length as expected by the D2P process alone. In conclusion, the contribution of the S3P process results in an increase of the baseline level, as can be inferred from figure C.4. The effect on the width of autocorrelation signal on the He^{2+} yield is about 4% (see C.5) and is thus negligible because for sure lower than the experimental errors. The fact that the correlation signal is still clearly detectable despite the presence of the S3P process is due to the fact that the lifetime of the resonant process is much longer than the pulse duration, resulting primarily in a baseline level increase.

List of Symbols and Acronyms

α	fine structure constant
γ	Lorentz's factor: $\gamma = \frac{1}{\sqrt{1-(\frac{v}{c})^2}}$.
λ	wavelenght
ν	radiation frequency
ω_c	Critical frequency parameter in storage rings
$\Phi(\mathbf{r}, t)$	scalar potential of the field
σ_{if}	photoionization cross-section for transition from initial state i to final state f
$\mathbf{E}(t)$	Electric Field
ε_0	dielectric constant
$\vec{\beta}$	speed relative to the light speed in vacuum c: $\vec{\beta} = v/c$
$\vec{B}$	magnetic field
$A(\mathbf{r}, t)$	vector potential of the field
a_0	Bohr radius
c	speed of light in vacuum
h	Planck constant
H^A	Atomic term of the Hamiltonian
J	total angular momentum: J=L+S
k	wave vector
$L - S$	spin-orbit coupling
m_e	electron mass

V^{AF} Interaction term of the Hamiltonian

AD Angular Distribution

ADC analog-to-digital converter

CAI Collective AutoIonization

CVD Chemical Vapor Deposited

D2P Direct Two Photon

DPI Direct PhotoIonization

eBPM electron Beam Position Monitor

FEL Free Electron Laser

FOFB Fast Orbit FeedBack

FWHM Full Width Half Maximum

HA Hemispherical Analyzer

HGHG High-Gain Harmonic-Generation

ICD Interatomic Coulombic Decay process

IP Ionization Potential

K Undulator strength parameter

KB Kirkpatrick-Baez Mirror pairs

KE Kinetic Energy

LDM Low density Matter beamline

MBES Magnetic Bottle Electron Spectrometer

MCP Micro Channel Plate

NIR Near Infra-Red

NR2P Non-Resonant Two Photon

pBPM photon Beam Position Monitor

PEPICO PhotoElectron-PhotoIon COincidence spectroscopy

PEPIPICO PhotoElectron-PhotoIon-PhotoIon COincidence spectroscopy

PES Photoelectron Energy Spectrum

PSD Position Sensitive Detector

R2PI Resonant Two PhotoIonization

RF Radio Frequency

S3P Sequential Three Photon

SASE Self Amplified Spontaneous Emission

SR Synchrotron Radiation

TDC Time-to-digital converter

TOF Time-of-Flight

UV UltraViolet

VMI Velocity Map Imaging

XUV Extreme UltraViolet

YAG Yttrium Aluminium Garnet

Bibliography

[1] C. R. Brundle and A. D. Baker (Editors). *Electron spectroscopy: Theory, techniques and applications*. Academic Press London, 1982.

[2] C. J. Joachain B. H. Bransden. *Physics of Atoms and Molecules*. 2nd Edition. Prentice Hall, Harlow, England, 2003.

[3] Christopher J. Foot. *Atomic Physics*. Oxford University Press, Oxford, 2005.

[4] Alonso J. A. *Structure and Properties of Atomic Nanoclusters*. Imperial College Press, U.S., 2012.

[5] A. W. Castleman Jr. and R. G. Keesee. Clusters: bridging the gas and condensed phases. *Accounts of Chemical Research*, 19(12):413–419, 1986.

[6] The National Institute of Standards and Technology (NIST). *NIST Atomic Spectra Database*, 2014. http://www.nist.gov/pml/data/asd.cfm.

[7] Johnston R. L. *Atomic and Molecular Clusters*. CRC Press, 2002.

[8] M.L. Klein. *Inert Gases*. Springer-Verlag, Berlin Heidelberg, 1984.

[9] R.A. Aziz, V.P.S. Nain, J.S. Carley, W.L. Taylor, G.T. McConville. An accurate intermolecular potential for helium. *Journal of Chemical Physics*, 70:4330, 1979.

[10] R.A. Aziz, W. J. Meath, and A. R. Allnatt. On the Ne-Ne potential-energy curve and related properties. *Chemical Physics*, 78:295–309, 1983.

[11] R.A. Aziz, H.H. Chen. An accurate intermolecular potential for argon. *Journal of Chemical Physics*, 67:5719, 1977.

[12] R.A. Aziz. An improved potential for krypton. *Molecular Physics*, 38:177, 1979.

[13] J. A. Barker, M.L. Klein and M.V. Bobetic. Lattice dynamics with three-body forces: solid Xe and Kr. *IBM Journal of Research and Development*, 20:222, 1976.

[14] Doctoral Thesis by Marcus Lundwall. Rare-gas clusters studied by electron spectroscopy. *Digital Comprehensive Summaries of Uppsala Dissertations from the Faculty of Science and Technology*, 260, 2007.

[15] C.C. Gerry, P.L. Knight. *Introductory Quantum Optics*. Cambridge University Press, 2005.

[16] P. Lambropoulos, D. Petrosyan. *Fundamentals of Quantum Optics and Quantum Information*. Springer, 2007.

[17] G. Grynberg C. Cohen-Tannoudji, J. Dupont-Roc. *Atom-Photon Interactions*. Wiley-VCH Verlag GrnbH & Co. KGaA, 2004.

[18] D. A. Shirley U. Becker. *VUV and Soft X-ray Photoionization*. Plenum Press, New York, 1996.

[19] W. Demtröder. *Atoms, Molecules and Photons: An Introduction to Atomic-, Molecular- and Quantum-physics; with 43 Tables*. Advanced texts in physics. Springer, 2006.

[20] Master's Thesis by S. Thorin. Design and construction of a velocity map imaging spectrometer. *Lund Reports on Atomic Physics*, 327, 2004.

[21] Elettra Sincrotrone Trieste. *Elettra official website*, 2014. https://www.elettra.trieste.it/it/lightsources/elettra/sorgente-elettra.html.

[22] The Center for X-Ray Optics. *CXRO Synchrotron bend magnet spectrum calculator*, 2014. http://henke.lbl.gov/optical_constants/bend2.html.

[23] F. Ciocci, G. Dattoli, A. Torre, A. Renieri. *Insertion Devices for Synchrotron Radiation and Free Electron Laser*. World Scientific, 2000.

[24] H. Wiedemann. *Synchrotron Radiation*. Springer-Verlag Berlin Hiedelberg, 2003.

[25] Elettra Sincrotrone Trieste. *FERMI official website*, 2014. https://www.elettra.trieste.it/it/lightsources/fermi/fermi-the-free-electron-laser-copy.html.

[26] André T.J.B. Eppink and David H. Parker. Velocity map imaging of ions and electrons using electrostatic lenses: Application in photoelectron and photofragment ion imaging of molecular oxygen. *Rev. Sci. Instruments*, 68:3477–3484, 1997.

[27] C. Bordas, F. Paulig, H. Helm and D.L. Huestis. Photoelectron imaging spectrometry: Principle and inversion method. *Review of Scientific Instruments*, 67(6):2257–2268, 1996.

[28] Scientific Instrument Services Inc. *SIMION software documentation*, 2014. simion.com.

[29] Michael Guilhaus. Special feature: Tutorial. principles and instrumentation in time-of-flight mass spectrometry. physical and instrumental concepts. *Journal of Mass Spectrometry*, 30(11):1519–1532, 1995.

[30] W.C.Wiley and I.H. McLaren. Time-of-flight mass spectrometer with improved resolution. *Rev. Sci. Instruments*, 26:1150, 1955.

[31] J.H.D Eland. *Photoelectron Spectroscopy: An Introduction to Ultraviolet Photoelectron Spectroscopy in the Gas Phase*. Butterworths, 1984.

[32] M. Di Fraia, M. Antonelli, A. Tallaire, J. Achard, S. Carrato, R.H. Menk, G. Cautero, D. Giuressi, W.H. Jark, F. D'Acapito, A. De Sio, E. Pace. X-ray beam position monitor based on a single crystal diamond performing bunch by bunch detection. *Journal of Physics: Conference Series*, 425:212001, 2013.

[33] M. Antonelli, M. Di Fraia, S. Carrato, G. Cautero, R.H. Menk, W.H. Jark, T. Ganbold, G. Biasiol, C. Callegari, M. Coreno, A. De Sio, E. Pace. Fast synchrotron and FEL beam monitors based on single-crystal diamond detectors and InGaAs/InAlAs quantum well devices. *Nuclear Instruments and Methods in Physics Research A*, 26:164–167, 2013.

[34] A. De Sio, M. Di Fraia, M. Antonelli, R.H. Menk, G. Cautero, S. Carrato, L. Tozzetti, J. Achard, A. Tallaire, R.S. Sussmann, E. Pace. X-ray micro beam analysis of the photoresponse of an enlarged CVD diamond single crystal. *Diamond and Related Materials*, 34:36 – 40, 2013.

[35] K. Prince, R. Blyth, R. Delaunay, M. Zitnik, J. Krempasky, J.S.J, R. Cammilloni, L. Avaldi, M. Coreno, G. Stefani, C. Furlani, M. de Simone, S. Stranges . The gas-phase photomemission beamline at Elettra. *Journal of Synchrotron Radiation*, 5(3):565–568, 1998.

[36] P. O'Keeffe, P. Bolognesi, M. Coreno, A. Moise, R. Richter, G. Cautero, R. Sergo, L. Stebel, L. Pravica, Y. Ovcharenko, L. Avaldi. A photoelectron velocity map imaging spectrometer for experiments combining synchrotron and laser radiation. *The Review of Scientific Instruments*, 82:033109, 2011.

[37] ADIXEN by Pfeiffer Vacuum. *Manual Adixen ATP 2300 M*, 2014. www.pfeiffer-vacuum.com/products/turbopumps/magnetically-levitated/atp-2300-m/onlinecatalog.action.

[38] Allectra GmbH. *Allectra website*, 2014. www.allectra.com.

[39] Frank Stienkemeier and Kevin K Lehmann. Spectroscopy and dynamics in helium nanodroplets. *Journal of Physics B: Atomic, Molecular and Optical Physics*, 39(8):R127, 2006.

[40] D. Buchta, S. R. Krishnan, N. B. Brauer, M. Drabbels, P. O'Keeffe, M. Devetta, M. Di Fraia, C. Callegari, R. Richter, M. Coreno, K. C. Prince, F. Stienkemeier, J. Ullrich, R. Moshammer, M. Mudrich. Extreme ultraviolet ionization of pure He nanodroplets: Mass-correlated photoelectron imaging, penning ionization, and electron energy-loss spectra. *The Journal of Chemical Physics*, 139(084301), 2013.

[41] D. Pentlehner, R. Riechers, B. Dick, A. Slenczka, U. Even, N. Lavie, R. Brown, K. Luria. Rapidly pulsed helium droplet source. *Review of Scientific Instruments*, 80(4), 2009.

[42] G. Cautero, R. Sergo, L. Stebel, P. Lacovig, P. Pittana, M. Predonzani, S. Carrato. A two-dimensional detector for pump-and-probe and time resolved experiments. *Nuclear Instruments and Methods in Physics Research Section A*, 595:447–459, 2008.

[43] Hamamatsu Photonics. *Hamamatsu Micro Channel Plates*, 2014. www.hamamatsu.com/eu/en/product/category/3100/3008/index.html.

[44] tectra GmbH Physikalische Instrumente. *tectra website*, 2011. www.tectra.de.

[45] D. Buchta, S. R. Krishnan, N. B. Brauer, M. Drabbels, P. O'Keeffe, M. Devetta, M. Di Fraia, C. Callegari, R. Richter, M. Coreno, K. C. Prince, F. Stienkemeier, R. Moshammer, M. Mudrich. Charge transfer and penning ionization of dopants in or on helium nanodroplets exposed to EUV radiation. *The Journal of Physical Chemistry A*, 117(21):4394–4403, 2013.

[46] EMCO High Voltage Corporation. *EMCO webpage*, 2014. www.emcohighvoltage.com.

[47] Elettra Sincrotrone Trieste S.C.p.A. *User guide advanced 4-channel time converter THR02-ST*, 2014. http://iloweb.elettra.eu/index.php?page=_layout_prodotto&id=222&lang=it.

[48] National Instruments. *LabVIEW System Design Software*, 2014. www.ni.com/labview/i/.

[49] V. Lyamayev,Y. Ovcharenko, R. Katzy, M. Devetta, L. Bruder,A. LaForge, M. Mudrich, U. Person, F. Stienkemeier, M. Krikunova,T. M´oller,P. Piseri, L. Avaldi,M. Coreno, P. O'Keeffe, P. Bolognesi, M. Alagia, A. Kivim´aki, M. Di Fraia,N.B. Brauer, M. Drabbels,T. Mazza, S. Stranges, P. Finetti, C. Grazioli, O. Plekan, R. Richter, K.C. Prince, C. Callegari. A modular end-station for atomic, molecular, and cluster science at the low density matter beamline of FERMI@Elettra. *Journal of Physics B: Atomic, Molecular and Optical Physics*, 46(16):164007, 2013.

[50] Elettra Sincrotrone Trieste. *PADReS website*, 2014. www.elettra.trieste.it/it/lightsources/fermi/padres/padres-home.html.

[51] Allaria E., Diviacco B., Callegari C., Finetti P., Mahieu B., Viefhaus J., Zangrando M., De Ninno G., Lambert G., Ferrari E., Buck J., Ilchen M., Vodungbo B., Mahne N., Svetina C., Spezzani C., Di Mitri S., Penco G., Trovó M., Fawley W.M., Rebernik P.R., Gauthier D., Grazioli C., Coreno M., Ressel B., Kivimäki A., Mazza T., Glaser L., Scholz F., Seltmann J., Gessler P., Grünert J., De Fanis A., Meyer M., Knie A., Moeller S.P., Raimondi L., Capotondi F., Pedersoli E., Plekan O., Danailov M.B., Demidovich A., Nikolov I., Abrami A., Gautier J., Lüning J., Zeitoun P., Giannessi L. Control of the polarization of a vacuum-ultraviolet, high-gain, free-electron laser. *Phys. Rev. X*, 4:041040, 2014.

[52] C. Svetina, C. Grazioli, M. Alagia, L. Avaldi, G. Cautero, M. de Simone, M. Devetta, M. Di Fraia, M. Drabbels, C. Fava, V. Feyer, P. Finetti, S. Gerusina, R. Katzy, A. Kivimaki, V. Lyamayev, N. Mahne, T. Mazza, A. Moises, T. Möller, P. O'Keeffe, Y. Ovcharenko, P. Piseri, O. Plekan, K.C. Prince, L. Raimondi, R. Sergo, F. Stienkemeier, S. Stranges, M. Zangrando, M. Coreno and C. Callegari. The Low Density Matter (LDM) beamline of FERMI. *Journal of Synchrotron Radiation*, Submitted.

[53] S. Mondal, R. Ma, K. Motomura, H. Fukuzawa, A. Yamada, K. Nagaya, S. Yase, Y. Mizoguchi, M. Yao, A. Rouzee, A. Hundertmark, M. J. J. Vrakking, P. Johnsson, M. Nagasono, K. Tono, T. Togashi, Y. Senba, H. Ohashi, M. Yabashi, T. Ishikawa, I. P. Sazhina, S. Fritzsche, N. M. Kabachnik, K. Ueda. Photoelectron angular distributions for the two-photon sequential double ionization of xenon by ultrashort extreme ultraviolet free electron laser pulses. *Journal of Physics B: Atomic, Molecular and Optical Physics*, 46(16):164022, 2013.

[54] Andor Technology Ltd (Andor). *Andor Neo Camera*, 2014. http://www.andor.com/scientific-cameras/neo-and-zyla-scmos-cameras/neo-55-scmos.

[55] Plone Foundation. *TANGO Controls Website*, 2014. www.tango-controls.org.

[56] Elettra Sincrotrone Trieste S.C.p.A. *AH501B Picoammeter*, 2014. http://iloweb.elettra.eu/index.php?page=_layout_prodotto&id=141&lang=it.

[57] P. O'Keeffe, E. Ripani, P. Bolognesi, M. Coreno, M. Devetta, C. Callegari, M. Di Fraia, K.C. Prince, R. Richter, M. Alagia, A. Kivimäki, L. Avaldi. The role of the partner atom and resonant excitation energy in interatomic coulombic decay in rare gas dimers. *The Journal of Physical Chemistry Letters*, 4(11):1797–1801, 2013.

[58] A. C. LaForge, M. Drabbels, N. B. Brauer, M. Coreno, M. Devetta, M. Di Fraia, P. Finetti, C. Grazioli, R. Katzy,V. Lyamayev, T. Mazza, M. Mudrich, P. O'Keeffe, Y. Ovcharenko, P. Piseri, O. Plekan, K. C. Prince, R. Richter, S. Stranges, C. Callegari, T. Möller, F. Stienkemeier. Collective autoionization in multiply-excited systems: A novel ionization process observed in helium nanodroplets. *Scientific Reports*, 4:3621, 2014.

[59] T. Mazza, M. Ilchen, A. J. Rafipoor, C. Callegari, P. Finetti, O. Plekan, K. C. Prince, R. Richter, M. B. Danailov, A. Demidovich, G. De Ninno, C. Grazioli, R. Ivanov, N. Mahne, L. Raimondi, C. Svetina, L. Avaldi, P. Bolognesi, M. Coreno, P. O'Keeffe, M. Di Fraia, M. Devetta, Y. Ovcharenko, T. Möller, V. Lyamayev, F. Stienkemeier, S. Düsterer, K. Ueda, J. T. Costello, A. K. Kazansky, N. M. Kabachnik, M. Meyer. Determining the polarization state of an extreme ultraviolet free-electron laser beam using atomic circular dichroism. *Nature Communications*, 5:3648, 2013.

[60] Y. Ovcharenko, V. Lyamayev, R. Katzy, M. Devetta, A. LaForge, P. O'Keeffe, O. Plekan, P. Finetti, M. Di Fraia, M. Mudrich, M. Krikunova, P. Piseri, M. Coreno, N.B. Brauer, T. Mazza, S. Stranges, C. Grazioli, R. Richter, K.C. Prince, M. Drabbels, C. Callegari, F. Stienkemeier, T. Möller . Novel collective autoionization process observed in electron spectra of He clusters. *Physical Review Letters*, 112:073401, Feb 2014.

[61] The National Institute of Standards and Technology (NIST). *NIST Atomic Weights and isotopic Composition*, 2014. http://www.nist.gov/pml/data/comp.cfm.

[62] G. Öhrwall, M. Tchaplyguine, M. Gisselbrecht, M. Lundwall, R. Feifel, T. Rander, J. Schulz, R.R.T. Marinho, A. Lindgren, S.L. Sorensen, S. Svensson, O. Björneholm. Observation of elastic scattering effects on photoelectron angular distributions in free Xe clusters. *Journal of Physics B: Atomic, Molecular and Optical Physics*, 36(19):3937, 2003.

[63] P. O'Keeffe, A. Ciavardini, E. Ripani, P. Bolognesi, M. Coreno, L. Avaldi, M. Devetta, M. Di Fraia, C. Callegari, K. C. Prince, R. Richter. Experimental investigation of the interatomic coulombic decay in NeAr dimers. *Physical Review A*, 90:042508, Oct 2014.

[64] Cederbaum L.S., Zobeley J., Tarantelli F. Giant intermolecular decay and fragmentation of clusters. *Phys. Rev. Lett.*, 79:4778–4781, Dec 1997.

[65] G. Margaritondo and P.R. Ribic. A simplified description of X-ray free-electron lasers. *Journal of Synchrotron Radiation*, 18((Pt-2)):101–108, 2011.

[66] J. U. Grabow, A. S. Pine, G. T. Fraser, F. J. Lovas, R. D. Suenram, T. Emilsson, E. Arunan, and H. S. Gutowsky. Rotational spectra and van der waals potentials of ne-ar. *The Journal of Chemical Physics*, 102(3), 1995.

[67] S. Scheit, V. Averbukh, H-D. Meyer, J. Zobeley, L.S. Cederbaum. Interatomic coulombic decay in a heteroatomic rare gas cluster. *The Journal of Chemical Physics*, 124(15), 2006.

[68] A. I. Kuleff, K. Gokhberg, S. Kopelke and L.S. Cederbaum. Ultrafast interatomic electronic decay in multiply excited clusters. *Physical Review Letters*, 105(4):043004, 2010.

[69] M. Yan, H. R. Sadeghpour and A. Dalgarno. Photoionization cross sections of He and H2. *The Astrophysical Journal*, 496(2):1044, 1998.

[70] Alfred Maquet and Richard Taïeb. Two-colour IR+XUV spectroscopies: the "soft-photon approximation". *Journal of Modern Optics*, 54(13-15):1847–1857, 2007.

[71] J.P. Connerade. *Higly Excited Atoms*. Cambridge University Press, 1998.

[72] T. Ditmire, T. Donnelly, A. M. Rubenchik, R. W. Falcone, and M. D. Perry. Interaction of intense laser pulses with atomic clusters. *Physical Review A*, 53:3379–3402, 1996.

[73] M.B. Danailov, F. Bencivenga, F. Capotondi, F. Casolari, P. Cinquegrana, A. Demidovich, E. Giangrisostomi, M.P. Kiskinova, G. Kurdi, M. Manfredda, C. Masciovecchio, R. Mincigrucci, I.P. Nikolov, E. Pedersoli, E. Principi and P. Sigalotti. Towards jitter-free pump-probe measurements at seeded free electron laser facilities. *Optical Express*, 22(11):12869–12879, 2014.

[74] A. Bouhal, R. Evans, G. Grillon, A. Mysyrowicz, P. Breger, P. Agostini, R. C. Constantinescu, H. G. Muller, and D. von der Linde. Cross-correlation measurement of femtosecond noncollinear high-order harmonics. *Journal of the Optical Society of America B*, 14(4):950 – 956, 1997.

[75] Wenbin Li, Xiaoying Ma, Xiaoyue Yang, and Zhanshan Wang. Simulation of cross-correlation method for temporal characterization of VUV free-electron-lasers. *Chinese Optics Letters*, 11(9):091403, 2013.

[76] Imagine Optic. *HASO Shack-Hartmann wavefront sensors*, 2014. www.imagine-optic.com.

[77] Behlke Power Electronics GmbH. *Behlke fast HV switches*, 2014. www.behlke.com.

[78] A. Galimberti, C.J. Bocchetta, C. Fava, A. Gambitta, G. Paolucci, R. Presacco, G. Paolicelli, G. Stefani. A new detector for photon beam position monitoring designed for synchrotron radiation beamlines. *Nuclear Instruments and Methods in Physics Research Section A: Accelerators, Spectrometers, Detectors and Associated Equipment*, 477(1-3):317 – 322, 2002.

[79] Menk R.H., Giuressi D., Arfelli F.,Rigon L. Hiresmon: A fast high resolution beam position monitor for medium hard and hard x-rays. *AIP Conference Proceedings*, 879(1):1109–1112, 2007.

[80] Elettra Sincrotrone Trieste. *X-ray Fluorescence Beamline website*, 2014. http://www.elettra.trieste.it/it/lightsources/elettra/elettra-beamlines/microfluorescence/x-ray-fluorescence.html.

[81] Elettra Sincrotrone Trieste. *Circular Polarization Beamline website*, 2014. http://www.elettra.trieste.it/it/lightsources/elettra/elettra-beamlines/cipo/cipo.html.

[82] M. Antonelli, R.H. Menk, G. Cautero, D. Giuressi,S. Lizzit, A. De Sio, E. Pace, M. Di Fraia. Diamond-based photon bpms for fast electron-beam diagnostics in synchrotron radiation sources. *Proceedings of IBIC2014, SLAC, USA*, TUPF13, 2014. In press.

[83] M. Antonelli, G. Cautero, I. Cudin, D. M. Eichert, D. Giuressi, W. H. Jark, E. Karantzoulis, S. Lizzit, R. H. Menk, A. De Sio, E. Pace, M. Di Fraia. Fast beam diagnostics for third-generation synchrotrons by means of novel diamond-based photon bpms. *Proceedings of IPAC2014, Dresden, Germany*, THPME128, 2014.

[84] Gustavo A. Garcia, Laurent Nahon, and Ivan Powis. Two-dimensional charged particle image inversion using a polar basis function expansion. *Review of Scientific Instruments*, 75(11):4989–4996, 2004.

[85] L. B. Madesn and P. Lambropoulos. Scaling of hydrogenic atoms and ions interacting with laser fields: Positronium in a laser field. *Physical Review A*, 59(6):4574–4579, 1999.

[86] L. A. A. Nikolopoulos and P. Lambropoulos. Helium double ionization signals under soft-x-ray coherent radiation. *Journal of Physics B: Atom. Mol. Opt. Phys.*, 39:883–893, 2006.

[87] Los Alamos National Laboratory. *LANL Atomic Physics Codes*, 2014. http://aphysics2.lanl.gov/cgi-bin/ION/runlanl08d.pl.

[88] Piraux B., Bauer J., Laulan S. and Bachau H. Probing electron-electron correlation with attosecond pulses. *The European Physical Journal D*, 26:7–13, 2003.